11-1-2010

# Effects of structured roughness on fluid flow at the microscale level

Rebecca Noelani Wagner

## Recommended Citation

Wagner, Rebecca Noelani, "Effects of structured roughness on fluid flow at the microscale level" (2010). Thesis. Rochester Institute of Technology. Accessed from

# Effects of Structured Roughness on Fluid Flow at the Microscale Level

by

Rebecca Noelani Wagner

*A Thesis Submitted in Partial Fulfillment of the Requirements for the degree of*
*Master of Science in Mechanical Engineering*

Approved by:

**Dr. Satish Kandlikar**
Department of Mechanical Engineering (Thesis Advisor)

**Dr. Steven Weinstein**
Department of Chemical and Biomedical Engineering (Committee Member)

**Dr. Kathleen Lamkin-Kennard**
Department of Mechanical Engineering (Committee Member)

**Dr. Alan Nye**
Department of Mechanical Engineering (Department Representative)

**Department of Mechanical Engineering**
**Rochester Institute of Technology**
**Rochester, NY 14623**
**November 2010**

# Permission for Thesis Reproduction

I, Rebecca Noelani Wagner, hereby grant permission to the Wallace Memorial Library of the Rochester Institute of Technology to reproduce my thesis entitled *Effects of Structured Roughness on Fluid Flow at the Microscale Level* in whole or in part. Any reproduction will not be for commercial use or profit.

| | |
|---|---|
| Rebecca Noelani Wagner | November 19, 2010 |

# Abstract

There are no theoretical differences between microscale and macroscale flows for incompressible liquids. Fluid flow and heat transfer characteristics in microchannels, however, are known to deviate from conventional macroscale theory in both the laminar and turbulent regimes. As the hydraulic diameter of a channel decreases, the effects of inherent surface roughness within the channel becomes more apparent, causing an increase in frictional losses and early transition to turbulence, as well as unpredictable heat transfer performance. Though many have experimentally, analytically, and numerically established that such deviations occur, the hypotheses attempting to characterize the deviations are sometimes contradictory and frequently employ correctional factors. Hence, no concise and conclusive explanation has been given.

Difficulties with existing knowledge hinge around defining surface roughness itself. Average roughness amplitude parameters are commonly in use, but do not provide sufficient representation of designed roughness structures. Two-dimensional grooves or ridges can yield the same amplitude values yet exhibit vastly different hydraulic and heat transfer performance.

This work aims to characterize structured surface roughness using existing parameters, and form a theoretical model to correlate surface descriptors to fluid performance in rectangular channels of varying aspect ratios and surface geometries. A theoretical model was developed to predict the effect of roughness pitch and height on pressure drop along the channel length, using friction factors for comparison with prior work. Validation of the proposed theory was carried out through experimentation with water flow in channels possessing designed transverse rib roughness. The end goal was to develop a clear understanding of the effect of two-dimensional structured roughness on frictional losses in fully-developed laminar flow, with the potential for extension to analysis of heat transfer and developing flow.

# Table of Contents

## List of Figures

## List of Tables

# Nomenclature

## Latin

| | |
|---|---|
| $A$ | Area, surface or cross-sectional, as noted in the text |
| $a$ | Rectangular channel height, or longer of the two dimensions |
| $b$ | Rectangular channel separation, or smaller channel dimension |
| $b_{eff}$ | Effective channel separation |
| $D$ | Pipe diameter |
| $D_h$ | Hydraulic diameter |
| $e$ | Roughness size, used in the Moody diagram [1] |
| $F_p$ | Average floor profile (alternatively named *FdRa*) |
| $f$ | Friction factor |
| $f(x)$ | Lower wall function |
| $g$ | Gravity |
| $g(x)$ | Upper wall function |
| $h$ | Roughness height, wall function method |
| $k$ | Roughness height, as defined by Von Mises [2] |
| $P$ | Pressure |
| $Q$ | Volumetric flow rate |
| $r$ | Pipe radius |
| $R_a$ | Average roughness |
| $R_c$ | Average height |
| $R_{\Delta q}$ | RMS tilt |
| $Re$ | Reynolds number |
| $R_{ku}$ | Kurtosis |
| $R_p$ | Maximum peak height |
| $R_q$ | Root-mean-square (RMS) roughness |
| $R_{sk}$ | Skew |
| $R_{SM}$ | Mean spacing of peaks |
| $R_v$ | Minimum valley height |
| $R_z$ | Maximum or ten-point-peak height |
| $u$ | $x$-component of velocity |
| $v$ | $y$-component of velocity |
| $w$ | $z$-component of velocity |

## Greek

| | |
|---|---|
| $\alpha$ | Channel aspect ratio; smaller dimension divided by larger |
| $\delta$ | boundary layer thickness |
| $\Delta_a$ | Mean slope of roughness profile |
| $\varepsilon_{Fp}$ | Roughness height parameter, for constricted flow model [3] |
| $\lambda$ | Roughness pitch |
| $\mu$ | Dynamic viscosity |
| $\rho$ | Density |

## Subscripts

| | |
|---|---|
| $cf$ | Constricted flow |

# 1 Introduction

The drive for understanding the fundamentals of microfluidics is not a new topic of discussion, as microchannels have been in use since the 1960’s. However, the recent increase in applications for microchannels has spurred the need for ongoing research.

Microchannel dimensions permit very high surface-area-to-volume ratios, greatly enhancing heat and mass transfer, as well as chemical reactivity. The enhanced heat transfer makes microchannel heat exchangers (MHE’s) ideal in electronics cooling applications. In particular, the small footprints of MHE’s make them ideal for cooling the densely packed processor and memory units in servers and super computers. Some companies are currently developing microchannel reactors, similar to MHE’s, in which reaction conditions can be precisely controlled for processes such as hydrogen production, conversion of natural gas into synthetic fuel, and the production of household chemicals. Most of these devices are composed of arrays of parallel channels, with critical dimensions, for microchannel reactors for example, ranging from 0.25 to 5 mm [4]. Bio-related applications for microchannels include drug delivery research and detection and separation of pathogens (viral, bacterial, and fungal) such as E. coli. Microchannel technology also allows for accurate simulation of chemical diffusion in the blood, brain tissue, lung tissue, etc. Overall advantages of using microchannels in industrial applications include increased product yields, improved energy efficiency, smaller device footprints, and reduced capital costs. Fundamental research on microscale transport processes is therefore required for further improvement and implementation of microchannel technology.

A major difficulty in microfluidic devices, and the primary topic of this work, is that of surface roughness. All surfaces possess natural or random roughness which results from manufacturing processes. Inside any channel one may expect to find the walls are neither smooth nor uniformly rough, but may have large burrs or gouges in various locations along the length of the channel. This random roughness is typically smaller than the boundary layer thickness in internal macroscale or large-scale flows. Therefore, it is assumed to have negligible influence in the laminar flow regime, although it may take effect in turbulent flow if its height is larger than the viscous boundary layer [5]. At the microscale level, where the channel walls are very closely spaced, the height of individual asperities may be on the order of the channel dimensions. High roughness can lead to greater frictional losses and earlier transition to turbulence.

Surface roughness is typically characterized by the use of average amplitude parameters. These conventional amplitude parameters are in common use because they are simple to calculate and provide a sufficient description of natural roughness in macroscale applications. In order to understand the effect of asperity height, slope, density, etc. of roughness on fluid flow, it is useful to consider structured roughness so as to both control and measure those aspects of surface geometry individually. The average amplitude parameters which are sufficient for uniform roughness are insufficient in representing structured or periodic roughness.

# 2 Related Work

## 2.1 Historical Perspective

Since Darcy identified the dependence of internal fluid flow on pipe diameter, inclination, and surface type in the 1800's [6], much effort has gone into experimental and theoretical assessments of the effects of roughness on internal flows. In the early 1900's, Von Mises highlighted the significance of relative roughness, which he defined as the ratio of roughness "size" to pipe radius, $k/r$ [2]. Hopf [7] and Fromm [8] later performed flow experiments on rectangular channels with various types of roughness. They classified surface types based on roughness aspect ratios and concluded that friction factor and Reynolds number are dependent on the surface type, differentiated by the roughness pitch-to-height ratio, $\lambda/h$, for repeating roughness structures. In an attempt to expand the understanding of flow in rough pipes at the time, Nikuradse performed exhaustive experiments assessing a complete range of Reynolds numbers for various $k/r$ values, while maintaining geometric similitude in pipe geometries, resulting in an enormous database for frictional flow in pipes [9]. In 1939, Colebrook developed the general (and well-known) formula for friction factor at high Reynolds numbers [10]. With Nikuradse's experimental results and Colebrook's turbulent flow formula, Moody [1] constructed a convenient means, in graphical form, for estimating friction factors based on relative roughness and Reynolds number, making the Darcy-Weisbach equation more readily applicable.

The Moody diagram allows for prediction of fluid behavior in macroscale pipes, and has been in use in both academic and industry settings for decades. The diagram is limited to relative roughness values of 5% and lower, or $e/D < 0.05$, however, and indicates that roughness of any size has no effect on friction factors in the laminar flow regime. This conclusion that roughness takes no effect in laminar flows is still pervasive today in that the flow in conventional-sized pipes and channels is typically turbulent, so the variance in the friction factors for laminar flows are of less practical importance. Interest in microscale phenomena has increased in the recent past due to its usefulness for passive enhancement of microfluidic devices. With the increase in the use of microscale geometries in various applications, and because flows in microscale pipes and ducts are often laminar, the study of laminar flow in roughened microchannels is of significant importance. Experiments performed since the 1980's indicate that as the pipe size decreases there is significant deviation from conventional theory in both laminar and turbulent regimes [11].

## 2.2 Channel Geometry

Early research on internal flows focused on circular ducts or conventional pipes, as was the case with the data used to generate the Moody diagram. For fully developed, laminar flow in circular ducts, the Darcy friction factor may be defined as $64/Re_D$, where $Re_D$ is the Reynolds number calculated using the pipe diameter as the characteristic length. This definition of laminar friction factor does not hold true for non-circular geometries, since the wall shear varies around the perimeter of the duct. In order to extend conventional correlations for non-circular geometries, the hydraulic diameter may be used in place of the characteristic length;

$$D_h = \frac{4A}{P}$$

where $A$ is the cross-sectional area and $P$ is the wetted perimeter, or the length of the wall in contact with the fluid flowing through the cross-section. For a rectangular cross-section in which one side is significantly smaller than the other, $D_h$ limits to twice the smaller dimension. This concept of hydraulic diameter is used simply to extend existing empirical correlations for pipe flow to non-circular geometries, and to represent the characteristic length scale in fluid mechanics.

Throughout the 1970's, Shah worked to analyze the variation of fully developed, laminar flow friction factors in smooth ducts of various cross sectional geometries using a least-squares-matching technique [12, 13]. His work resulted in a compilation of analytical solutions for flow friction based on data from over 300 sources for 25 duct geometries. These solutions are still used for comparison to this day, and are likewise used for smooth channel comparison in this work.

In more recent literature, researchers have reported that friction factors in non-circular geometries begin to differ from Shah's findings as the channel size decreases to the microscale level. In gas flows, the discrepancy may be attributed to slip flow at the boundaries, but this does not explain the difference for incompressible flows. Prior works on liquid flow in microchannels have reported significant increases [14-17] or decreases [18, 19] in friction factors from conventional laminar theory, while others reported negligible deviations [20-24]. In addition to these, other authors have reported increases in friction factors for some geometries or aspect ratios, but decreases for others [25, 26]. Many of these authors highlighted the role of wall roughness in their observed deviations.

While a wide variety of channel shapes and sizes have been investigated in literature, the classification of channel size (i.e. microscale, miniscale, etc.) is still not definitive. In many cases, the term microchannel may be applied to channels having a hydraulic diameter greater than 1 mm. The classification scheme recommended by Kandlikar and Grande [27] indicates delineations based on molecular mean free path considerations for single phase gas flow, and surface tension effects in two phase flow. Their conclusion result in the following classifications:

| | |
|---|---|
| Conventional channels: | $D_h > 3$ mm |
| Minichannels: | $200\ \mu m < D_h \leq 3$ mm |
| Microchannels: | $10\ \mu m < D_h \leq 200\ \mu m$ |

An earlier classification scheme was defined arbitrarily for size-range classification in industry by Mehendale *et al*. [28] as follows:

| | |
|---|---|
| Conventional channels: | $D_h > 6$ mm |
| Compact Passages: | $1\ mm < D_h \leq 6$ mm |
| Mesochannels: | $100\ \mu m < D_h \leq 1$ mm |
| Microchannels: | $1\ \mu m < D_h \leq 100\ \mu m$ |

Scale may indicate both the channel size and roughness size. Through the use of either of these schemes, it is revealed that the majority of conventional microfluidic devices are in actuality comprised of minichannels. Size classification becomes more complicated with channels of non-circular cross-sections, as channel shape and aspect ratio are known to have significant effects on flow behavior in channels of all sizes [12, 13]. It is recommended by Kandlikar *et al*. [11] that the minimum dimension of any given channel be used in place of the hydraulic diameter. That is, for rectangular channels the shorter side of the rectangle will replace the hydraulic diameter in calculations and table look-ups. Bahrami *et al.* [29] recommend using the square root of a channel's cross-sectional area as the characteristic length, as they claim it is superior to the hydraulic diameter.

Although the effects of channel geometry on internal fluid flow have been studied extensively in literature, the channel size effects are still not definitive. It is generally agreed upon, however, that surface roughness must be understood in small-scale flows. The majority of pre-1990's literature is concerned with the general aspects of flows over rough walls, while more recent research has emphasized the differences between various types of roughness. These types are separated here into two categories; uniform and structured roughness.

## 2.3 Uniform Roughness

The surface roughness used in many experiments can be classified as uniform or Gaussian roughness. That is, the amplitude density distribution for the data obtained from a profilometer, microscope, or other metrology device is a normal or Gaussian distribution. When glass is etched or metals are abraded, the outcome is frequently Gaussian. The roughness that results naturally from various machining and manufacture techniques is random, but frequently Gaussian. The difference is that random roughness is not controlled or deliberate, whereas etching or polishing is done in order to obtain a desired surface finish. A skewed distribution is indicative of prominent peaks or valleys across a surface, but in general the same geometry would be found uniformly across an etched or grit blasted surface.

The Moody diagram is based heavily on experimental data for uniformly rough surfaces. Nikuradse, for example, sifted and re-sifted sand so that the grain diameters were approximately the same, then used a lacquer to adhere the sand to the inner surfaces of pipes [9]. Since then, authors have attempted to equate surface roughness to an equivalent sand grain roughness. Such an approach to roughness characterization is questionable as the method of gluing sand to a surface may not result in roughness that is the same size as the sand grains, nor could repeating Nikuradse’s method result in the same density or distribution of grains on the surface. Any slight difference in coating or drying the sand could result in different flow resistance. While the size of uniform roughness may be controlled in this technique, the distribution is entirely uniform across the surface and is difficult to characterize by anything other than amplitude parameters, hence the desire to use an equivalent sand grain roughness for comparison.

Existing roughness parameters primarily serve to describe natural or uniform roughness by the average or extreme height. Standard amplitude parameters include the average roughness, $R_a$, which is the arithmetic mean of surface height values, and the root-mean-square (RMS) roughness, $R_q$, which is the standard deviation of the height distribution. Line measurements are represented by $R$, whereas surface measurements are represented by $S$. Most amplitude parameters use the average roughness as a reference line. Extreme height parameters, for example, represent the highest peaks or deepest gouges in a surface relative to the mean line. In Nikuradse’s experiments, the use of the sand grain diameter for the roughness value is comparable to using an extreme amplitude parameter to represent the surface in that the sand particles would not actually project into the boundary layer to their full diameter due to the laquer coating. Amplitude parameters are useful for surface specification and control in design and manufacturing, but cannot effectively predict hydraulic performance.

Alternative roughness parameters may contribute to the prediction of hydraulic performance, but are not in common use for fluid flow applications. The skew of a surface, $R_{sk}$, represents the symmetry of that profile about its meanline, indicating whether it possesses many sharp peaks (positive skewness), sharp valleys (negative skewness), or is a Gaussian distribution ($R_{sk} = 0$). Kurtosis, $R_{ku}$, represents the peakedness of a surface, qualifying the flatness of the amplitude density distribution. A leptokurtic surface ($R_{ku} > 3$) possesses frequent extreme peaks and valleys, as opposed to a platykurtic surface which exhibits infrequent or small deviations. There are also parameters for counting the number of times a profile crosses a threshold, and for evaluating the density or slopes of peaks. These and many other spatial or functional parameters have potential for use in predicting surface effects on fluid flows.

Menezes *et al.* [30] roughened steel surfaces with wet and dry emery paper in various patterns in order to correlate twenty five existing roughness parameters, including skew and kurtosis, with the coefficient of friction for each surface under lubricated conditions. He found that the performance of each plate was independent of the average roughness $R_a$, but correlated well with the mean slope of the profile $\Delta_a$ for every surface. This parameter is the arithmetic mean of the slopes between every pair of successive points of a roughness profile, giving an indication of the shape of the profile. Although it compared well in the reported experiments, it does not completely describe a surface and may need to be combined with an amplitude or hybrid parameter. No conclusion was made for the skew or kurtosis parameters, though it was implied that these were unable to be correlated with the frictional coefficient.

In 2005, Kandlikar *et al*. [3] proposed the use of a constricted parameter for use in estimating pressure drop in roughened microchannels. The parameter $\varepsilon_{Fp}$ is a function of the average roughness and two other amplitude parameters, and serves to account more accurately for the extent to which roughness elements project into the boundary layer. This constricted flow approach led to a modified Moody diagram which covers higher relative roughness values and smaller hydraulic diameters. This approach is valid provided that the roughness elements are closely spaced. There is still a need, however, for further understanding the effect of roughness geometry on internal flows.

## 2.4 Structured Roughness

Structured or artificial roughness was studied at least as far back as the 1920’s with Hopf and Fromm’s saw-tooth style two-dimensional roughness [7, 8], followed by Schlichting’s three-dimensional arrays of spheres, cones, and angled roughness [31]. Structured roughness is obtained by adding or removing material from a surface in a deliberate and precise way such that a two- or three-dimensional pattern arises. Though the focus for these authors was on turbulent flow, they were some of the pioneers in artificial roughness studies.

As there is no “universal” parameter for structured roughness, many researchers have resorted to using roughness height values and relative roughness in order to assess and compare the effects of different roughness geometries on fluid flow, even in recent literature. Schlichting, who used an equivalent sand grain roughness in his study, also attempted to correlate the flow resistance with roughness density, quantified by the projected roughness area normal to flow divided by the total plate area. In 1952, Sams [32] experimented with structured roughness in laminar and turbulent flow by threading and cross-threading macroscale pipes ($D \approx 12.7$ mm). He concluded that the conventional “relative roughness” concept is not sufficiently representative of the effects of structured roughness, specifically his square thread type roughness, on hydraulic performance. Though the author went to great lengths to correlate friction factors with the square roughness height, width, and spacing, the final outcomes were a series of empirical formulations.

Numerical simulations have been employed for assessing structured roughness effects in microchannel flow by a number of researchers, either through the use of commercial CFD software or by programming finite difference methods manually in languages such as FORTRAN or computing environments like MATLAB, etc. Rawool *et al*. [33] simulated laminar air flow in microchannels possessing two-dimensional transverse rib roughness, and systematically varied the roughness cross-section from triangular to trapezoidal to rectangular, as well as varying the height and pitch, or peak-to-peak distance. The authors found that the roughness pitch plays a definite role in fluid flow, in that the friction factor increases as roughness elements are brought closer together, i.e. higher friction factors for smaller pitch values. This was in addition to the roughness height effect already seen in previous literature; friction factor increases as roughness height increases. Friction factors were also found to be greater for triangular and rectangular geometries, and lower for trapezoidal roughness. These results are in agreement with the numerical simulations of Wang *et al.* [34] and Sun and Faghri [35], enforcing the idea that the roughness geometry should be taken into consideration.

Transition to turbulence is frequently correlated to the ratio of roughness height to boundary layer thickness $k/\delta$, which highlights the importance of the interaction of roughness elements with the boundary layer. In a review on turbulent flows over transverse rib type roughness, Jiménez [36] described two types of roughness; *d*-type and *k*-type, and a transitional roughness that occurs between these two types. They *d*-type roughness was described as ribs closely spaced such that they can sustain stable vortices (recirculation downstream of the roughness elements) that serve to isolate the bulk flow from the roughness. The *k*-type roughness is sparser such that the flow separates at the top of the roughness element and reattaches downstream, before reaching the next roughness element. The vortices interact with the bulk flow for this sparse roughness, causing increased friction factors and early transition to turbulence. Coleman *et al*. [37] experimentally and numerically assessed the effect of transverse rib roughness pitch-to-height ratios, $\lambda/h$, on turbulent flow and identified "transitional" roughness, at $\lambda/h \approx 8$, as having the most predominant effect on fluid flow. The authors reported that values of $\lambda/h < 5$ indicate closely spaced ribs, *d*-type roughness, or skimming flow, while $\lambda/h > 5$ indicate isolated roughness elements, *k*-type roughness, or interactive flow. In the extremes where $\lambda/h$ is significantly greater or less than 5, the roughness effect is expected to diminish. Although these publications discussing roughness ratios focus on turbulent flows, the concept may still hold true for microscale laminar flows.

## 2.5 Roughness Models

As stated previously, there are no theoretical differences between microscale and macroscale flows for incompressible liquids. Some authors, however, have made modifications to conventional theory in order to account for microscale roughness effects. In this section, a few of those models for flow in rough microchannels are reviewed. These models were either developed for or have been applied to steady, laminar, fully-developed liquid flows in microchannels possessing uniform or structured roughness.

Mala and Li [38] proposed the roughness-viscosity model (RVM), in which the surface roughness increases the fluid viscosity near the wall, accounting for the increase in friction factor in laminar flow. The authors define roughness-viscosity as a function of distance from the wall, such that the roughness-viscosity is zero at the center of the channel and a positive, non-zero, finite value at the wall. The concept is that the surface roughness increases momentum transfer in the boundary layer near the wall. But this model includes a coefficient that must be determined experimentally.

Sabry [39] took a unique approach that is reminiscent of the Cassie-Baxter model for surface wetting; the liquid does not fully contact the rough walls, and gases are trapped between some roughness elements. Conceptually, in this model, when flow separation occurs over roughness elements, the flow will become separated from the wall by a thin film of gas. The author initially assumed a “blanket” of gas of a specified thickness completely separates the bulk liquid from the rough wall. Since, in actuality, a gas blanket could not completely separate the liquid from the solid, a shielding coefficient was introduced into the model. This correction factor would range from 0 for no entrained gas to 1 for total separation of liquid from solid. Though the concept may be of interest in heat transfer applications, as a vapor blanket would be likely to occur and would insulate the flow, this model does not address the variation in friction factor with roughness height, as has been observed in previous literature.

Koo and Kleinstreuer [40], and Kleinstreuer and Koo [41], proposed a porous medium layer (PML) model in which uniform or random surface roughness is represented by a porous region or layer on the walls of a channel. The surface roughness (or PML) can increase or decrease the friction factor, depending on the PML permeability. The authors found good agreement with previous data. However, the model requires a number of unique and obscure parameters, such as porosity, permeability, and resistance speed factor, resistance speed power, and resistance constant. Constraints for the resistance variables were stated, but their exact definitions were not clear.

Expanding on the PML model, Gamrat et al [42, 43] developed a roughness layer model (RLM) in which they employed a discrete element approach to represent roughness at the wall. The authors used two effective roughness height parameters that are dependent on two dimensionless parameters; porosity of the “rough layer” and roughness height normalized by roughness spacing. The authors reported good agreement with experimental data for both uniform and structured roughness. But, the model is semi-empirical, as a drag coefficient must be obtained experimentally.

## 2.6 Objectives

Definite departure from conventional laminar theory has been identified in numerous experiment-based publications. Vast portions of the experimental works have resulted in empirical relations, scaling factors, etc., and these correlations are not universally applicable across the full range of small-scale channels, roughness types, and fluids. Similarly, recent theoretical and numerical works result in scaling models or require correction factors. Although it is intuitive that flow over a rough surface will experience greater drag than a smooth surface, it is still unclear when, where, and how a rough surface will begin to affect the bulk flow.

The study described herein deals with laminar water flow in rectangular channels of small aspect ratios, primarily in what may be considered the minichannel range, but touches on the microscale regime. Structured roughness is evaluated for its controllability of pitch and height. This work is an extension of a series of experiments performed by Brackbill [44] with saw-tooth roughness in rectangular microchannels. Standard amplitude parameters were evaluated as well as spatial and functional parameters in order to determine a combination of parameters relevant to structured roughness surface description. The relative roughness, $\varepsilon_{Fp}/D_h$, and the ratio of roughness height to channel separation, $h/b$, were also assessed for comparison with prior works. It is shown here that flow between rough walls can be modeled without the detailed computation of the flow around the roughness elements themselves.

# 3 Theoretical Model

Two-dimensional structured roughness was studied for its controllability of height, pitch, and slope of periodic peaks. A theoretical flow model that incorporates descriptive roughness parameters was developed, with focus on fully developed laminar flow.

## 3.1 Fundamental Equations and Computational Domain

The Navier-Stokes (N-S) equations for an incompressible Newtonian fluid form the foundation for the theoretical treatment of the microscale problem presented here. The result of the analysis provides pressure as a function of velocity, fluid properties, and channel and roughness geometry. In addition, the continuity equation was used to complete the relationship between volumetric flow rate and pressure terms. The internal two-dimensional flow was assumed to be steady and fully developed, so that inlet and outlet effects may be neglected. For further simplification, fluid properties were assumed to be constant.

Channel orientation and geometry are displayed in Figure 1 below. Fluid flow is in the positive *x*-direction, transverse rib roughness is in the *x*-*y* plane, and gravity acts in the negative *y*-direction. The channel separation *b* is significantly less than the channel length *L*, and the channel aspect ratio is small, such that the flow is comparable to flow between infinite parallel plates.

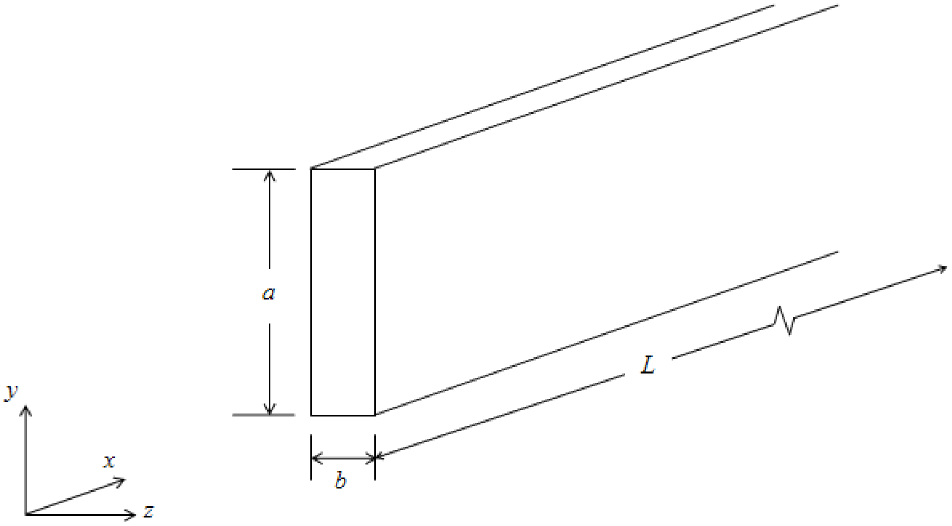

**Figure 1. Channel Geometry and Axis Orientation**

The computational domain is the region between the rough walls, in the *x*-*z* plane. The boundaries for the flow is the transverse rib roughness, represented by the functions *f*(*x*) and *g*(*x*) for the lower and upper walls, respectively, as seen in Figure 2. This periodic roughness is described by its pitch $\lambda$ and height *h*. Channel separation *b* is the difference between wall functions *f*(*x*) and *g*(*x*). The treatment of the separation *b* is discussed in the Surface Roughness and Channel Separation section. The limits of integration in the *x*-direction are from 0 to *L*.

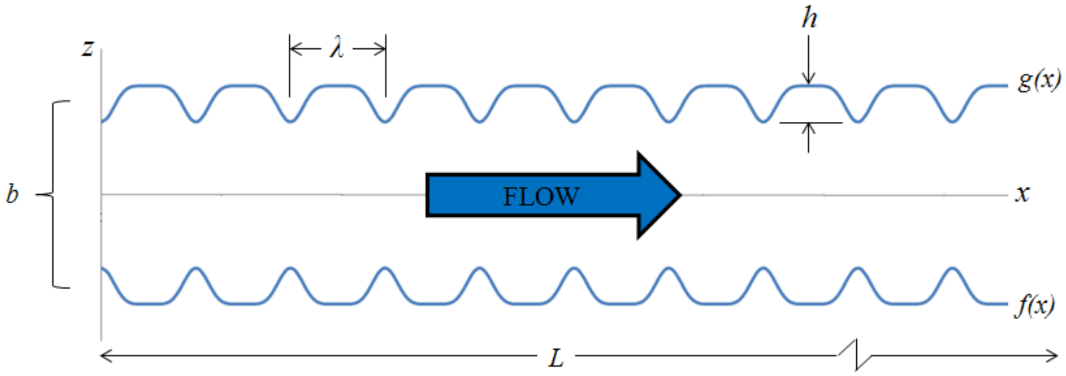

**Figure 2. Computational Domain**

## 3.2 Assumptions and System of Equations

This is a two-dimensional analysis, for which the velocity vector is $\vec{u} = u\hat{i} + w\hat{k}$. Flow is assumed to be steady, meaning any time derivatives are zero, resulting in a parabolic flow profile, which is validated in this section. The fluid is an incompressible liquid, for which the density and viscosity are constant. Gravity acts in the *y*-direction only, perpendicular to the computational domain shown in Figure 2 above. Inlet and outlet effects are neglected. The no-slip boundary condition is applied, i.e. velocity at the walls, where $z = f(x)$ and $z = g(x)$, is zero. In addition, it is assumed that the pressure at the inlet and outlet, or $P_0$ and $P_L$, respectively, are known.

The momentum equation, Newton's second law of motion, balances the acceleration of a fluid element and the forces imposed on it by neighboring elements. The continuity equation expresses conservation of mass for a constant density fluid. These comprise the system of equations used for the current analysis:

$$Continuity: \quad \frac{\partial u}{\partial x} + \frac{\partial w}{\partial z} = 0$$

$$N-S \begin{cases} x-component: & -\frac{\partial P}{\partial x} + \mu\left(\frac{\partial^2 u}{\partial x^2} + \frac{\partial^2 u}{\partial z^2}\right) = \rho\left(u\frac{\partial u}{\partial x} + w\frac{\partial u}{\partial z}\right) \\ y-component: & \rho g - \frac{\partial P}{\partial y} = 0 \\ z-component: & -\frac{\partial P}{\partial z} + \mu\left(\frac{\partial^2 w}{\partial x^2} + \frac{\partial^2 w}{\partial z^2}\right) = \rho\left(u\frac{\partial w}{\partial x} + w\frac{\partial w}{\partial z}\right) \end{cases}$$

### 3.2.1 Lubrication Approximation

To solve the full N-S equations requires the use of computational fluid dynamics. In this analysis, the lubrication approximation was applied for simplification by assuming that the slope of the trajectory of fluid elements is small. That is, velocity *w* in the *z*-direction is significantly less than velocity *u* in the *x*-direction. Figure 3 provides a visual representation of this assumption.

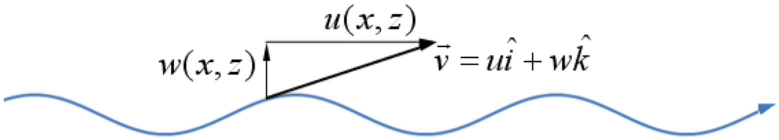

**Figure 3. Trajectory of a Fluid Particle and its Velocity Components**

Also referred to as the small slope approximation, it may be interpreted as; the slope of the boundaries is small at every point, such that $\frac{\partial f(x)}{\partial x} << 1$ and $\frac{\partial g(x)}{\partial x} << 1$. This approximation is often applied to flow fields in which the fluid is forced to move between two closely spaced surfaces, as with flow between infinite parallel plates or in a slot [45], where *b*/*L* << 1.

### 3.2.2 Simplified System of Equations

Application of the lubrication approximation makes no change to the continuity equation, but reduces the conservation of momentum equations thus:

$$N-S \quad \begin{cases} x-component: & \dfrac{\partial P}{\partial x} = \mu \dfrac{\partial^2 u}{\partial z^2} \\ y-component: & \dfrac{\partial P}{\partial y} = \rho g \\ z-component: & \dfrac{\partial P}{\partial z} = 0 \end{cases}$$

In the *x*-direction, all that remains is the viscous effects. Gravity only takes effect in the *y*-direction and may be used to assess variation of velocity in the *y*-direction. All inertial terms drop out due to the lubrication approximation. The lack of inertia implies very low Reynolds numbers (Stoke's flow) or flow in a slot of low relative roughness (small slope).

Integrating the *x*- and *y*-components of the simplified N-S equations and applying the no-slip boundary conditions yields the following:

$$P = \rho g y + p(x) \tag{1}$$

$$u = \frac{1}{2\mu}\frac{\partial P}{\partial x}\big(z - g(x)\big)\big(z - f(x)\big) \tag{2}$$

Equation 1 allows for an understanding of the effect of gravity on flow. It may be used to evaluate changes in the flow field in the *y*-direction. Equation 2 represents the bulk flow velocity profile in the absence of inertia. In laminar flow, if the channel separation *b* is significantly less than the length *L*, then the flow is approximately parabolic, as is this bulk profile. In an extended analysis, in section 3.5, this velocity profile serves as a trial function in an augmented lubrication approximation in which the inertial terms in the *x*-component are not discounted.

Integration of the continuity equation across the channel separation brings about a volumetric flow rate per unit depth relation. Applying Leibniz Rule, and utilizing equation 2 as an initial approximation for the velocity profile results in the following pressure–flow relation:

$$-\frac{1}{12\mu}\frac{\partial P}{\partial x}\big(g(x) - f(x)\big)^3 = \frac{Q}{a} \tag{3}$$

Rearranging for the differential pressure term as a function of flow:

$$\frac{\partial P}{\partial x} = -12\mu \frac{Q}{a} \frac{1}{\left(g(x) - f(x)\right)^3} \tag{4}$$

Integrating this differential equation along a specified length results in an equation for pressure-drop as a function of flow rate, viscosity, and the boundaries or wall function equations:

$$P_L - P_0 = -12\mu \frac{Q}{a} \int_0^L \frac{1}{\left(g(x) - f(x)\right)^3} \partial x \tag{5}$$

From here, equations for *g*(*x*) and *f*(*x*) are used to evaluate the integral and thereby predict the pressure drop along the length of rough channel. These two equations are the wall functions that represent structured two-dimensional roughness, and so this approach is referred to as the wall function method.

## 3.3 Wall Function Method

Pressure drop along a length of rectangular channel may now be predicted, provided that the channel and roughness geometries, fluid properties, and flow rate are known. Because the intention of this study was to investigate the effects of structured roughness on laminar fluid flow, it was necessary to utilize these wall functions *f*(*x*) and *g*(*x*) in such a way that the height and pitch of evenly spaced peaks may be systematically varied.

### 3.3.1 Structured Roughness

The form of the roughness chosen for this study was obtained through curve-fitting of existing two-dimensionally rough surfaces, possessing “saw-tooth” style roughness. These surfaces and the curve-fitting exercise are discussed further in Section 4.1, Saw-tooth Roughness. The equation format for the periodic roughness is:

$$f(x) = h\cos^p\left(\frac{\pi}{\lambda}x\right) - \frac{b}{2} \tag{6}$$

where $h$ is the height of roughness elements, $\lambda$ is the pitch or peak-to-peak spacing, $p$ is the power on the cosine which controls the slope of the peaks, and $b$ is the root channel separation, measured valley-to-valley. The opposing wall $g(x)$ is the negative of equation 6 (refer to Figure 2). Thus, the difference between these two functions results in the root channel separation minus a power sinusoid that is a function of $x$.

$$g(x) - f(x) = b - 2h\cos^{p}\left(\frac{\pi}{\lambda}x\right) \tag{7}$$

This form of two-dimensional roughness is convenient in that it allows for control of all parameters of interest, such that any one variable may be manipulated while keeping the remaining geometries constant. To evaluate the effect of alignment of roughness peaks on fluid flow, a phase shift variable may be added into the cosine function of one of the walls.

Implementing this style of roughness is not trivial for the theoretical model at hand. The integral in equation 5 is difficult to solve exactly, and requires the use of averaging techniques when boundaries of the form of equation 6 are used for the wall function input. Therefore, the Gaussian quadrature rule was used to approximate the integral. Code was written in MATLAB in order to expedite the analysis of an extensive combination of surface profiles, channel geometries, and flow rates. A sample of this code can be found in Appendix A.

### 3.4 Constricted Flow Method

In prior works by Brackbill [44] and Brackbill and Kandlikar [45, 46] an effective channel separation was used for evaluation of flow behavior. To achieve this, the integral portion of equation 5 was simplified by taking $f(x)$ and $g(x)$ to be constant values, i.e. the channel walls are essentially hydraulically smooth, thus:

$$\int_0^L \frac{1}{\left(g(x) - f(x)\right)^3}\partial x = \frac{L}{b_{eff}^3} \tag{8}$$

The effective separation, $b_{eff}$, is then defined as:

$$b_{eff} = g(x) - f(x) \tag{9}$$

Equation 5 becomes:

$$P_L - P_0 = -12\mu \frac{Q}{a} \frac{L}{b_{eff}^3} \tag{10}$$

This formulation has been found to be valid for macroscale channels, or channels possessing low relative roughness. For microscale flows, however, surface roughness must be accounted for. Average amplitude parameters currently in use have been shown to be ineffective by Perry *et al.* [48], therefore the channel separation must be given careful consideration.

### 3.4.1 Surface Roughness and Channel Separation

Amplitude parameters such as the average roughness, $R_a$, and root-mean-square roughness, $R_q$, are typically used to describe surfaces of random or uniform roughness, like the sand grain roughness used by Nikuradse. Simple average parameters and the concept of "relative roughness," however, are insufficient for structured two-dimensional roughness [32].

A sample of structured roughness, machined via ball end mill on CNC, and its associated $R_a$ and $R_q$ values are shown in Figure 4. This shows how utilizing these parameters would fail to account for the significant peaks in the profile, which may project into the boundary layer.

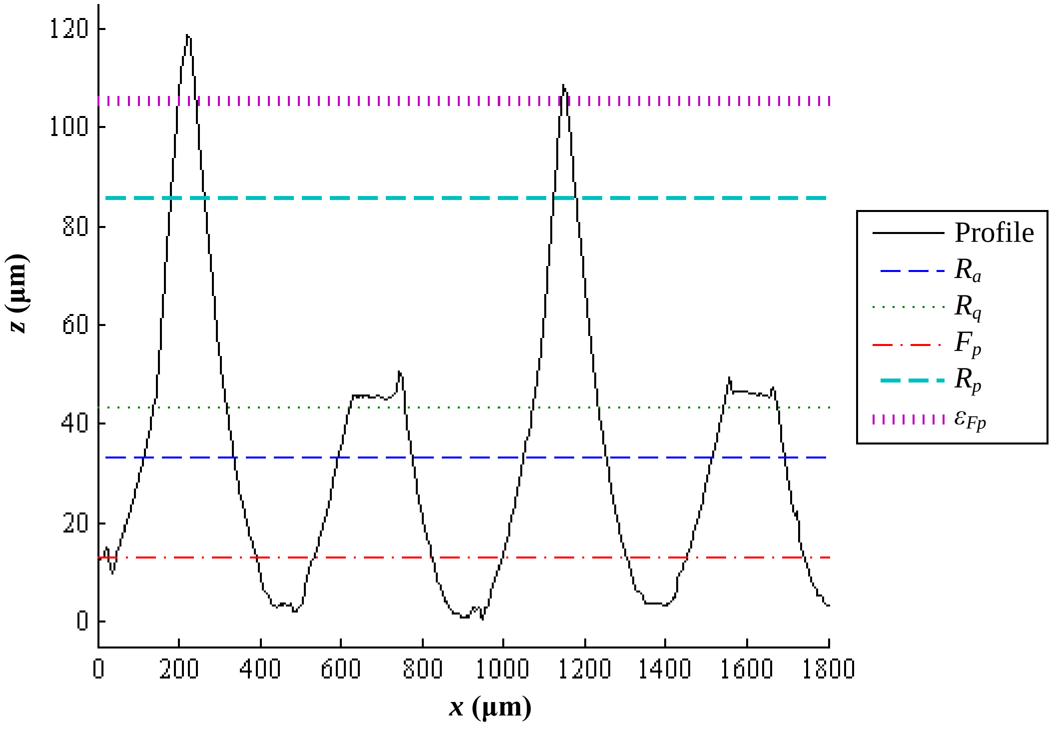

**Figure 4. Profilometer Data for 815 µm Pitch Saw-tooth Roughness Profile with Amplitude Parameters and Constricted Parameter, $\varepsilon_{Fp}$**

Kandlikar *et al*. [3] set forth a method for assessing a surface of significant random roughness or structured roughness. This new roughness factor, referred to as the constricted flow parameter, is a function of the average parameters typically obtained through surface analysis:

$$\begin{aligned} \varepsilon_{Fp} &= R_p + F_p \\ &= \left(\mathrm{Max} - R_a\right) + F_p \end{aligned} \tag{11}$$

where Max is the single highest point obtained from one evaluation length of any given profile. The floor profile, $F_p$, also called *FdRa*, is defined as the average of all points below the mean line, $R_a$, which is simply the arithmetic mean of the height of all points along a profile. These additional values for the 815 μm surface are also shown in Figure 4.

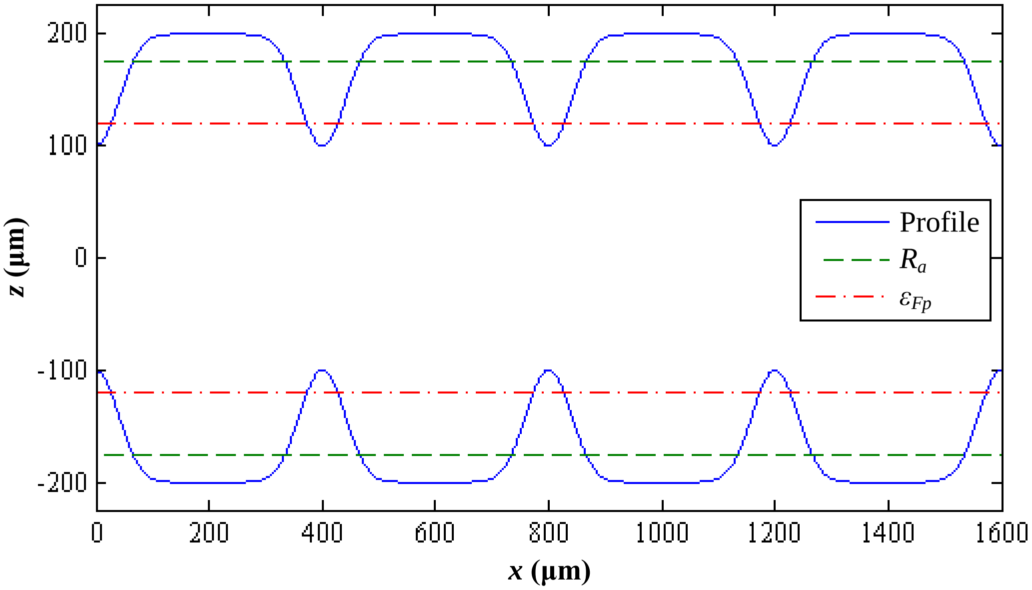

**Figure 5. Representative Channel and Roughness Geometry; $h$ = 100 μm, $\lambda$ = 400 μm, $b$ = 400 μm**

The constricted parameter was used to develop a constricted channel separation $b_{cf}$ for use in place of $b_{eff}$ in equation 10. This constricted separation is calculated as:

$$b_{cf} = b - 2\varepsilon_{Fp} \tag{12}$$

where $b$ is the root separation between two rough walls, measured between the floor profiles ($F_p$) of opposing surfaces. By this definition, any amplitude parameter could be used to “constrict” the channel separation. Figure 5 shows a sample cross-section of a channel possessing the ideal sinusoidal structured roughness discussed previously, with its constricted separation and average roughness separation. In this figure, it can be seen that using the average roughness to define the channel separation does not entirely account for the peaks.

In previous studies [45, 46], the constricted parameter was successfully used to fit experimental data to conventional laminar theory by using the constricted separation $b_{cf}$ in place of $b_{eff}$, in equation 10. This constricted flow method is effective in accounting for natural or random roughness, as well as some forms of structured roughness. It is not a strong function of roughness pitch, however, which is an aspect of structured roughness that is known to have a significant effect on fluid flow. Nor does the constricted parameter account for shape or alignment of roughness peaks. Therefore, to improve the understanding of the effects of structured two-dimensional roughness, it becomes necessary to consider all aspects of roughness geometry by representing the wall roughness as an exact function of $x$.

## 3.5 Further Theoretical Analysis

For relatively high Reynolds numbers, flow can be divided into a bulk region of inviscid flow unaffected by viscosity, and a region close to the wall where viscosity is significant (the boundary layer). The inertial term in the $x$-component of the N-S equation may be non-negligible. This further analysis allows us to understand the impact of the lubrication approximation itself without the added complication of unknown velocity profile assumptions. Also, it allows for examination of the velocity profile from the boundary layer solution and the behavior of the inertial term as the velocity increases and hydraulic diameter decreases.

An augmented velocity profile is required for this analysis. Incorporating the differential pressure function from the prior analysis (equation 4) into the initial velocity profile approximation (equation 2) yields:

$$u = \frac{6Q}{a\left(g(x) - f(x)\right)^3}\left(z - g(x)\right)\left(z - f(x)\right) \tag{13}$$

In this equation, velocity is strictly a function of flow rate and wall geometry, and varies with $x$ and $z$. The profile is parabolic and the equation satisfies the boundary conditions and continuity equation.

Using an augmented lubrication approximation in which the inertial term is not neglected, the *x*-component of N-S equation is:

$$-\frac{\partial P}{\partial x}+\mu\frac{\partial^2 u}{\partial z^2}=\rho\left(u\frac{\partial u}{\partial x}+w\frac{\partial u}{\partial z}\right) \tag{14}$$

Through the use of u-substitution and Leibniz Rule, this differential equation simplifies to:

$$-\frac{\partial P}{\partial x}\left(g(x)-f(x)\right)+\mu\left.\frac{\partial u}{\partial z}\right|_{f(x)}^{g(x)}=\rho\frac{\partial}{\partial x}\int_{f(x)}^{g(x)}u^2\partial z \tag{15}$$

If the velocity profile is known, this equation may be solved for a pressure–flow relation that includes the inertial term. Therefore, we use the velocity profile developed previously (equation 13) as a trial function, yielding the following pressure-drop equation:

$$P_L-P_0=-\frac{12\mu Q}{a}\int_0^L\frac{1}{\left(g(x)-f(x)\right)^3}\partial x+\frac{6\rho Q^2}{5a^2}\int_0^L\left(\frac{\frac{\partial g(x)}{\partial x}-\frac{\partial f(x)}{\partial x}}{\left(g(x)-f(x)\right)^3}\right)\partial x \tag{16}$$

The first term of this equation is the same as the previous analysis (equation 5). The inertial integral is not trivial to solve, however, once the trigonometric profile (equation 6) is applied. Examining the limits of this analysis can indicate the potential usefulness of this augmented analysis. If inertia were negligible, as with low Reynolds number flows, this formulation would limit back to the lubrication approximation equation (equation 5). Similarly, in the smooth wall case, *f*(*x*) and *g*(*x*) are constants, the derivatives of which are zero. The inertial integral will then yield a negligible constant. Thus, the formulation is consistent with the boundary layer analysis for the case of hydraulically smooth walls. Overall, these limits indicate that the analysis has potential as an improvement upon the initial analysis, and may be a starting point for future work.

## 3.6 Application of Theory

In order to test the theoretical pressure loss equation (equation 5) and to compare it with existing laminar flow models, friction factors must be evaluated for varying Reynolds numbers. To this end, the pressure-loss form of the Darcy-Weisbach equation, or Darcy friction factor, was used to calculate experimental friction factors:

$$f = \frac{\Delta P}{L} \frac{D_h}{2\rho} \left( \frac{Q}{A} \right)^2 \tag{17}$$

where $D_h$ is the hydraulic diameter, calculated as four times the cross-sectional area divided by the wetted perimeter:

$$D_h = \frac{2ab}{a+b} \tag{18}$$

The Darcy-Weisbach equation was also used to calculate theoretical friction factors with $\Delta P$ obtained from the wall function method. For comparison with conventional laminar theory, the correlation for friction factors in smooth, rectangular ducts, from Kakaç *et al*. [51], was also evaluated:

$$f = \frac{24}{\mathrm{Re}}(1 - 1.3553\alpha + 1.9467\alpha^2 - 1.7012\alpha^3 + 0.9564\alpha^4 - 0.2537\alpha^5) \tag{19}$$

where the aspect ratio is calculated as the channel width divided by channel height:

$$\alpha = \frac{b}{a} \tag{20}$$

Reynolds number was calculated as:

$$\mathrm{Re} = \frac{\rho Q D_h}{\mu A} \tag{21}$$

The hydraulic diameter and cross-sectional area may be "constricted" by using the constricted separation in place of the root separation. Similarly, Reynolds number may be constricted by using the constricted hydraulic diameter and area. Constricted friction factors may be calculated by using constricted geometry, as well as the constricted form of equation 10 for pressure drop.

# 4 Preliminary Results

This chapter presents the results of comparison of available data with the theoretical model, prior to the design and manufacture of a new test set and roughness pieces. In addition, the roughness profile, equation 6, was evaluated in order to optimize the profile and understand the effects of each variable on roughness amplitude parameters.

## 4.1 Saw-tooth Roughness

Experimental data from previous tests by Brackbill [44] were used for comparison with the wall function method detailed above. Initial validation of the experimental setup was reported for the hydraulically smooth channel case. Channel separation values were 200, 300, and 500 μm. Flow rates in these experiments were varied to cover the range of Reynolds numbers from 487 to 2322. Friction factors were calculated by Brackbill using equation 19 for laminar theory and the constricted Darcy friction factor for experimental values. Figure 6 shows the comparison between Brackbill's experimental data for hydraulically smooth channels and the smooth channel correlation (Equation 19). For each of these three channel separations, error was less than 4% at all flow rates.

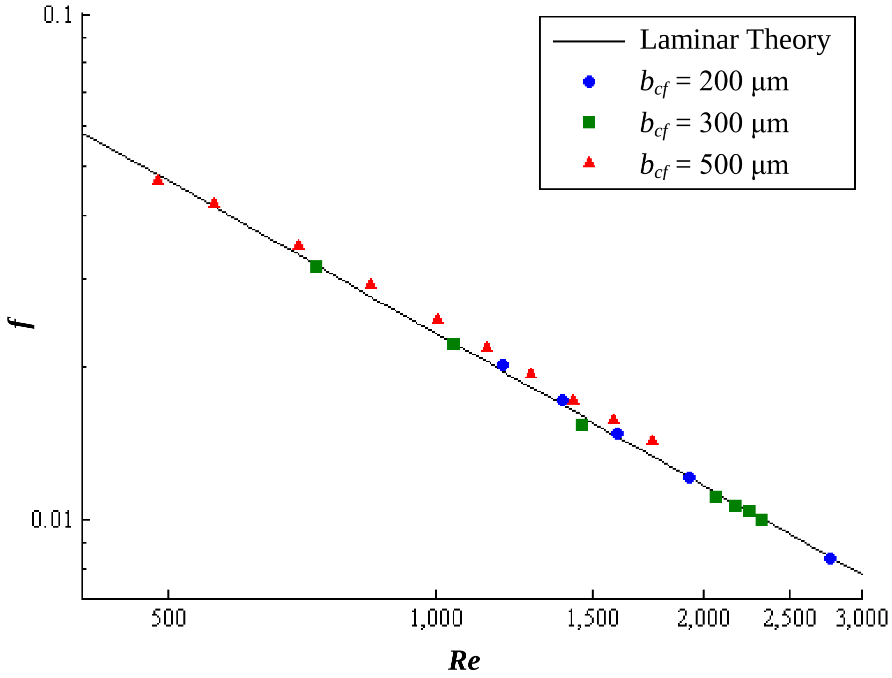

**Figure 6. Smooth Channel Validation of Previous Experimental Setup**

The style of two-dimensional roughness examined by Brackbill is referred to as "saw-tooth" roughness. The surfaces possessed evenly spaced peaks, and were described by the roughness height and pitch. A sample of profilometer data from one such saw-tooth surface is shown in Figure 7 below. This surface would form one wall of a channel, as shown in Figure 5.

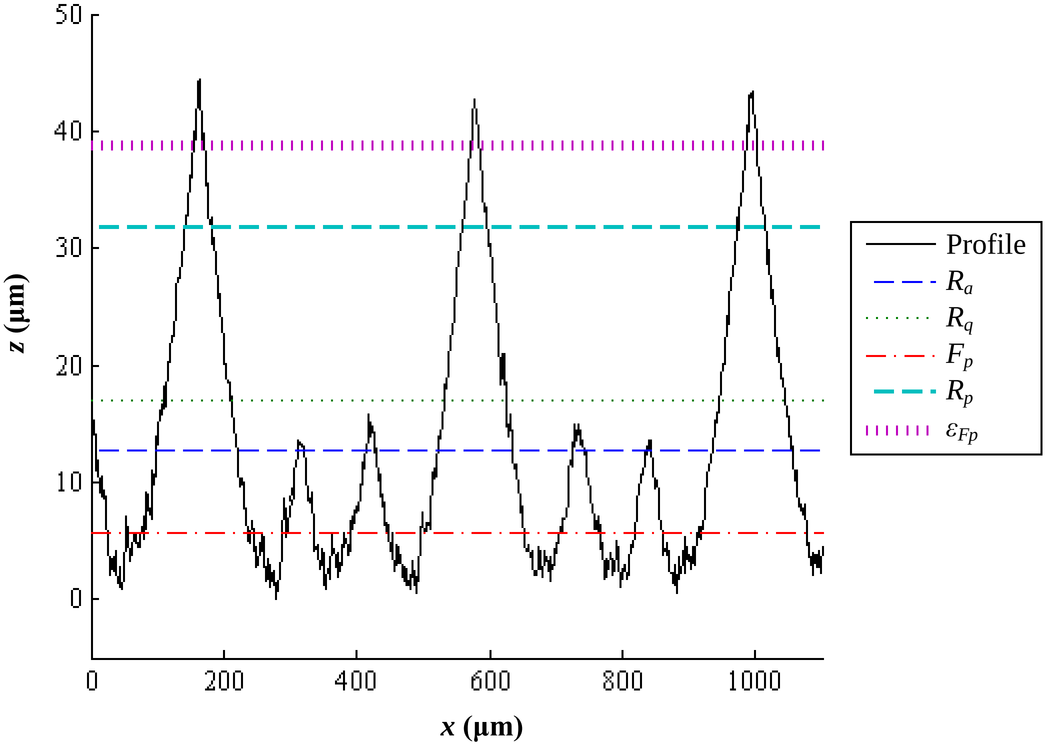

**Figure 7. Saw-tooth Roughness Profile with Height Parameters, $\lambda$ = 503 µm**

This figure includes the standard average amplitude parameters, $R_a$ and $R_q$, as well as the constricted parameter $\varepsilon_{Fp}$ and its components, $R_p$ and $F_p$, obtained from the profilometer data. It is shown that of all these parameters, none fully account for the peak heights, though the constricted parameter is closest. The peaks for this surface were designed to be 50 µm tall, but the constricted parameter was found to be 38.75 µm. Amplitude parameters do not account for the distance between the major peaks, so it becomes necessary to use spatial parameters. However, due to the smaller peaks between those major peaks, on the order of 20 µm tall, the standard spatial parameters were incapable of characterizing the major peaks. The roughness between the major peaks has the added effect of skewing height parameters and complicating the measurement of the root channel separation.

In order to apply the wall function method, the "saw-tooth" surfaces were fit with smooth, continuous polynomials. This was achieved by examining the profiles and formulating sinusoidal functions that fit the curvature. Through a series of curve-fitting exercises, initially using complex combinations of trigonometric functions, it was quickly determined that the minor peaks could not be accounted for by any continuous stable function, and so equation 6 was developed. Leaving all coefficients as variables, the least sum of squares method was used in conjunction with Excel's Solver tool to obtain a best fit. A sample image of the same profilometer data shown in Figure 7 and its corresponding curve-fit are shown below in Figure 8.

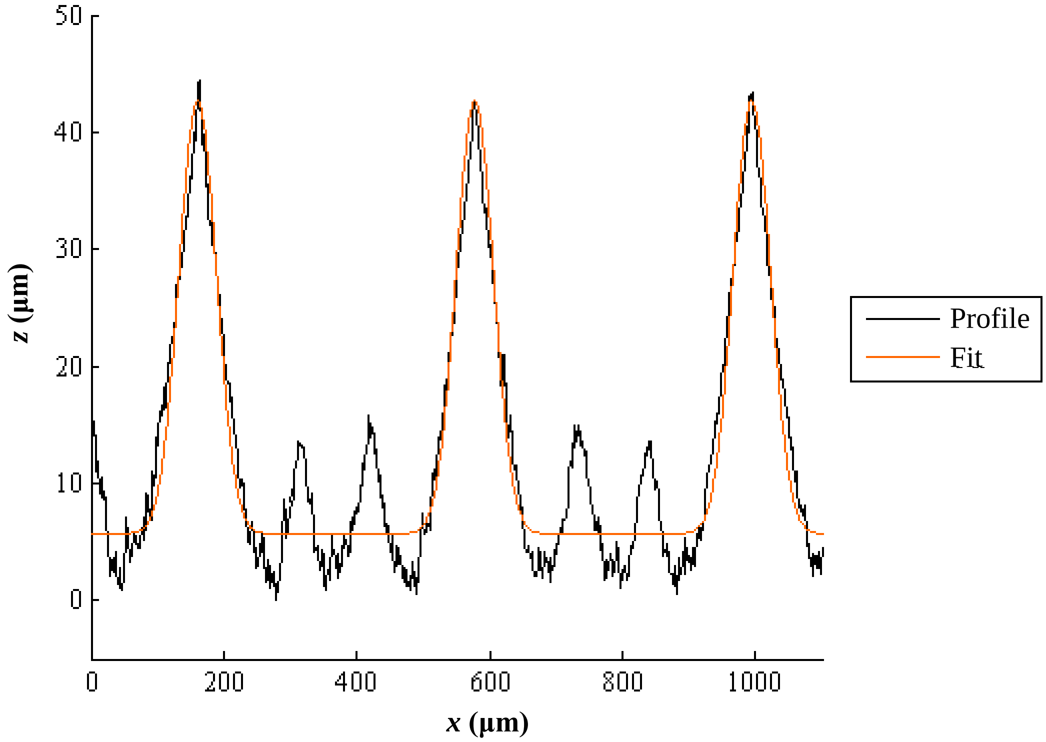

**Figure 8. Curve Fit of 503 µm Pitch Saw-tooth Roughness Profile**

Figure 8 is one example of a smooth curve of the form of equation 6 (shown in orange) fit to profilometer data from saw-tooth roughness (shown in black). The height obtained for the curve fit of this profile is 37.2 µm and the pitch is 416.7 µm. The "floor" of the profile was taken to be the same as the $F_p$ parameter, shown in Figure 7, but was allowed to vary slightly in order to obtain a best fit. Although the difference between the curve fit and the surface data was minimized, it is clear that it does not provide a perfect fit as it neglects the roughness in the valleys between the major peaks. This minor roughness may be non-negligible in microscale flows, particularly considering interactive flow.

Though the curve does not provide an exact fit, the friction factors obtained through the wall function method provided an excellent prediction of the channel's hydraulic performance for two channel separations. The two figures below show the un-constricted laminar experimental data obtained by Brackbill [44] for two channel separations of the 503 µm pitch surface; *b* = 300 and 400 µm. The plots include the conventional laminar theory line (equation 19), and the line predicted by the wall function method based on the curve fit of Figure 8.

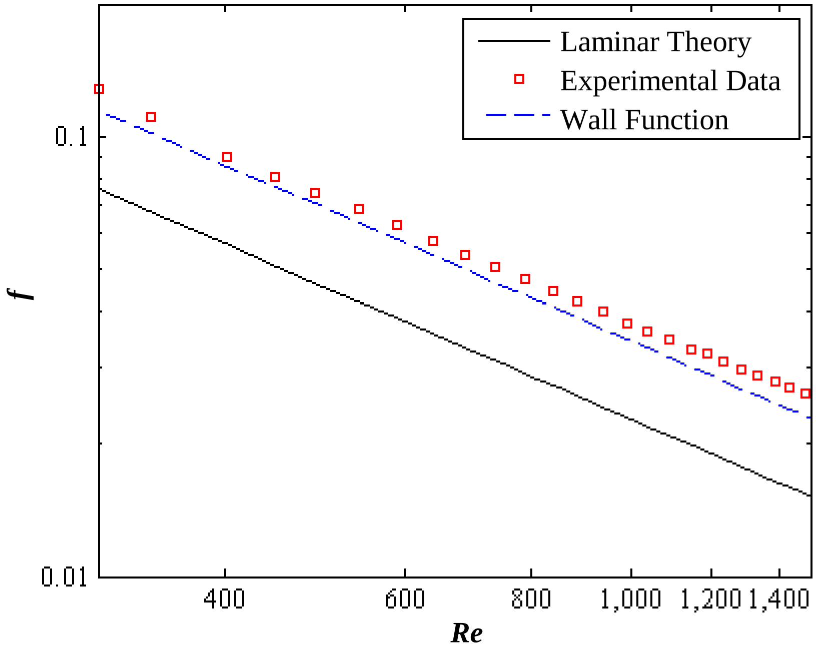

**Figure 9. *f* vs. *Re* for 503 µm Pitch Surface, *b* = 400 µm**

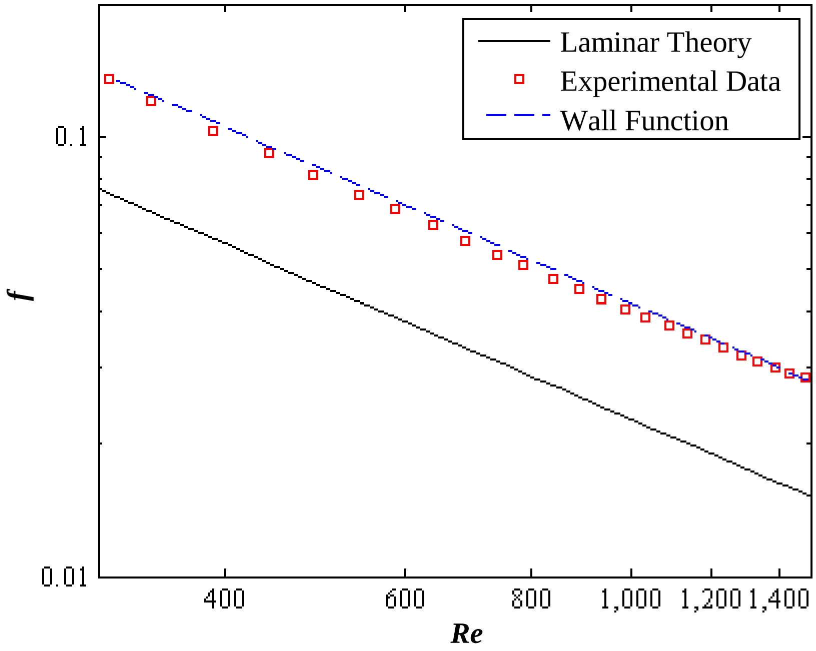

**Figure 10. *f* vs. *Re* for 503 µm Pitch Surface, *b* = 300 µm**

The experimental data for $b$ = 300 µm are an average of 76% greater than the friction factors predicted by laminar theory, and for $b$ = 400 µm about 65% greater. The data fits the lines predicted by the wall function method to within 4% for $b$ = 300 µm and within 10% for $b$ = 400 µm. However, the wall function method under-predicts the 400µm channel size case and over-predicts the 300 µm. This may be due, in part, to the roughness between peaks, discussed previously.

Other surfaces were measured, fitted with polynomials, and compared with the wall function method, but none compared as well as the 503 µm pitch surface. This was due to the increase in roughness between peaks as the pitch increased. The minor roughness made it difficult to identify the floor of the profile and thus the root channel separation. It also had the effect of skewing amplitude parameters so that they were significantly lower than the actual peak height. The overall effect of this minor roughness on the flow data obtained by Brackbill is unknown.

It should be noted that the wall function method was developed based on the lubrication, or small-slope approximation, which implies that the slope of the roughness at any point is small. The profile shown previously clearly does not fit this category. The limits of the lubrication approximation were tested not only by increasing the roughness height but also by the inclusion of minor roughness in between the major peaks. In order to properly validate the theoretical model defined herein, surfaces were designed and manufactured to fit precisely to the power sinusoid of equation 6.

## 4.2 Idealized Roughness

Before using the wall function method to assess flow in the presence of idealized structured roughness, the roughness profiles themselves were analyzed numerically in order to understand the effect of pitch and height on certain amplitude parameters. Equation 6 was studied by systematically varying each variable and evaluating the effect on the average roughness $R_a$ and RMS roughness $R_q$, as well as the constricted parameter $\varepsilon_{Fp}$ and its components, $F_p$ and $R_p$. For reference, Figure 5 shows a sample of the roughness studied in this section.

Initially, the height of roughness elements was maintained at $h$ = 50 µm and pitch was varied such that $\lambda/h$ ranged from 2 to 12, in order to envelop the “transitional” roughness identified by Coleman *et al*. [37]. It was immediately apparent that if the power on the sinusoid was not varied as well, the slope of the peaks became shallower as pitch increased. The result was that all roughness parameters remained approximately constant, varying by no more than half a micron, when the height and power were held constant and pitch was varied. This indicated that the existing parameters are very weak functions of roughness pitch, but may be strongly affected by the power or slope of peaks. The study was repeated for a constant pitch of 250 µm, keeping the power constant and varying the height such that $\lambda/h$ ranged from 2 to 12 once again. The results are shown in Figure 11 below.

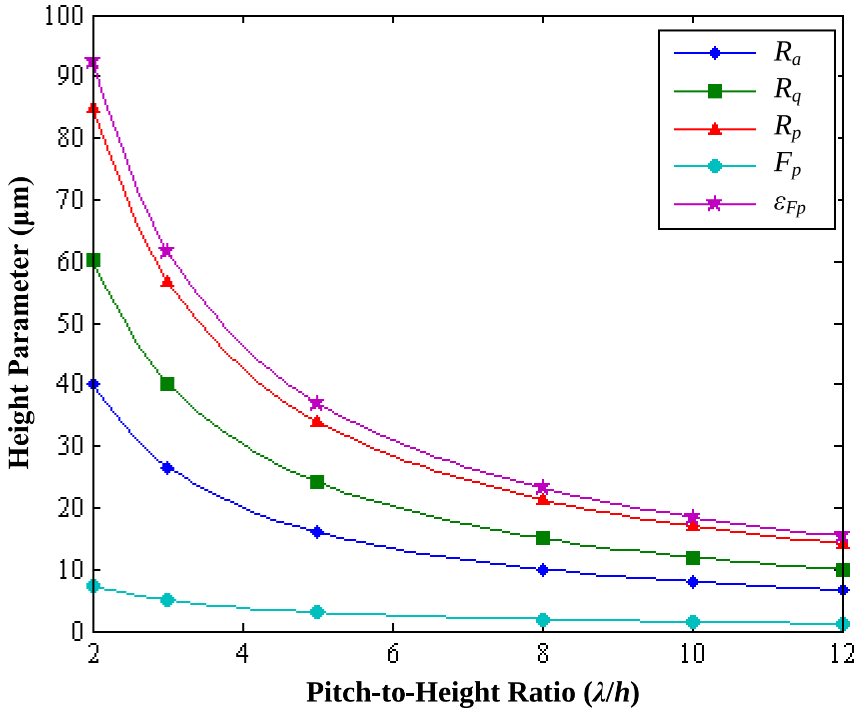

**Figure 11. Roughness Parameters vs. $\lambda/h$ for $\lambda$ = 250 µm and $p$ = 6**

As the roughness height decreased, all parameters decreased asymptotically. This is to be expected for amplitude parameters, as they are direct functions of roughness height. Note that for this style of idealized roughness, there is very little difference between the constricted parameter and peak height $R_p$. This is due to the smoothness of the profile between the peaks, evidenced by the low $F_p$ value.

In the next pair of studies, the power was varied such that the roughness peaks maintained the same curvature and slope from the base of the peak to about halfway up the roughness element. This was achieved by plotting the profiles on the same coordinates and observing that there was sufficient agreement between them, as shown in Figure 12. Additionally, the least sum of squares method was used to minimize the difference between the small segment of the profiles from $x$ = 10 to 50 µm.

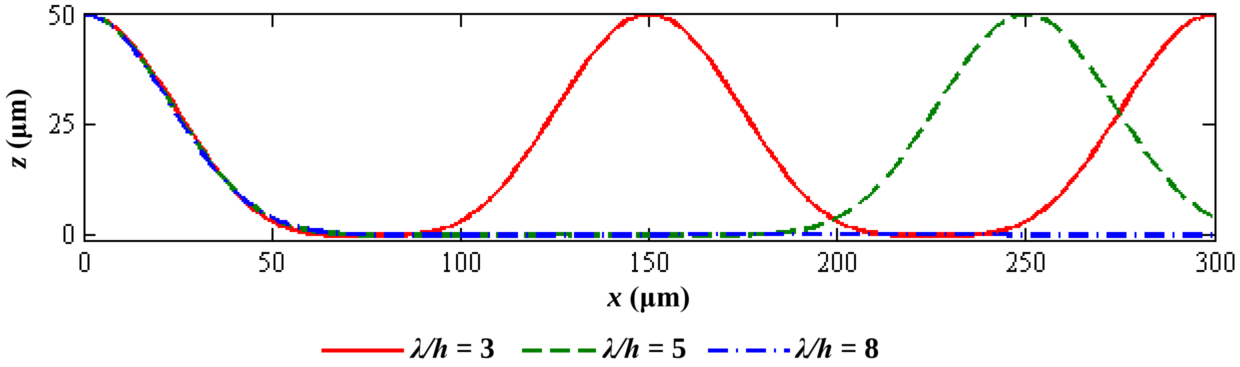

**Figure 12. Ideal Surface Roughness Profiles for *h* = 50 µm, *λ* varies, *p* varies**

This process of varying the cosine power was applied to a series of profiles with a constant pitch of $\lambda$ = 250 µm, varying the height $h$ such that the same pitch-to-height ratios were obtained. Figure 13 illustrates the effect of varying the power to keep the roughness slope the same.

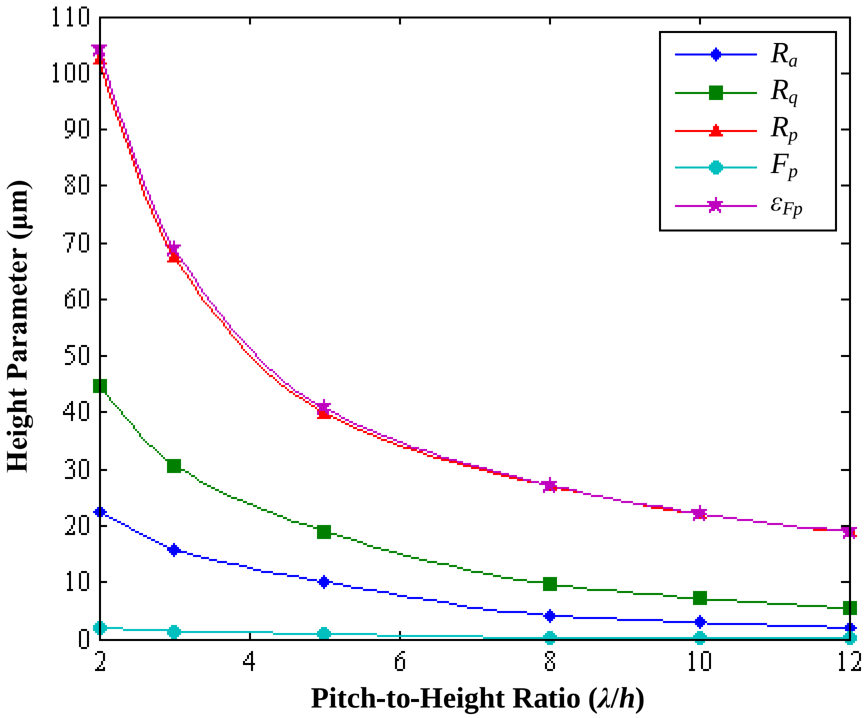

**Figure 13. Roughness Parameters vs. *λ*/*h* for *λ* = 250 µm, *p* varies**

Comparing Figure 13with Figure 11, the primary effect of maintaining similar roughness slopes that it decreases the average amplitude parameters and the floor profile, and increase the constricted and peak height parameters. The constricted parameter and peak height are essentially the same in this case. In general, the profiles are "cleaner" or more consistent from one to the next, as was seen in Figure 12, and as evidenced by the minimal floor profile parameter.

In this next study, roughness height was held constant at 50 µm. Pitch was varied as before, to obtain the same pitch-to-height ratios, and power was varied as described above. A summary of the roughness values obtained is shown in Figure 14.

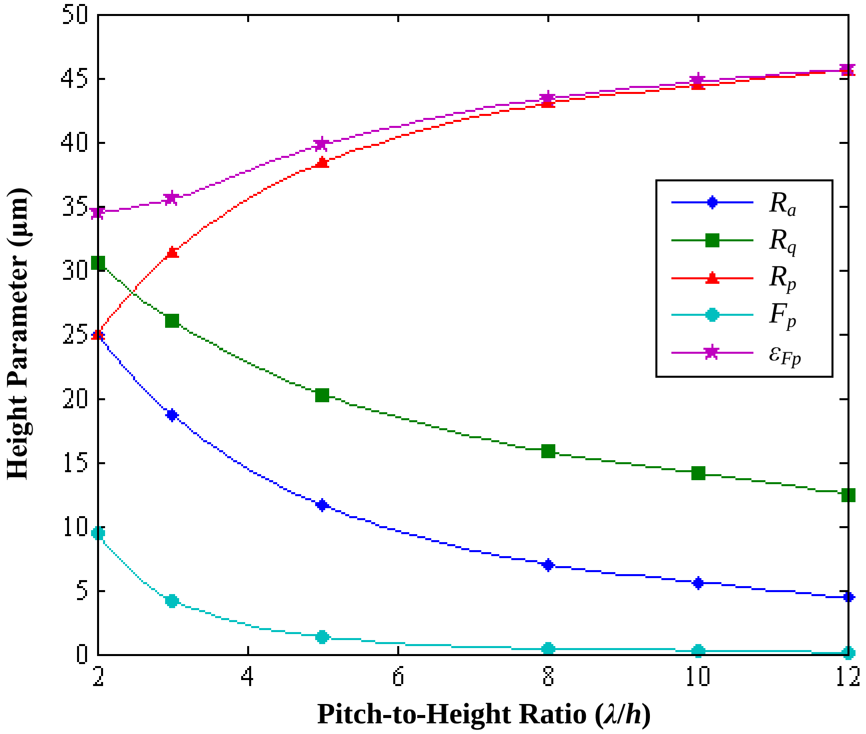

**Figure 14. Roughness Parameters vs. *λ*/*h* for *h* = 50 µm, *p* varies**

As the roughness pitch increases, the average amplitude parameters $R_a$ and $R_q$ decrease while the constricted parameter $\varepsilon_{Fp}$ and peak height $R_p$ increase. This is due to the decrease in the density of asperities on the surface, indicating that the constricted parameter is more sensitive to these extreme peaks than the exiting average parameters. For smaller pitch-to-height ratios, there is a significant difference between the constricted parameter and peak height, as the floor profile parameter $F_p$ increases with peak density (as pitch decreases). But as pitch increases, $F_p$ diminishes, resulting in $\varepsilon_{Fp}$ and $R_p$ converging toward the designed height of 50 µm.

The results of this analysis indicate that, in general, all amplitude parameters investigated are sensitive to both pitch and height, particularly in the event that the roughness peaks are closely spaced, or $\lambda/h$ is small. The sinusoid power also has a strong effect on the cases of closely spaced roughness. The constricted parameter $\varepsilon_{Fp}$ and peak height $R_p$ are better suited to this style of structured or transverse rib roughness than are the average parameters $R_a$ and $R_q$, The average and RMS roughness may be sufficient, however, in the case of low roughness height and large pitch-to-height ratio, as seen in Figure 11. The primary point of interest here is that the amplitude parameters all exhibit asymptotic behavior as pitch, height, and power are varied, in that the parameters limit to constant values in either $\lambda/h$ extreme.

In the literature review, it was noted that the $\lambda/h = 8$ case is considered “transitional” roughness, and has been identified as having the greatest effect on fluid flow. For the constricted flow model, this would imply that the roughness values reach a maximum at $\lambda/h = 8$, and decrease on either side of that point. It is hoped that the wall function method developed here will be an improvement on conventional theories in that respect.

## 4.3 Friction Factors

Knowing that the wall function method varies with roughness geometry, it is of interest to understand the behavior of the wall function method, the constricted flow method, and smooth channel correlation as different roughness parameters vary. In this section, all three formulations are assessed for varying channel aspect ratios, Reynolds numbers, and roughness geometries. Channel height was chosen to be 12192 µm, from the experiments of Brackbill [44], and the separation values were 150 µm, 200 – 1000 µm in 100 µm increments, 2000 – 10000 µm in 2000 µm increments, and 12192 µm.

First, equation 19, the correlation for laminar flow in smooth rectangular ducts was evaluated for a range of aspect ratios and Reynolds numbers. The behavior of equation 19 is illustrated in Figure 15 below. Aspect ratios ranged from 0 to 1, where $\alpha = 1$ indicates a square channel and, though an aspect ratio of zero is not physically possible, as $\alpha$ approaches zero, the channel becomes a narrow slot or very closely spaced, infinite parallel plates. Figure 15 shows that friction factor is highest for the lowest aspect ratios, and decreases asymptotically as $\alpha$ approaches 1. For example, at a Reynolds number of 50, the friction factor limits to $f = 0.2846$ at $\alpha = 1$. The plot also shows that the friction factor increases more sharply at low aspect ratios if the Reynolds number is lower, or flow is very laminar. For a Reynolds number of 150, for example, there is little difference between the friction factor for a square channel and narrow slot. As Reynolds number increases further, the laminar friction factor ceases to be a function of aspect ratio, or remains approximately constant, and approaches zero. This equation does not vary significantly with surface roughness, as changes in surface roughness result in minimal changes to the channel aspect ratio and Reynolds number, as described with Figure 16.

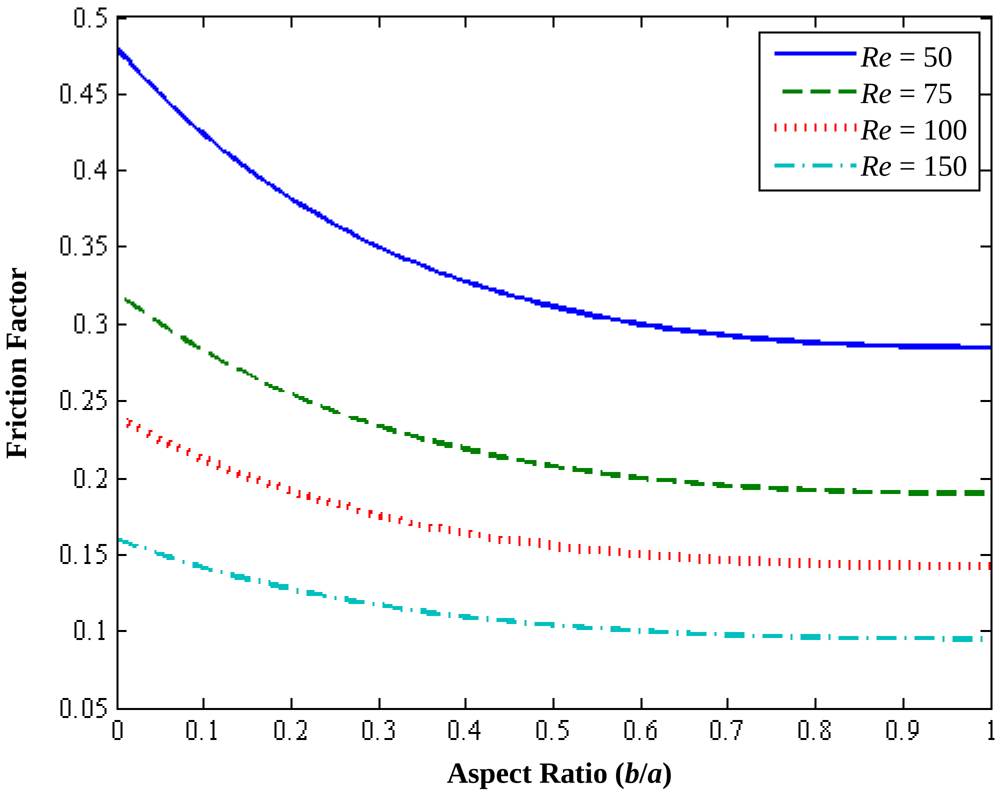

**Figure 15. Friction Factor vs. Aspect Ratio, Smooth Channel Correlation**

The constricted form of equation 19 was evaluated by obtaining a constricted aspect ratio and Reynolds number for each scenario. A series of values for $\varepsilon_{Fp}$ were chosen, ranging from 20 to 100 μm, in 20 μm increments. Constricting the aspect ratio and Reynolds number proved to have little effect on the friction factor compared with the un-constricted form of the equation, however, as a small change in roughness height has minimal effect on the aspect ratios, particularly as the aspect ratio increases. Figure 16 is a plot of the constricted from of equation 19 for an un-constricted Reynolds number of 50 and three representative $\varepsilon_{Fp}$ values. Varying the Reynolds number has the same effect as seen in Figure 15, thus only one Reynolds number is shown in Figure 16, so as to highlight the effect of varying $\varepsilon_{Fp}$.

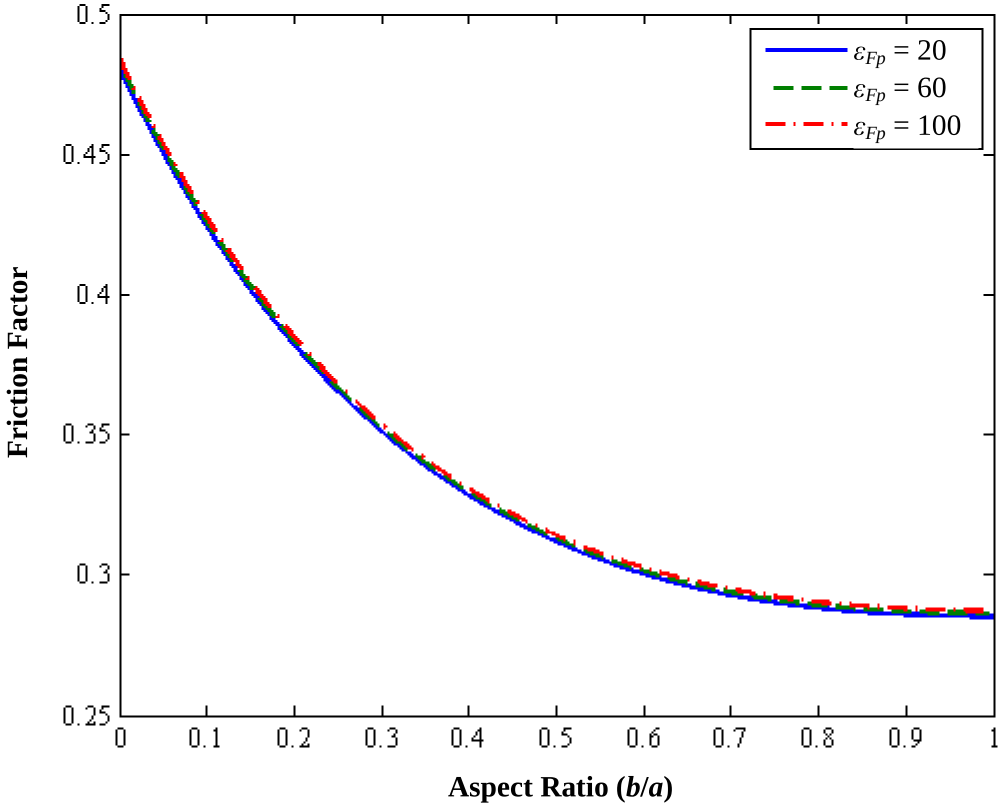

**Figure 16. Friction Factor vs. Aspect Ratio, Constricted Flow Method, *Re* = 50**

As illustrated by Figure 16 above, the friction factor lines for varying roughness heights differ very slightly for narrow channels. The difference between fiction factors for $\varepsilon_{Fp}$ = 20 and 100 µm, for example, is approximately 1.6% for small aspect ratios and decreases to 0.7% as $\alpha$ approaches 1. Percent error between the constricted and un-constricted forms of equation 19 was found to be about 0.2% at low aspect ratios, and decreased to zero as aspect ratio increased, for all $\varepsilon_{Fp}$. For this reason, the un-constricted laminar friction factor (equation 19) was used for further comparison in the study of the wall function method, and for comparison with experimental data.

To assess the behavior of friction factors obtained from the wall function method, idealized surfaces based on equation 6, identical to those shown in Figure 12, were modeled with a constant height of $h$ = 50 µm. The roughness pitches modeled were $\lambda$ = 100, 150, 250, 400, 500, and 600 µm. The corresponding pitch-to-height ratios for these surfaces are $\lambda/h$ = 2, 3, 5, 8, 10, and 12. The cosine power was varied, as described in the Idealized Roughness section, so that the slope was relatively constant across all profiles. These wall function variables were entered into the MATLAB code, shown in Appendix A. Fluid density and viscosity were held constant for all simulations. Reynolds number was used for the input parameter associated with flow rate in this version of the code, and the volumetric flow rate was calculated based on channel geometry, fluid properties, and Reynolds number. For this analysis, Reynolds number was set to 50, and channel separations ranged from 150 to 12192, as described at the beginning of this section. The evaluation length was set to 1.0 inch, to match the distance between pressure taps in prior experiments. The theoretical pressure drop was evaluated in MATLAB using equation 5 and the wall functions, equation 6. The pressure drop was then incorporated into equation 17 for friction factor. The results of this exercise are plotted on a log-log graph, in Figure 17 below, in order to magnify the behavior of wall function friction factors in the low aspect ratio range.

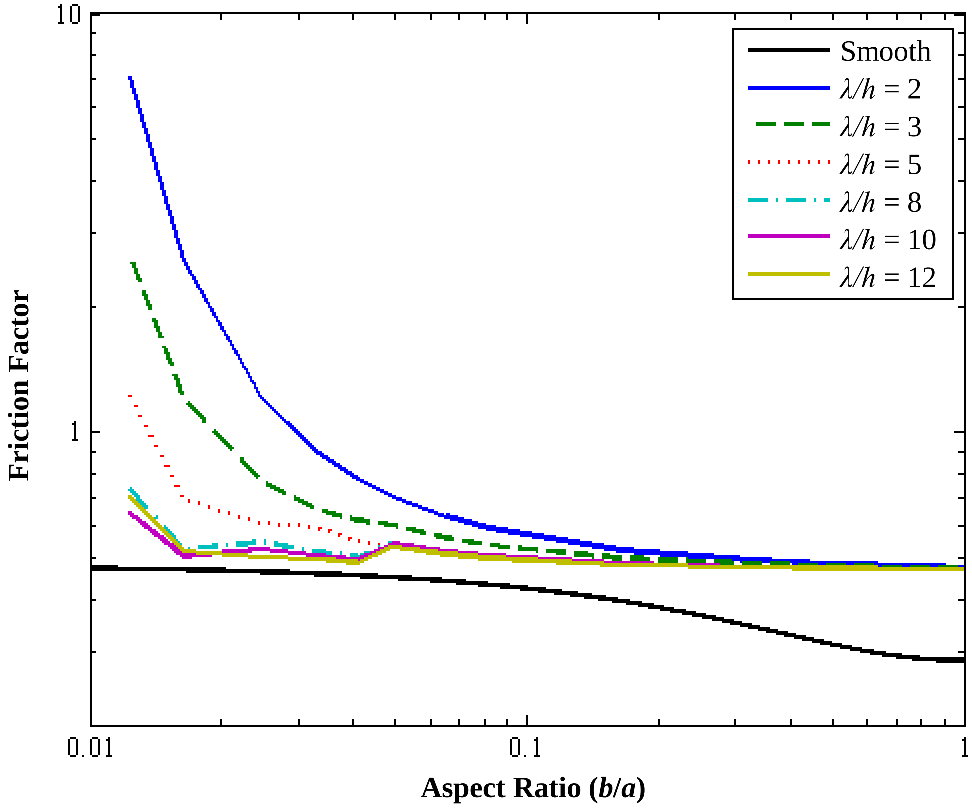

**Figure 17. Friction Factor vs. Aspect Ratio, Wall Function Method, *Re* = 50**

The "Smooth" line shown in Figure 17 was calculated using equation 19, and is the same as the line plotted in Figure 15 for *Re* = 50. This line was plotted for smooth channel comparison because the wall functions studied here were for a constant roughness height. It was found that setting the wall functions *f*(*x*) and *g*(*x*) to constant values, or setting h = 0, resulted in friction factors within 1.2% of smooth channel theory.

This plot is intended to display the comparative behavior of the wall function method and the smooth channel correlation. Like the smooth channel correlation, the friction factors predicted by the wall function method decrease as Reynolds number increases, as discussed previously for Figure 15. At the low end of aspect ratios, both theories predict higher friction factors, so they agree that friction factor is greater in taller/narrower channels. The roughness height was held constant for this study, and the small pitch-to-height ratios indicate very closely spaced roughness, for which the wall function method predicts very high friction factors. As roughness spacing increases on the low channel aspect ratio end, the wall function method appears to converge toward the smooth channel correlation (see $\lambda/h$ = 10 and 12 in Figure 17). As channel aspect ratio increases toward a square channel, the wall function decreases asymptotically to a friction factor of 0.5 for all roughness profiles. This is higher than the smooth channel correlation predicted, but the value decreases towards the smooth channel correlation as roughness height decreases. This view of the wall function method's behavior may be indicative of its range of applicability, and in fact reinforces the theoretical methods used to obtain this theory, as one of the assumptions for the analysis was that the channel separation is significantly less than the channel height.

In the range of lower channel aspect ratios and higher roughness pitch-to-height ratios, the wall function method exhibits some instability. The friction factor lines for the three pitch-to-height values $\lambda/h$ = 8, 10, and 12 are nearly indistinguishable, and in fact the $\lambda/h$ = 12 profile resulted in friction factors greater than the $\lambda/h$ = 10 surface for the smallest three aspect ratios modeled. As Reynolds number varies, this instability neither increases nor diminishes. The instability may be due, in part, to the increase in cosine power as roughness pitch increases. High pitch-to-height ratios are representative of low relative roughness, so the instability in this range may indicate that the wall function method will be less accurate as roughness decreases and the user should revert to the conventional smooth channel correlation.

In addition to the wall function method, the constricted flow method was used in predicting hydraulic performance for each of these scenarios. The code in Appendix A includes the constricted flow approach at the end, with the added ability to switch between using the constricted flow parameter or average roughness for the analysis. It was hoped that evaluating the constricted pressure drop would provide some improvement over the constricted form of equation 19. The results of the constricted flow analysis showed that this method is incapable of predicting friction factors that differ from the smooth channel correlation, as was discussed with Figure 16. The greatest difference observed between the constricted flow method and the equation for smooth channels was, as the channel separation increased, the friction factors obtained from the constricted flow method became increasingly lower than those predicted by the smooth channel correlation.

The overall outcome of this systematic study of friction factor behavior is that the wall function method appears to be most effective in the case of low channel aspect ratios and low roughness pitch-to-height ratios. Above channel aspect ratios of 0.1, friction factors obtained from the wall function method converge to a value much higher than predicted by the smooth channel correlation. But, as channel size increases, the roughness effect on flow is expected to diminish. The same is true for high roughness pitch-to-height ratios, in that the sparse roughness elements result in flow over independent obstructions rather than through a rough channel. Therefore, it was concluded that further work on the wall function method shall be focused on smaller channel separations and lower roughness pitch-to-height ratios.

## 4.4 Flow through Channels Possessing Idealized Roughness

Analysis of flow in the presence of the two-dimensional roughness was performed on the same idealized surfaces discussed in the previous section. The format of equation 6 was used for the wall functions, where $h$ was held at a constant value of 50 μm, and $\lambda$ was varied such that $\lambda/h$ = 3, 5, 8, and 10. The root channel separation values modeled were 150 μm, and 200-600 μm in 100 μm increments. Channel height was fixed at 12192 μm, as before. Reynolds number ranged from 5 to 3400. All roughness parameters for these theoretical surfaces were calculated in the roughness analysis performed prior. The range of profiles and channel separations resulted in relative roughness values, $\varepsilon_{Fp}/D_h$, ranging from 3-15%.

For a constant channel separation, as $\lambda/h$ increases (or relative roughness decreases) the wall function method converges toward laminar theory for smooth rectangular ducts. An example of this convergence can be seen in Figure 18, which shows friction factors versus Reynolds number for each surface modeled, when channel separation was held constant at 150 μm. The smooth channel correlation, shown in black, was calculated using equation 19. Higher values of $\lambda/h$ indicate lower roughness effect on fluid flow, in that the peaks become isolated flow obstructions rather than periodic roughness, eventually limiting to the hydraulically smooth case. As roughness pitch decreases, the increase in friction factor is more pronounced, as seen in the differences between the "Smooth" line and $\lambda/h = 3$ and = 5.

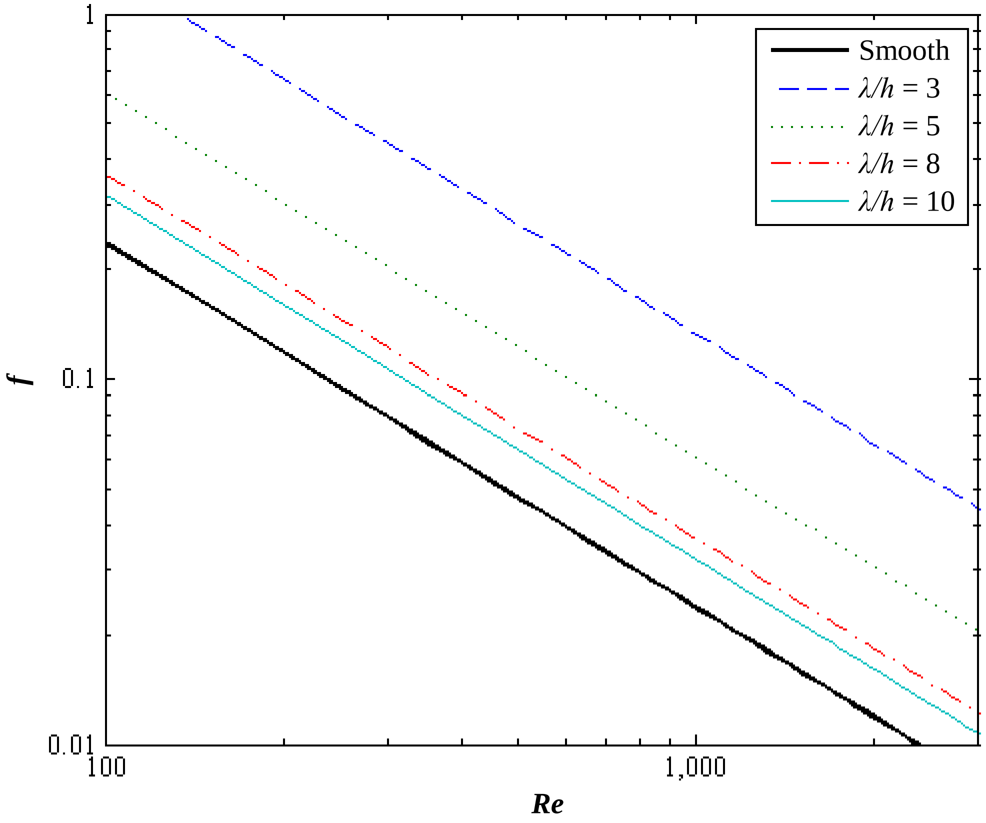

**Figure 18. Comparison of Wall Function Method with Smooth Channel Correlation, for Channel Separation *b* = 150 µm**

Figure 19 shows a plot of friction factor versus Reynolds number for a single surface, $\lambda/h = 5$, and four different channel separations; $b$ = 150, 200, 300, and 500 µm. For any given roughness profile, as the channel separation increases from microscale to macroscale, the wall function method again converges to the smooth channel correlation for rectangular ducts. This is because microscale roughness has minimal effect on the bulk flow in larger scale channels [36]. In these cases, aspect ratio increases minutely with the increase of separation from 150 µm to 600 µm, because the channel height is significantly greater than the width, and so the corresponding decrease in the smooth channel friction factor is 1.2%. The smooth correlation lines in Figures 18 and 19 correspond with the 150 µm channel separation.

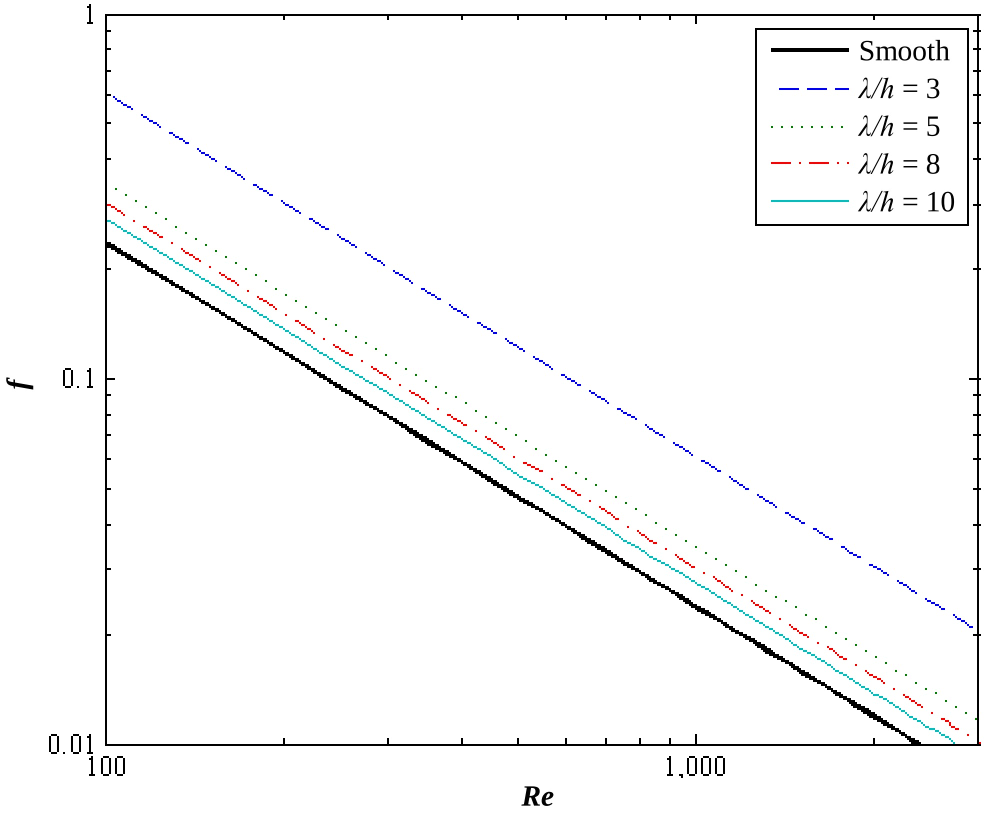

**Figure 19. Comparison of Wall Function Method with Smooth Channel Correlation, for Surface Profile *λ*/*h* = 5**

In general, it was shown using the wall function method that for larger hydraulic diameters and larger $\lambda/h$ ratios, i.e., lower relative roughness ($\varepsilon_{Fp}/D_h < 5\%$), the friction factor deviates little from the correlation for laminar flow in smooth rectangular ducts. As the channel separation decreases, the roughness height becomes of the same order of the channel separation, resulting in a significant increase in roughness effect, evident in the plots discussed previously. For large roughness pitch values, this effect is not evident until the ratio of roughness height to channel separation $h/b$ is at least 0.25. For lower values of $\lambda/h$, the difference between the wall function method and laminar theory is significant for $h/b \approx 0.08$.

# 5 Experimental Setup

In order to assess the validity of the theoretical analysis, and thereby test the limits of the applied assumptions and approximations, it is necessary to perform experiments with fluid flow in the roughness and channel geometries studied in the previous sections. Surfaces designed based on equation 6 were generated in stainless steel and evaluated using a Keyence laser confocal microscope. A complete experimental apparatus and test loop was also developed for testing. The test components will be discussed in the following subsections.

## 5.1 Design Parameters

A universal test matrix was developed to ensure geometric similitude across all experimental, theoretical, and numerical analyses associated with the project. Summaries of the test matrix for roughness parameters and channel geometry are shown in Table 1 and Table 2, respectively. The complete design test matrix, as it applies to this work, can be found in Appendix B.

**Table 1. Test Matrix Summary: Roughness Geometry - Designed**

| **Pitch** | **Height** | **Power** | **Pitch-to-Height Ratio** |
|---|---|---|---|
| $\lambda$ | $h$ | $p$ | $\lambda/h$ |
| **µm** | **µm** | **---** | **---** |
| 250 | 125 | 4 | 2 |
| 150 | 50 | 4 | 3 |
| 250 | 50 | 12 | 5 |
| 250 | 31.25 | 4 | 8 |
| 400 | 50 | 32 | 8 |

**Table 2. Test Matrix Summary: Channel Geometry - Designed**

| **Separation** | **Hydraulic Diameter** | **Aspect Ratio** | **Separation-to-Length Ratio** |
|---|---|---|---|
| $b$ | $D_h$ | $\alpha$ | $b/L$ |
| **µm** | **µm** | **---** | **---** |
| 250 | 480 | 0.02 | 0.002 |
| 450 | 850 | 0.04 | 0.003 |
| 600 | 1118 | 0.05 | 0.004 |
| 800 | 1600 | 0.06 | 0.005 |
| 1000 | 1964 | 0.08 | 0.007 |

The three variables employed in equation 6, pitch, height, and power, are shown in Table 1 above. Values for pitch and height were chosen so as to include both *d*- and *k*-type roughness, and to envelope the spectrum of *d*- and *k*-types of roughness, as discussed in the literature review. The values for the cosine power were obtained through plotting exercises, as described in the Preliminary Results section. The pitch-to-height ratios ranged from 2 to 8, as ratios equal to or greater than 10 have been identified as isolated flow obstructions, and would be expected to have a minimal effect.

Channel height was fixed at 12.70 mm and length at 152.4 mm. Separation values were chosen based on the requirements of the theoretical development, including that the channel separation must be significantly less than its length; $b \ll L$ or $b/L \ll 1$, and the channel separation must be significantly less than the height; $b \ll a$ or $\alpha \ll 1$. Table 2 shows that both of these are satisfied by the chosen channel separations. For graphic representations of the channel and roughness geometries, please refer to Figure 1 and Figure 2 in section 3.1.

## 5.2 Structured Roughness

Roughness was designed and manufactured per the test matrix in stainless steel via wire EDM. Pairs of test pieces were made for each profile so the channels constructed from these parts would have two identical rough walls, as in the theoretical analysis. A sample of one of the profiles submitted for manufacture is shown in Figure 20. Since the manufacturer required a solid model of the parts, data points from segments of each profile were imported into SolidWorks to create a spline, and the entire profile was patterned along the length of the part. Two-dimensional drawings of the roughness test pieces were also created and can be found in Appendix C.

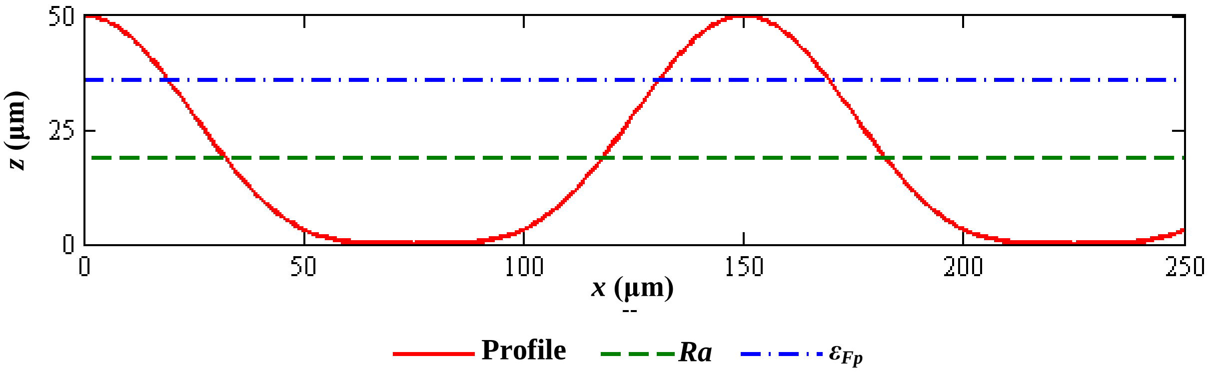

**Figure 20. Designed Roughness Profile, $h$ = 50 µm, $\lambda$ = 150 µm**

The method of wire EDM was chosen based on the need for precise patterning on the roughness test pieces, and the complex shape of the gauge blocks (discussed later). One of the drawbacks to this method was the size of wire used in the process, 101.6 µm, which limited the minimum roughness pitch allowable. Another difficulty was the severe deformation of the initial batch of roughness pieces. This was prevented in the second and subsequent batches by stress-relieving the steel plate from which the parts were cut.

Once the test pieces were obtained, they were cleaned by rinsing with methanol, acetone, IPA, and water sequentially, blowing the surfaces dry with compressed air between rinses. Multiple sample lengths of each surface were then scanned on the laser confocal microscope, which has a resolution of 1 nm. A total of 5 scans were taken for each test piece, or 10 scans per roughness profile, at even and consistent intervals. A sample 3-D image result from the microscope is shown in Figure 21. This surface was manufactured from the submitted profile show previously in Figure 20.

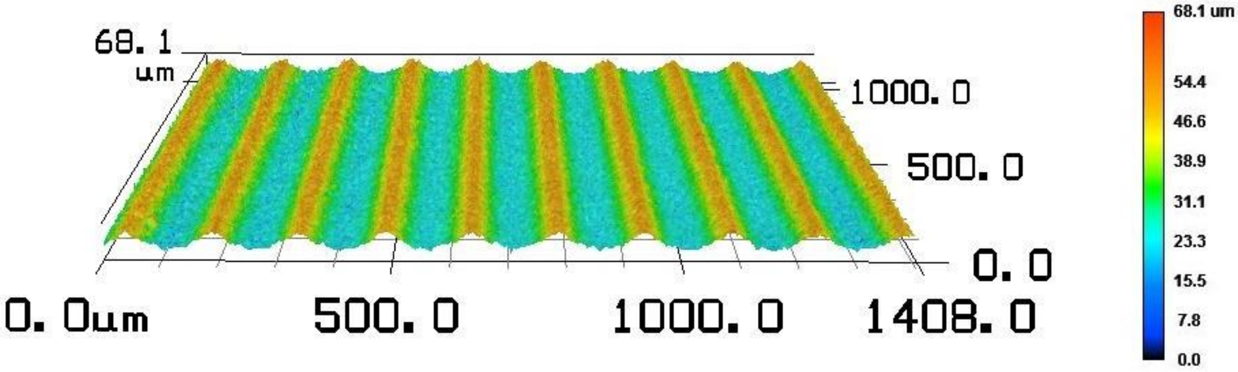

**Figure 21. Laser Confocal Image of Wire EDM Result, $R_{step}$ = 49.6 µm, $R_{SM}$ = 149.8 µm**

Roughness parameters were obtained from each scan and averaged for each profile. The roughness parameters of interest, set forth in Table 3 below, were determined based on information found in literature and through assessment of the profile described by equation 6. Some, if not all, of these parameters were expected to correlate with the variables in equation 6. In particular, the amplitude parameters were expected to correlate with the height *h*, and the spatial parameters would correlate with the pitch $\lambda$. The remaining parameters were hoped to correlate with the roughness slope, or cosine power *p*. These parameters have all been noted in literature and were evaluated to determine their relevance. Results from the surface scans can be found in Table 8 in the Results section.

**Table 3. Roughness Parameters**

| **Amplitude Parameters** | **Spatial Parameters** | **Shape Parameters** |
|---|---|---|
| Average Roughness, $R_a$ | Peak Density, $R_{ds}$ | RMS Tilt, $R_{\Delta q}$ |
| RMS Roughness, $R_q$ | Texture Direction, $R_{td}$ | Skew, $R_{sk}$ |
| Ten Point Height, $R_z$ | Mean Peak Spacing, $R_{SM}$ | Kurtosis, $R_{ku}$ |

The profile equations were re-fit to the two-dimensional surface data in order to compare the measured roughness parameters with the designed pitch and height variables, and to observe any change in the cosine power. For this curve-fitting exercise, two variables were added to the equation to properly align the curve-fit with the data; the phase shift $\varphi$ and vertical shift $E$. The profile equation used in curve-fitting is:

$$f(x) = h\cos^p\left(\frac{\pi}{\lambda}x + \varphi\right) + E$$

In Excel, the height and pitch values were input as the corresponding surface's design parameters. Each of the five variables was adjusted so the curve-fit profile was aligned with the surface data. Excel's solver tool was then used to minimize the least sum of squares. Figure 22 shows a sample of the result from curve-fitting the surface that was designed to have a roughness pitch of 150 μm and height of 50 μm. The measured pitch and height values are discussed below.

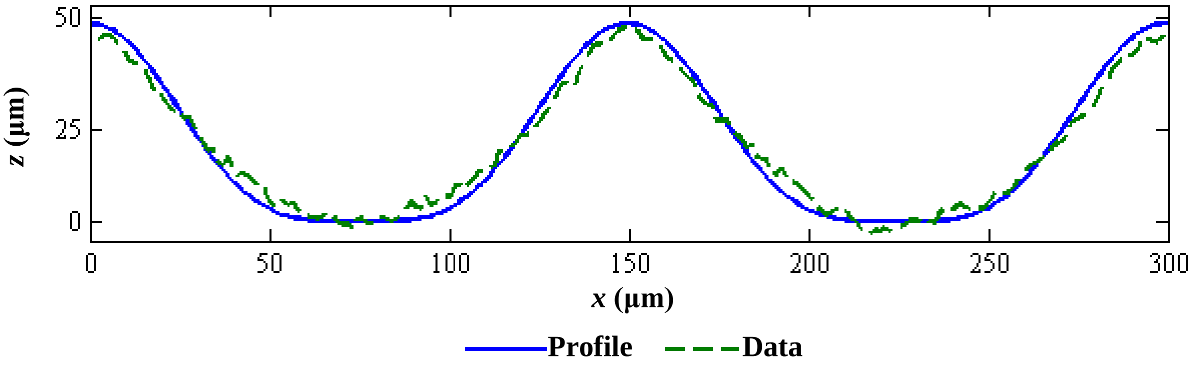

**Figure 22. Curve-fit and Profile Data of Surface Designed for *h* = 50 μm, *λ* = 150 μm**

The results of this curve-fitting exercise and the study of roughness parameters showed that the power values found for the curve-fits of three of the five surfaces differed from the designed values. The "average step height," noted as $R_{step}$, obtained from the laser confocal microscope provided an ideal fit to each surface and compared well with the designed height values. In addition, the mean spacing of peaks, $R_{SM}$, not only provided an excellent fit to the pitch of the surface data, but was also within 0.8 µm of the designed pitch for every profile. Figure 23 illustrates the relation between several amplitude parameters obtained from the five surfaces as compared to the designed roughness height. A perfect fit between designed and measured values would have a slope of 1. Plotting the $R_{SM}$ values versus the designed pitch, for example, yields a slope of 1.00.

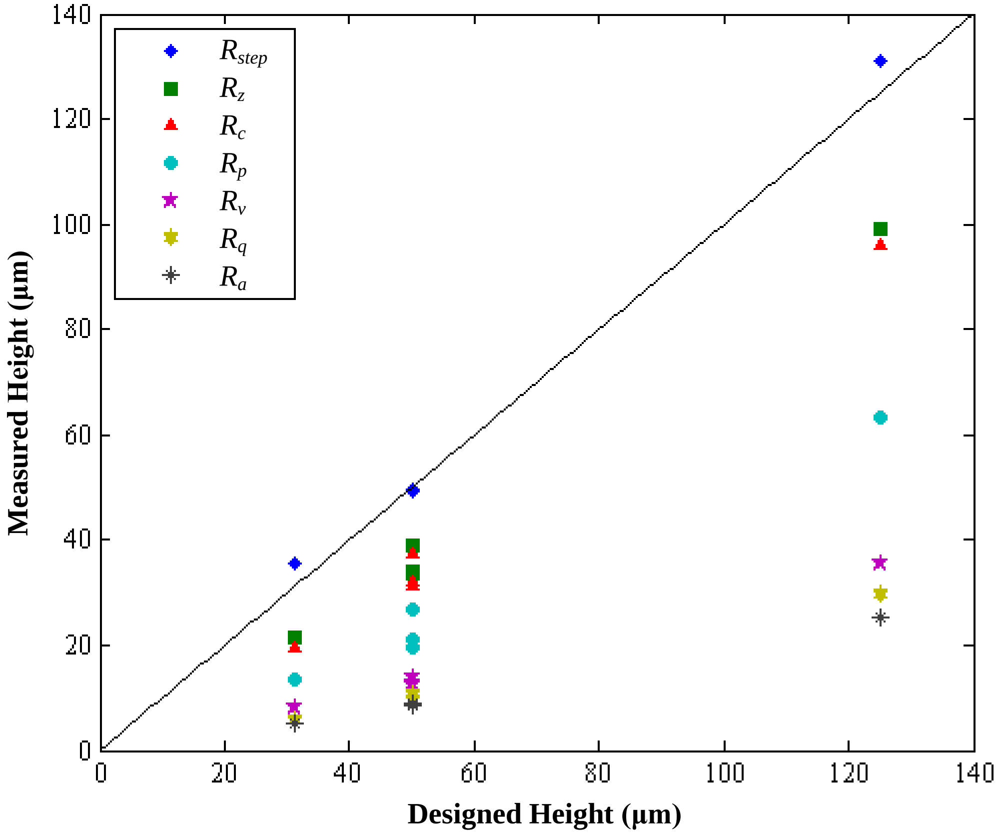

**Figure 23. Measured Amplitude Parameters vs. Designed Height**

It was expected that conventional average roughness parameters such as $R_a$ and $R_q$ would not account for the peaks, but is interesting to note that the maximum height $R_z$ and average height $R_c$ obtained from the microscope did not quite meet the design parameters. This initially seemed to indicate a manufacturing flaw. However, the "average step" parameter, unique to the laser confocal microscope, provides an excellent fit, with a slope of 1.03 when plotted against the designed height. It is not currently clear how this value is calculated within the microscope's software.

No conventional parameter has been correlated to the designed or measured power values with any degree of success. However, a weak correlation was observed with one of the shape parameters identified in Table 3. A plot of these three measured shape parameters versus the designed power can be seen in Figure 13.

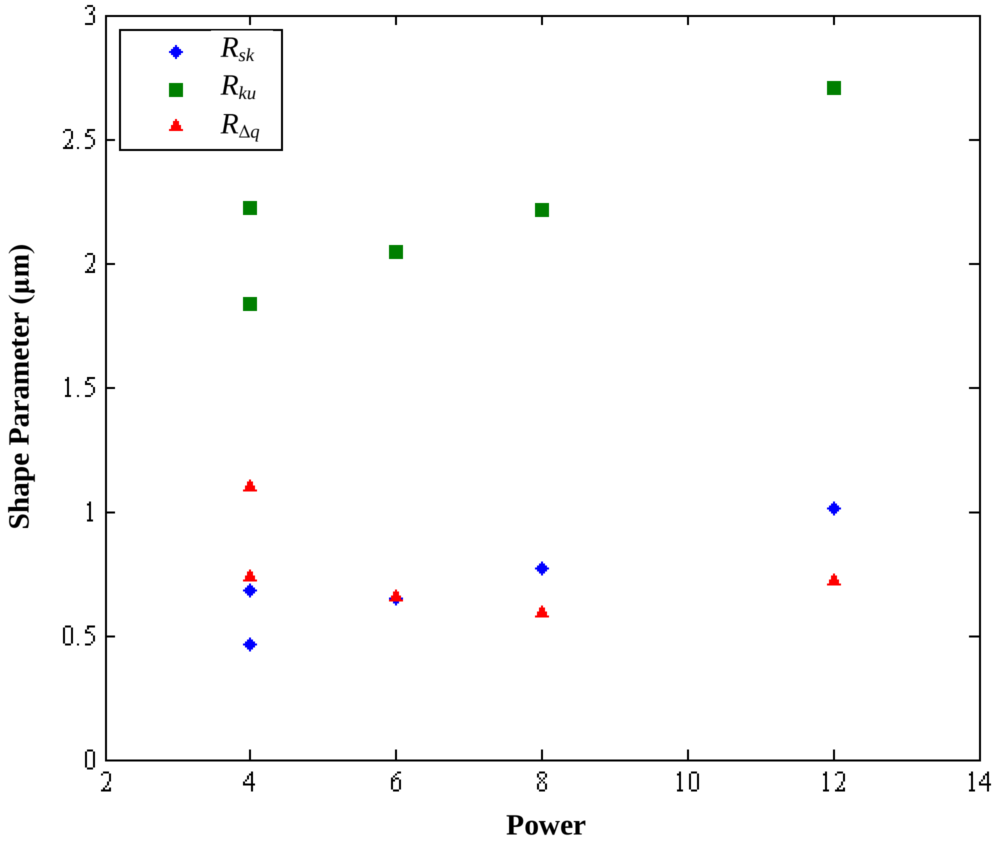

**Figure 24. Shape Parameters vs. Power**

Both skew ($R_{sk}$) and Kurtosis ($R_{ku}$) are functions of the RMS roughness, $R_q$. A Kurtosis value of 3 or a Skew value of 0 would indicate a perfectly random or Gaussian surface, which is not the case in this work. The fact that the skew parameter is small and positive for all surfaces is not surprising, as it indicates a predominance of peaks on a surface, as opposed to valleys, which is true for these surfaces, by design. A kurtosis value greater than 3 indicates a very "spiky" surface characterized by large, sharp peaks and valleys, while values less than 3 indicate many small, rounded peaks and valleys. RMS slope ($R_{\Delta q}$) is the average of slopes at all points, but does not correlate with any variable for these surfaces. The power value still requires some investigation in order to find a way to predict or estimate it for different structured surfaces, knowing that as pitch increases, the power increases non-linearly.

For experimental and theoretical calculations, the roughness profile geometries that were used were the average step height $R_{step}$ and mean spacing of peaks $R_{SM}$, detailed in Table 8 of the Results section. The power values were obtained through curve-fitting and visually verifying agreement between the curve-fit and surface data.

## 5.3 Channel Assembly

An experimental test set was designed using SolidWorks and machined in the Brinkman Lab. Figure 25 shows the geometry of the roughness test pieces. The surface labeled “rough face” possesses the structured roughness detailed previously. Thermocouple holes were drilled to a quarter of the channel depth for concurrent heat transfer testing.

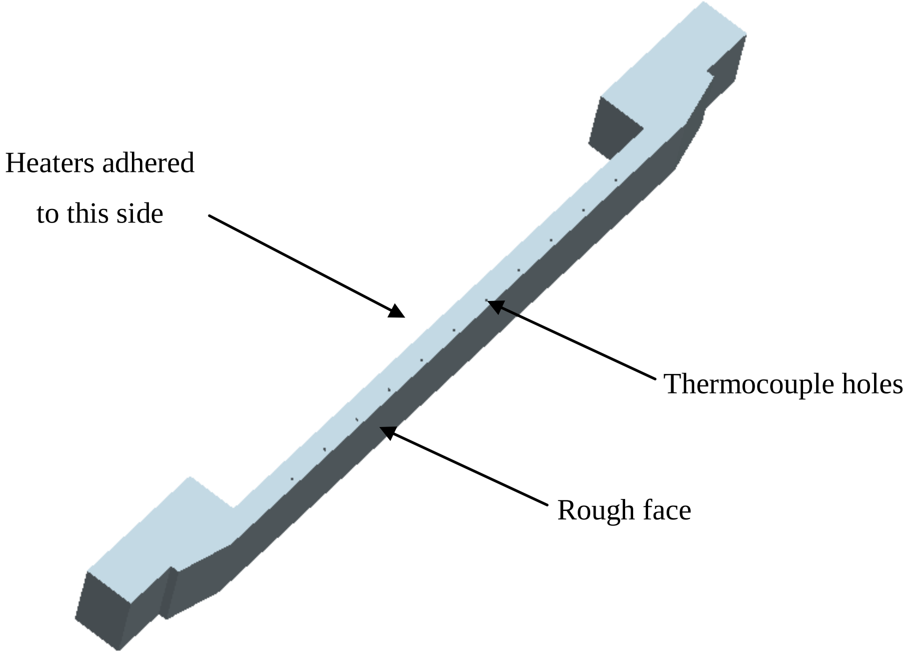

**Figure 25. Solid Model of Roughness Test Piece**

Each end of the test piece was designed to have an inclined face and a small step. This step is where custom-made precision gage blocks were fit to align the roughness peaks and set the channel separation. The gage block design is shown in Figure 26. The hole through the gage block allowed for a smooth transition from circular tubing to the rectangular channel, thereby alleviating cavitation issues identified in earlier versions of the test set.

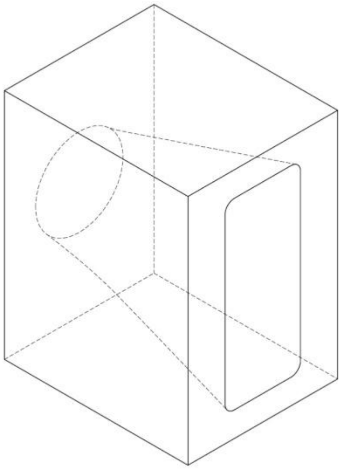

**Figure 26. Solid Model of Gauge Block**

Channel height was fixed at 12.70 mm and the length was 152.4 mm, while the width or separation varied as detailed in Table 2. Both the test pieces and gage blocks were made of stainless steel by wire EDM, and their mating surfaces were precision ground and finished.

A matching pair of test pieces was assembled with a matching pair of gauge blocks to form a rectangular channel of constant cross-section, as seen in Figure 27. Rectangular cartridge heaters, shown in orange, were designed to fit into the back of the roughness test plates, while a backing plate provided both insulation (in the heat transfer test set) and structure to prevent deflection during testing. In the heat transfer test set, the backing plates were made from an insulating material, whereas for this test set they were of aluminum.

Channel separation was set by an identical pair of gauge blocks, which were interchangeable to allow testing of an array of channel sizes. An added benefit of having the channels separately assembled was for inspection of roughness alignment outside of the test set assembly and to ensure the channel was parallel along its entire length. The CAD model of the full test set assembly, including the microchannel assembly, is shown in Figure 28.

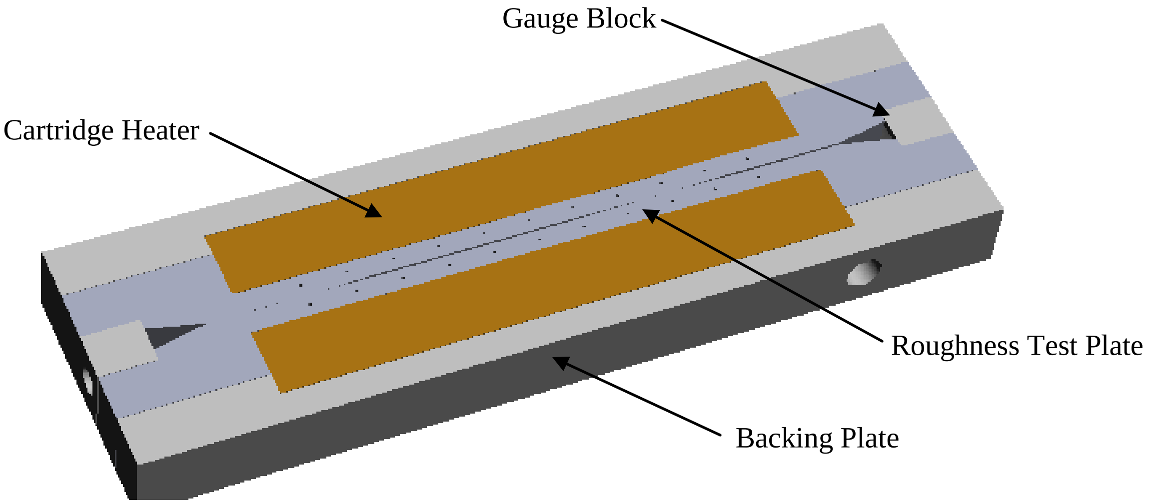

**Figure 27. Solid Model of Microchannel Assembly**

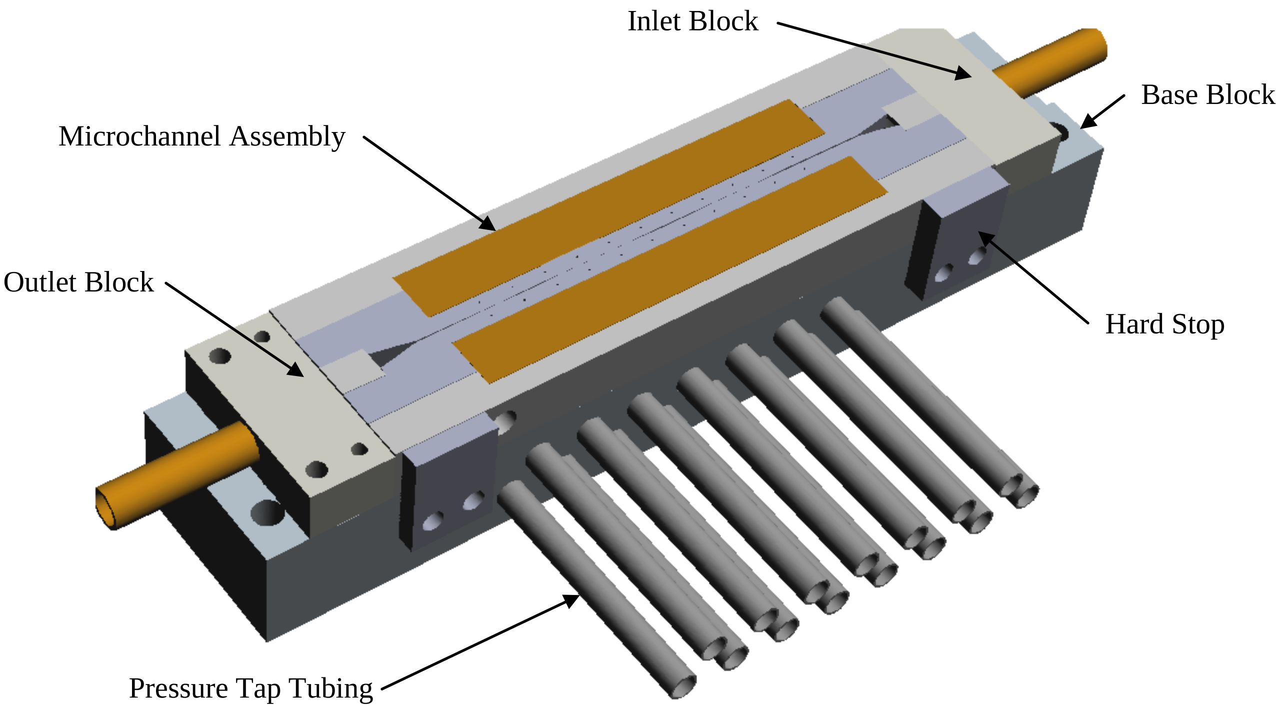

**Figure 28. Solid Model of Test Set Assembly (rear view)**

The test fixture, shown in Figure 28, consists of the base block and the inlet and outlet blocks. The base block was drilled for 15 pressure tap holes and fit with FEP pressure tap tubing, which was abraded, cleaned, and epoxied into the base with a structural adhesive. On the open ends of the tubing shown, differential pressure transducers were pressed in and epoxied in place. Pipe fittings, shown in orange, were assembled into the inlet and outlet blocks to mate with tubing leading from the pump and to the reservoir. The outlet block was aligned on the base by a pair of dowel pins, and then bolted into tapped holes in the base. The inner (channel side) hole of the outlet block aligned with the circular hole in the gauge block, and thus the entire channel was centered over the line of pressure tap holes in the base. This ensured that the entire channel assembly was repeatedly aligned with the pressure tap holes in each test. The inlet block slid along a slot in the base, and was clamped to the base by a toe clamp from above, while a custom clamping devise was used to provide axial compression to seal the inlet and outlet. A separate clamping fixture was also used to compress the channel horizontally (perpendicular to the flow direction) against the hard stops. As a final assembly step, a solid aluminum lid was clamped down across the top of the channel with a series of three large toe clamps.

All interfaces between the microchannel assembly and test fixture were sealed with a 0.32 inch thick adhesive-backed Silicon gasket. This gasket was replaced periodically as over-compressing or frequently clamping and unclamping would damage the gasket and increase the risk for leaks.

## 5.4 Test Loop

Liquid flow testing was performed using degassed distilled water in a closed test loop, shown in Figure 29. A collapsible reservoir contained approximately 3 gallons of degassed water, and would collapse as water was drained from the system to prevent a large liquid-to-air interface from forming within the container. A bank of flow meters measured separate ranges of flow rate, with sufficient overlap between them, and were activated by opening valves located upstream of each. An array of 15 pressure transducers, denoted by the letter **P** in Figure 29, spaced 6.53 mm apart, measured gage pressure along the channel length. Thermocouples, labeled **T**, situated at the inlet and outlet measured bulk fluid temperature for interpolation of fluid properties. The micropump was controlled through a custom LabVIEW program which also recorded data from all sensors. Data processing was achieved using MS Excel, while the theoretical friction factors based on the wall function method were computed in MATLAB.

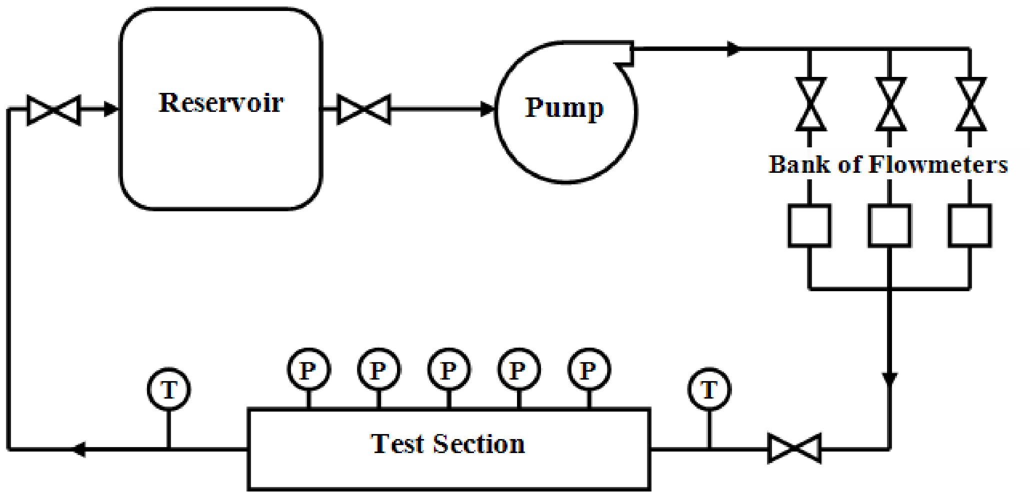

Figure 29. Schematic of Experimental Test Loop

Friction factors were calculated using equation 19 for laminar flow in smooth rectangular ducts, and equation 17 for the constricted and un-constricted experimental friction factors. These were compared with friction factors obtained from the wall function method, as set forth in the Theoretical Approach section. Extensive analysis and comparison of surface geometries was made in an attempt to evaluate the effect of pitch-to-height ratio of structured roughness, as well as the relative importance of existing roughness parameters on fluid flow.

## 5.5 Calibration and Experimental Uncertainty

To assess the experimental uncertainty in the microchannel test setup, multiple tests were run at constant flow rates corresponding to the laminar and turbulent flow regimes. Each test ran for a length of time during which a custom LabView program was used to record data from each sensor to ensure steady state had been achieved and to provide an extensive set of data for analysis. The two dimensionless parameters examined were the Reynolds number and friction factor, as defined previously. These parameters are dependent on channel geometry, fluid properties, and flow conditions. The error inherent in each sensor and measurement device was combined with the error associated with repeatability to provide a final percent error for the friction factor and Reynolds number.

The baseline experiment used degassed distilled water flowing through a hydraulically smooth rectangular channel. The microchannel was constructed as described in the Channel

Assembly section, and installed in the test loop described above. All sensors used in this test set were connected to a single DAQ system controlled in LabView. These devices were also mapped to and read in Measurement and Automation Explorer (MAX) for comparison with the LabView output. The following calibration procedures were repeated biweekly to assess the drift in measurements over time, and to maintain known uncertainty.

### 5.5.1 Pressure Transducer Calibration

The Omega DPI 610 pressure calibrator was used to apply pressure to each sensor. Although the voltmeter on the Omega calibrator can be used to read the pressure sensor's output, it was more convenient and more consistent with actual testing to read voltage through the DAQ. Each channel to which the differential sensors were connected was mapped to individually in the test panel in MAX.

The voltage input limits were varied depending on the operating range of the transducers. To begin at 0 kPa, all valves on the calibrator were opened. MAX displayed an average voltage for the immediate pressure, and both pressure and voltage values were recorded in an Excel file. With all valves closed, pressure was applied in increments of about 10 kPa, up to just under the limit of the transducer (e.g., 190 kPa for the 200 kPa sensors), and each successive pair of pressure-voltage values were recorded. The slope and intercept of the data was calculated directly using the slope and intercept functions in Excel. The slopes and intercepts obtained were compared with previous calibration values for each of the 15 pressure transducers by calculating the percent difference or drift. The slope for each sensor was then entered into the custom LabView program, but because of a zeroing function added in the code, the intercept of the data was not needed. The drift between sensor calibrations was less than 0.2% for all sensors over the course of testing, with the greatest drift observed for transducers in the entrance region.

### 5.5.2 Flowmeter Calibration

Each of the three Omega flow meters covers a different range of flow rates:

FLR-7: 13 – 100 mL/min
FLR-10: 60 – 1000 mL/min
FLR-12: 500 – 5000 mL/min

In the experimental set-up, there was an outlet downstream of the bank of flow meters, before the test section, from which water was collected. A precision scale was used to measure the mass of water collected, once the scale was calibrated to the mass of the beaker used to collect the water. Rather than using MAX, a simplified LabView code, similar to the test code, was used to run the pump at a constant RPM, record the time, and to record the voltage output from the flow sensor. Data was recorded in the Excel calibration file and analyzed similar to the pressure data. Dividing the mass of water by the time the pump was run provided the mass flow rate. The correlation between the flow rates and the voltage output from each flowmeter was then implemented in the custom LabView code.

### 5.5.3 Thermocouple Calibration

A two-point calibration was sufficient for this experiment, as the thermocouples were used for interpolation of bulk fluid properties. The two points require an ice bath (0°C) and boiling water (100°C). Prior to performing this calibration, the thermocouples and containers were cleaned thoroughly with distilled water.

For the ice bath, the container was filled with shaved or crushed clear ice made from distilled water. Distilled water was also added to create an ice bath with enough water to provide good thermal contact with the thermometers, but not so much as to cause the ice to float. A thermometer was kept in the container and used to stir the ice bath every few minutes to prevent cavities or air pockets from forming as ice melted. Temperature was allowed to stabilize for about half an hour, while stirring the ice, draining off excess water, and adding ice as needed. The thermocouples were inserted into the bath such that they were submerged to the same depth, with at least a few inches of ice between them and the bottom and sides of the container. It was also ensured that the thermocouples were at the same depth and not in contact with one another. Temperature values were read from the uncalibrated thermocouples in LabView over time, and recorded in the Excel file.

The procedure was repeated for boiling water, using a hot plate to bring distilled water to a boil and inserting the thermocouples to the same depth requirements. The thermocouples were allowed to reach a steady temperature, which was recorded from Lab View into Excel. A linear correlation for temperature was implemented into the LabView code as with the pressure transducers.

### 5.5.4 Bias and Precision Error

There are two classifications of error said to affect system measurements; bias and precision. Bias, or systematic error, occurs repeatedly with each measurement. It includes calibration, loading, and resolution errors and is typically reported by the sensor’s manufacturer as a percentage. Precision, or random error, is the irregular fluctuation or variance in data, such as white noise, which cannot be filtered. These errors were assessed for each device used in these experiments.

Precision and bias errors may be evaluated analytically by assuming that uncertainties behave like standard deviations. A specific physical quantity, $y$ can be considered to be a function of the independent measurements made to obtain its value:

$$y = f\left(x_1, x_2, ...x_n\right)$$

in which $x_i$ represents any individual measurement, where $i$ ranges from 1 to $n$. Total uncertainty combines both bias and precision errors through the following formulation:

$$U_y = \sqrt{B_y^2 + P_y^2}$$

where $B_y$ represents bias error and $P_y$ represents precision error associated with the measured quantity, $y$. Bias error is fairly straightforward to estimate, as it is dependent on the apparent accuracy of any given sensor, and may be calculated as:

$$\begin{aligned} B_y^2 &= \sum_{i=1}^{n}\left(\frac{\partial y}{\partial x_i} B_{x_i}\right)^2 \\ &= \left(\frac{\partial y}{\partial x_1} B_{x_1}\right)^2 + \left(\frac{\partial y}{\partial x_2} B_{x_2}\right)^2 + ... + \left(\frac{\partial y}{\partial x_n} B_{x_n}\right)^2 \end{aligned}$$

In the above equation, $B_{x_i}$ represents the bias, reported as a percent error by the manufacturer, associated for the $i^{\text{th}}$ instrument used in taking the necessary measurements to obtain $x_i$. The partial derivative of the physical quantity with respect to a given measurement, $\frac{\partial y}{\partial x_i}$, represents the weight which that measurement carries in calculating the physical quantity. This value may be taken to be the absolute value of the exponent on that variable in the relation $y = f\left(x_1, x_2, ...x_n\right)$. A brief study was carried out to assess the difference in calculating the partial derivatives for each variable, as opposed to taking the partial derivative to be the power of the variable, and it was found that the percent error is marginally larger when using the power, providing a more conservative estimate for the error.

Precision error is not expressly given for each device since it is typically related to unpredictable fluctuations in the data, and is sometimes classified as "human error." It may be treated in the same manner as bias error by estimating a standard deviation based on knowledge of the instruments. Thereby, with a 95% confidence interval, precision of a given measurement may be approximated as:

$$P_y = 1.96\sigma_y$$

where $\sigma_y$ is the estimated standard deviation for the calculated result $y$ (the value 1.96 correlates to a 95% confidence interval). When multiple data points may be taken, as was the case of this experiment, the standard deviation of any calculated result is calculated in the same manner as the bias error:

$$\begin{aligned}\sigma_y^2 &= \sum_{i=1}^{n}\left(\frac{\partial y}{\partial x_i}\sigma_{x_i}\right)^2 \\ &= \left(\frac{\partial y}{\partial x_1}\sigma_{x_1}\right)^2 + \left(\frac{\partial y}{\partial x_2}\sigma_{x_2}\right)^2 + \ldots + \left(\frac{\partial y}{\partial x_n}\sigma_{x_n}\right)^2\end{aligned}$$

where $\sigma_{x_i}$ is the standard deviation of measurements taken using the $i^{\text{th}}$ instrument. To obtain this standard deviation, a series of steady data was recorded.

This approach was applied to calculations for the Reynolds number (equation 21) and Darcy friction factor (equation 17) by breaking each equation down into its simplest measurable components. Taking the equation for Reynolds number, for example, yields the following:

$$\mathrm{Re} = \frac{\rho u D}{\mu} = \frac{\rho Q}{\mu A}\cdot\frac{4A}{P} = \frac{2\rho Q}{\mu(a+b)}$$

Each channel dimension, height $a$ and width $b$, was measured with a different instrument, and so the bias and precision errors are not necessarily the same. All variables carry a power of one, such that $\frac{\partial \mathrm{Re}}{\partial x_i} = 1$ for all $x_i$. The bias and precision errors for Reynolds number are as follows:

$$\begin{aligned}B_{\mathrm{Re}}^2 &= \left(\frac{\partial \mathrm{Re}}{\partial Q}B_Q\right)^2 + \left(\frac{\partial \mathrm{Re}}{\partial \rho}B_\rho\right)^2 + \left(\frac{\partial \mathrm{Re}}{\partial \mu}B_\mu\right)^2 + \left(\frac{\partial \mathrm{Re}}{\partial a}B_a\right)^2 + \left(\frac{\partial \mathrm{Re}}{\partial b}B_b\right)^2 \\ &= B_Q^2 + B_\rho^2 + B_\mu^2 + B_a^2 + B_b^2\end{aligned}$$

$$P_{\mathrm{Re}}^2 = 1.96^2\left[\left(\frac{\partial \mathrm{Re}}{\partial Q}\sigma_Q\right)^2 + \left(\frac{\partial \mathrm{Re}}{\partial \rho}\sigma_\rho\right)^2 + \left(\frac{\partial \mathrm{Re}}{\partial \mu}\sigma_\mu\right)^2 + \left(\frac{\partial \mathrm{Re}}{\partial a}\sigma_a\right)^2 + \left(\frac{\partial \mathrm{Re}}{\partial b}\sigma_b\right)^2\right]$$

$$= 3.84\left(\sigma_Q^2 + \sigma_\rho^2 + \sigma_\mu^2 + \sigma_a^2 + \sigma_b^2\right)$$

The equation for friction factor, broken down to its measurable components, is:

$$f = \frac{\Delta P}{\Delta x}\cdot\frac{D_h}{2\rho u^2} = \frac{\Delta P}{\Delta x}\cdot\frac{4A}{P}\cdot\frac{A^2}{2\rho Q^2} = \frac{\Delta P}{\Delta x}\frac{2A^3}{\rho Q^2 P} = \frac{\Delta P}{\Delta x}\frac{2a^3b^3}{\rho Q^2(a+b)}$$

In this equation, the flow rate and channel dimensions carry a weight of 2 and 3, respectively. The uncertainties are as follows:

$$B_f^2 = \left(\frac{\partial f}{\partial P}B_P\right)^2 + \left(\frac{\partial f}{\partial Q}B_Q\right)^2 + \left(\frac{\partial f}{\partial \rho}B_\rho\right)^2 + \left(\frac{\partial f}{\partial x}B_x\right)^2 + \left(\frac{\partial f}{\partial a}B_a\right)^2 + \left(\frac{\partial f}{\partial b}B_b\right)^2$$

$$= B_P^2 + 4B_Q^2 + B_\rho^2 + B_x^2 + 9B_a^2 + 9B_b^2$$

$$P_f^2 = 1.96^2\left[\left(\frac{\partial f}{\partial P}\sigma_P\right)^2 + \left(\frac{\partial f}{\partial Q}\sigma_Q\right)^2 + \left(\frac{\partial f}{\partial \rho}\sigma_\rho\right)^2 + \left(\frac{\partial f}{\partial x}\sigma_x\right)^2 + \left(\frac{\partial f}{\partial a}\sigma_a\right)^2 + \left(\frac{\partial f}{\partial b}\sigma_b\right)^2\right]$$

$$= 3.84\left(\sigma_P^2 + 4\sigma_Q^2 + \sigma_\rho^2 + \sigma_x^2 + 9\sigma_a^2 + 9\sigma_b^2\right)$$

A series of tests were run at constant flow rates, such that the system had reached a steady state, and one hundred data points were collected during each test. One set of tests was run for laminar flow, and another for turbulent flow. For simultaneous validation of the test setup, a hydraulically smooth channel was tested.

Bias and precision errors for each instrument are reported in Table 4. The bias error was either reported by the manufacturer or taken as an acceptable estimate from Ideal Flows course notes. In the case of density and viscosity, which are functions of the temperature, a separate error analysis was performed to determine their respective bias errors. Density was interpolated from a set of published data [50], while viscosity was computed using an equation fit to empirical data [51].

**Table 4. Instrument Bias and Precision Error**

| Measurement | Units | Instrument | Parameter | Bias (%) | σ | Precision (%) |
|---|---|---|---|---|---|---|
| Flow Rate | mL/min | Omega FLR1000 Series Flowmeter | $Q$ | 3.000 | 0.636 | 0.588 |
| Pressure | kPa | Omega PX26 Series Pressure Transducer | $P$ | 1.000 | 0.100 | 0.196 |
| Temperature | °C | ±0.1ºC Thermocouples | $\rho$ | 0.0005 | 0.0294 | 0.000 |
| | | | $\mu$ | 0.0442 | 0.0294 | 0.009 |
| Channel Height, Length | mm | Calipers | $a$, $L$ | 0.200 | 0.020 | 0.039 |
| Channel Separation, Roughness | µm | Laser Confocal | $b$, $h$, $\lambda$ | 0.001 | 0.000 | 0.000 |
| | | | | 0.001 | 0.000 | 0.000 |

The standard deviations shown above were calculated from the laminar test data or taken as one tenth of the bias error. For a conservative analysis, the higher error was used in calculating precision for each measurement. In addition to calculating the worst-case error, the experimental standard deviations in flow, pressure, and temperature were examined for laminar and turbulent flows. These values are cataloged in Table 5.

**Table 5. Laminar and Turbulent Precision Error**

| Measurement | Parameter | | σ | Precision (%) |
|---|---|---|---|---|
| Flow Rate | $Q$ | Laminar | 0.6357 | 1.246 |
| | | Turbulent | 0.9163 | 1.796 |
| Pressure | $P$ | Laminar | 0.0057 | 0.011 |
| | | Turbulent | 0.0127 | 0.025 |
| Temperature | $\rho$, $\mu$ | Laminar | 0.0294 | 0.058 |
| | | Turbulent | 0.0000 | 0.000 |

The percent error in Reynolds number and friction factor were computed for both laminar and turbulent flow, and can be found in Table 6. In addition to the method defined here, uncertainty was calculated for each parameter without decomposing the equations to their basic measurable components, in order to compare the outcomes of different uncertainty analysis methods. It was found that other methods resulted in lower values for experimental uncertainty. The values in Table 6 show that the bias error is the same for each instrument. Precision was evaluated first taking the standard deviation to be one tenth of the bias error, then using the standard deviations calculated from laminar and turbulent flow data.

**Table 6. Parameter Error**

| **Parameter** | **Bias** | **Precision** | **Total Uncertainty** |
|---|---|---|---|
| | **(%)** | **(%)** | **(%)** |
| $Re$ | 3.007 | 0.589 | 3.064 |
| $Re_{lam}$ | 3.007 | 1.249 | 3.256 |
| $Re_{turb}$ | 3.007 | 1.796 | 3.503 |
| $f$ | 6.116 | 1.198 | 6.232 |
| $f_{lam}$ | 6.116 | 2.495 | 6.605 |
| $f_{turb}$ | 6.116 | 3.593 | 7.093 |

Because the bias error for the laser confocal microscope is approximately zero, and the standard deviation for all roughness measurements was small, there is effectively zero difference between uncertainty calculated with and without surface roughness. As laminar flow is the aim of this work, the errors of interest are; $Re_{lam}$ = 3.3% and $f_{lam}$ = 6.6%.

In order to minimize error during experimentation, sensor calibrations were checked periodically and repeated as needed. Also, as the introduction of air into the system was prone to occur through regular use of the setup, the reservoir was periodically drained and replenished with a new batch of degassed water. This was deemed necessary due to a comparative study using plain distilled and degassed distilled water in the test setup. Plain distilled water resulted in a somewhat greater standard deviation in steady state measurements over time.

# 6 Results and Discussion

In the following sections, the experimental data for smooth and rough channels is discussed in detail and compared with the smooth channel correlation, the wall function method, and the constricted flow model. The size of data points in the plots of friction factor versus Reynolds number is approximately equal to half the experimental uncertainty of the friction factors. Percent errors between experimental and theoretical friction factors, as described in the text, were calculated as:

$$\%Error = \frac{f_{\exp} - f_{theory}}{f_{theory}} \cdot 100$$

## 6.1 Validation of Test Set with Hydraulically Smooth Channels

Preliminary experiments with smooth channels were performed in order to verify that the experimental test setup complied with the smooth channel correlation. The average roughness values for the smooth test pieces are $R_a$ = 0.2 µm and $R_q$ = 0.3 µm. Close agreement between these roughness values indicates that there are no significant gouges or protrusions on the surfaces. The constricted flow parameter was calculated for comparison, and was found to be 1.2 µm. It should be noted that these smooth test pieces were not in fact polished, but tested as obtained from the manufacturer. The low roughness values and the experimental data both indicate that the wire EDM method of manufacture provides a very good surface finish on parts, particularly in terms of hydraulic performance.

Channel separations were set with the 100, 450, 600, and 800 µm gauge blocks. The channel separations were measured both before and after testing to verify that the separation did not vary significantly during tests. Each channel was scanned at 7 points evenly spaced along the length, at 1 cm spacings, and these points were averaged to obtain a nominal or root channel separation. Table 7summarizes the measured smooth channel geometry that coincides with the data shown in Figure 30.

The aspect ratio is the channel separation divided by its height, *b*/*a*, and hydraulic diameter is calculated as in equation 18. Relative roughness was evaluated using the constricted flow parameter as the roughness size, because it was found to be the largest of the amplitude parameters obtained, and to illustrate that, even with the largest roughness value obtained, the relative roughness is less than 1% for all channel separations. Use of either the average or RMS roughness resulted in relative roughness values ranging from 0 to 0.2%.

**Table 7. Measured Channel Geometry – Smooth Surfaces**

| Separation | Aspect Ratio | Hydraulic Diameter | Relative Roughness |
|---|---|---|---|
| ***b*** | ***α*** | **$D_h$** | **$e/D_h$** |
| **µm** | **---** | **µm** | **---** |
| 101.8 | 0.01 | 202 | 0.6% |
| 377.5 | 0.03 | 733 | 0.2% |
| 548.4 | 0.04 | 1051 | 0.1% |
| 751.0 | 0.06 | 1418 | 0.1% |

In fluid flow tests, the flow rate was varied such that the range of Reynolds numbers spanned from approximately 50 to 4000, although the entire range was not possible for every channel separation. Reynolds number was calculated using the hydraulic diameter, from the root channel separations listed in Table 7. Friction factors were calculated using equation 17, and Reynolds numbers were calculated using equation 21. Theoretical turbulent friction factors were calculated using the Swamee–Jain equation:

$$f = \frac{0.25}{\left[\log\left(\frac{e}{3.7D_h} + \frac{5.74}{\mathrm{Re}^{0.9}}\right)\right]^2}$$

where $e/D_h$ is the relative roughness and $Re$ is the Reynolds number.

The laminar theory line, shown in black in Figure 30, was calculated using equation 19, which is intended for use with hydraulically smooth rectangular channels. Due to the small change in aspect ratio across test cases, there was a difference in friction factor of about 6% when switching between the smallest and largest channel separations. The laminar theory line shown in Figure 30was calculated using the largest aspect ratio; $\alpha = 0.6$.

In all cases, the experimental data was within 10% of conventional laminar theory for smooth rectangular channels. In the case of the smallest channel separation, 102 µm, the immense pressure consistently led to leakages above a Reynolds number of 400 across multiple tests. The ability to observe the behavior of friction factors as the leak occurred in this validation test allowed for early detection of leaks in rough channel experiments, particularly for the smaller channel separations.

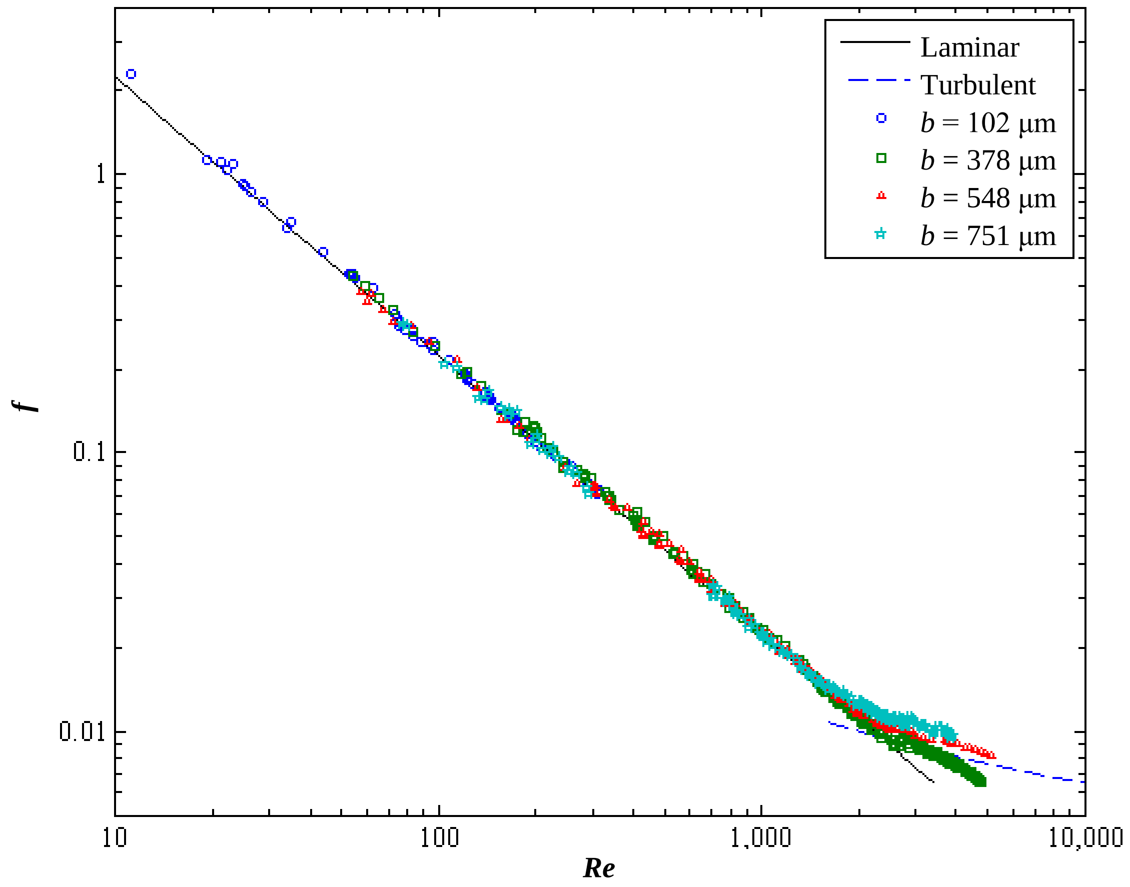

**Figure 30. Smooth Channel Friction Factor vs. Reynolds Number,**
***b* = 102, 378, 548, and 751 µm**

Figure 31 shows a plot of laminar experimental friction factors versus theoretical friction factors. The purpose of this plot is to illustrate the linearity of the data when compared with theory, and to show that the data is well within 10% of laminar theory, as the lines in black represent a slope of 1 and ±10% of that line.

This data indicates that the experimental test set is within the anticipated uncertainty of 6.6% for the friction factor in the laminar regime. The greatest deviation from the smooth channel correlation occurred for the smallest channel separation, which is not entirely unexpected, as the literature indicated friction factors increase as channel size decreases.

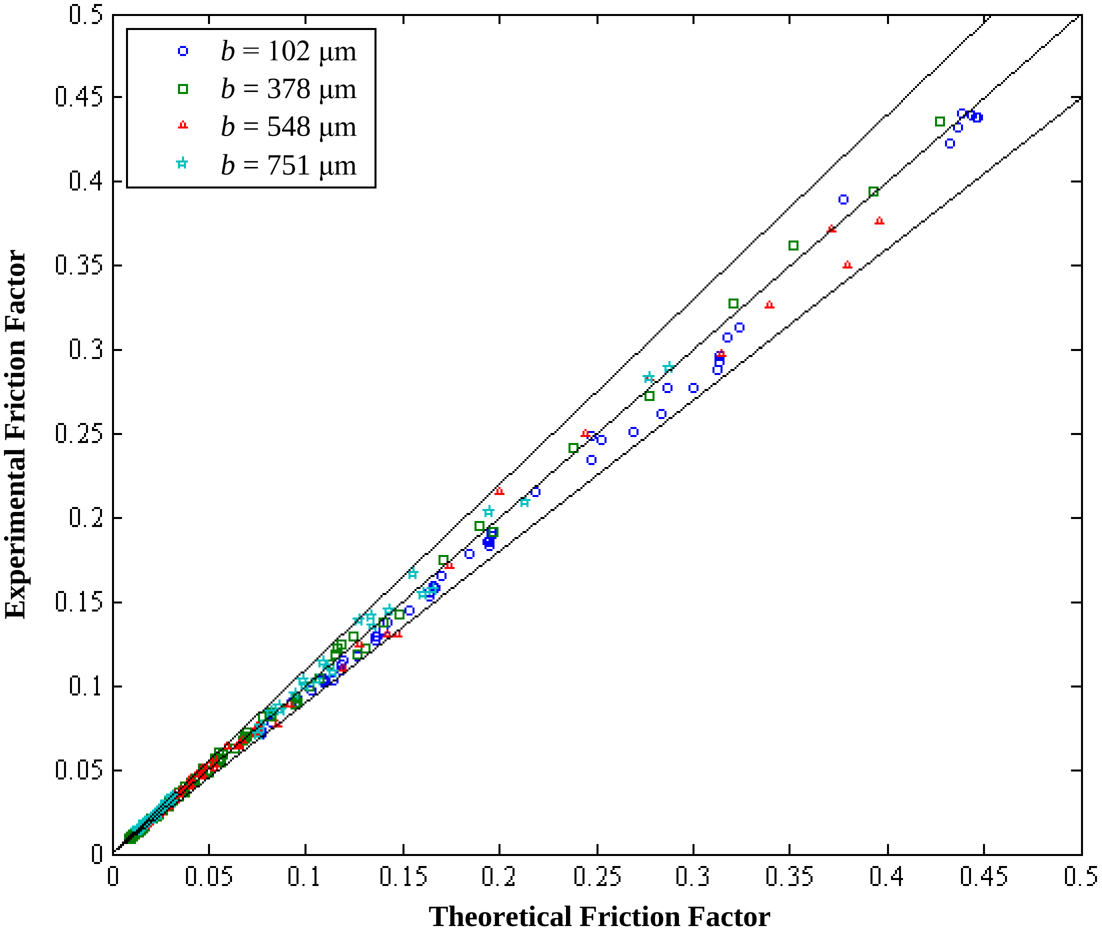

**Figure 31. Smooth Channel Experimental vs. Theoretical Friction Factors**

***b*** **= 102, 378, 548, and 751 µm**

## 6.2 Structured Roughness Results

Five sinusoidal roughness profiles were designed for experimental validation of the wall function method developed herein. These surfaces were manufactured via wire EDM and were measured extensively under a laser confocal microscope. The results of those surface measurements, and the ensuing curve-fitting exercises, are summarized in Table 8 below. The values chosen to represent the roughness pitch and height are the mean spacing of peaks $R_{SM}$ and the average step height, respectively. In addition to the profile geometry, Table 8 includes the constricted parameter, RMS roughness, and average roughness for each profile. In the following sections, these surfaces are typically referred to by their respective pitch-to-height ratios, with the exception of the tallest and shortest profiles which are alternately referred to as “tall” and “short,” respectively.

**Table 8. Test Matrix Summary: Roughness Geometry - Measured**

| Geometry | | | Average Roughness | | |
|---|---|---|---|---|---|
| Pitch | Height | Aspect Ratio | Constricted Parameter | RMS | Arithmetic Mean |
| *λ* | *h* | *λ/h* | $\varepsilon_{Fp}$ | *Rq* | *Ra* |
| µm | µm | --- | µm | µm | µm |
| 249.5 | 131.0 | 2 | 85.5 | 29.8 | 25.4 |
| 149.8 | 49.6 | 3 | 27.7 | 9.9 | 8.6 |
| 250.2 | 49.4 | 5 | 28.3 | 9.7 | 8.5 |
| 400.4 | 49.6 | 8 | 33.8 | 10.8 | 9.0 |
| 250.6 | 35.6 | 7 | 17.5 | 5.8 | 5.0 |

The five roughness profiles were tested experimentally for four channel separations each, with the exception of the profile of the lowest peak height, for which only three channel separations were tested. Channel separation was measured as described for the smooth channel, but the measurement was taken in the smooth valleys, between roughness peaks, so as to obtain the root separation required for the theoretical assessment. In a number of cases, there was some discrepancy between measurements before and after testing, or bowing of the roughness test pieces would occur. Figure 32 shows a plot of the separation values measured before and after testing the short profile ($h$ = 31.25 µm, $\lambda$ = 250 µm) with the 450 µm gauge blocks.

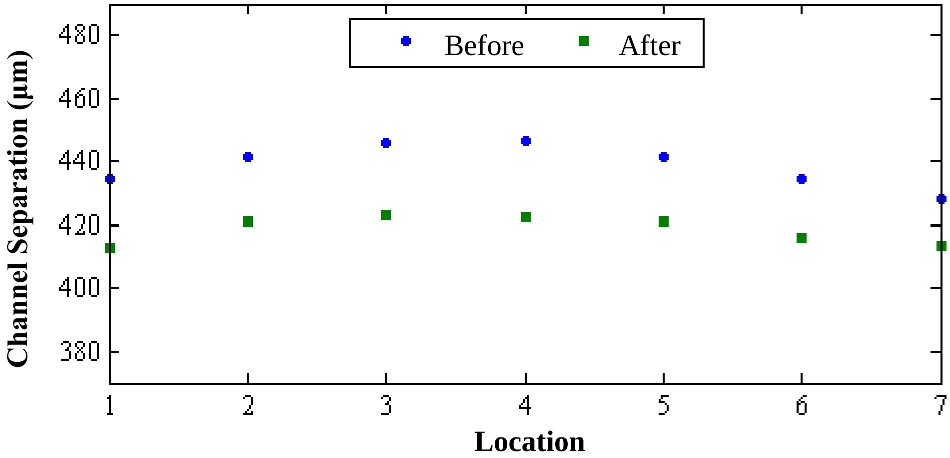

**Figure 32. Deviation in Channel Separation Measured Before and After Flow Testing Using 450 µm Gauge Blocks and $\lambda/h$ = 7 Surface**

The average separation measured before the test represented by Figure 32 was 418.6 µm, and 439.0 µm after. A deviation of about 20 µm is quite significant at this scale, and could have severe effects on much taller roughness profiles. It is also necessary to note that the separation is smallest at the ends and greatest in the middle in this figure, indicating that the channel was bowed. Therefore, the clamping was not even along the channel length, and the flow data should be retaken. In all, a minimum of 5 trials per test case were run in order to assure that the separation and the resulting data were consistent. Although the precision gauge blocks provide similar channel separations between test cases, those separations were not exactly as designed due to differences between roughness profiles. The following table details the measured channel separations for each test condition, as well as the associated relative roughness values. Channel geometry is identified by the pitch-to-height ratio in the left-hand column.

**Table 9. Test Matrix Summary: Channel Geometry - Measured**

| **Profile** | **Channel Dimensions** | | | | | |
|---|---|---|---|---|---|---|
| **Pitch-to-Height Ratio** | **Separation** | **Aspect Ratio** | **Hydraulic Diameter** | **Relative Roughness** | **Relative Roughness** | **Height-Separation Ratio** |
| $\lambda/h$ | $b$ | $\alpha$ | $D_h$ | $h/Dh$ | $\varepsilon_{Fp}/D_h$ | $h/b$ |
| --- | µm | --- | µm | --- | --- | --- |
| 2 | 377.0 | 0.03 | 732 | 18% | 12% | 0.35 |
| | 536.2 | 0.04 | 1029 | 13% | 8% | 0.24 |
| | 754.6 | 0.06 | 1425 | 9% | 6% | 0.17 |
| | 936.9 | 0.07 | 1745 | 8% | 5% | 0.14 |
| 3 | 230.3 | 0.02 | 452 | 11% | 6% | 0.22 |
| | 413.7 | 0.03 | 801 | 6% | 3% | 0.12 |
| | 551.8 | 0.04 | 1058 | 5% | 3% | 0.09 |
| | 751.3 | 0.06 | 1419 | 3% | 2% | 0.07 |
| 5 | 230.5 | 0.02 | 453 | 11% | 6% | 0.21 |
| | 414.1 | 0.03 | 802 | 6% | 4% | 0.12 |
| | 577.2 | 0.05 | 1104 | 4% | 3% | 0.09 |
| | 780.3 | 0.06 | 1470 | 3% | 2% | 0.06 |
| 8 | 257.7 | 0.02 | 505 | 10% | 7% | 0.19 |
| | 444.0 | 0.03 | 858 | 6% | 4% | 0.11 |
| | 593.4 | 0.05 | 1134 | 4% | 3% | 0.08 |
| | 791.0 | 0.06 | 1489 | 3% | 2% | 0.06 |
| 7 | 231.4 | 0.02 | 455 | 8% | 4% | 0.15 |
| | 439.0 | 0.03 | 849 | 4% | 2% | 0.08 |
| | 571.8 | 0.05 | 1094 | 3% | 2% | 0.06 |

To summarize, the overall range of channel separations tested was 230.3 to 936.9 µm, which corresponds to a range of hydraulic diameters of 452 to 1745 µm. Relative roughness ranged from 2% to 12%, using the constricted parameter. The roughness height to channel separation ratio $h/b$ ranged from 0.06 to 0.35, indicating that the roughness projected into the channels to a significant degree in most cases, specifically the smaller channel separations and the tallest roughness height case.

In all tests, the smallest channel separation possible was tested first, in order to obtain the greatest pressure drop and check for leakages. If the largest separation were to have been used first, then leaks might not be discovered until smaller channel separations, at which time the test section would need to be disassembled and re-sealed, increasing the risk for deviations in geometry measurement. Once data were obtained for the smallest channel size, successively larger gauge blocks were used.

It is necessary to note that when switching between flowmeters during testing, a smooth transition did not always occur. For this reason, a thorough overlap was obtained. That is, the low flowmeter was used up to its limit of 100 mL/min to record data, the valves were then switched so that the medium flowmeter was active, flow rate was decreased to the lower limit of the medium flowmeter (60 mL/min), and data was recorded with the medium flowmeter up to its limit of 1000 mL/min. Good agreement was found consistently for the low and medium range flowmeters. The high flowmeter, although calibrated in the same manner as the low and medium flowmeters, would consistently “jump” and report a much higher flow rate than the medium flowmeter, resulting in a discontinuity in the data. For this reason, data obtained with the high flowmeter is not reported or used in the data analysis.

The following plots, numbered 33 through 37, summarize the experimental data based on roughness type. They are shown in order of increasing effect on friction factor; $\lambda/h$ = 7, 8, 5, 3, 2. Reynolds numbers were calculated using equation 21, while experimental friction factors were calculated using the Darcy-Weisbach equation, equation 17. The theoretical laminar friction factor line, shown in black on each plot, was calculated using equation 19 and the smallest aspect ratio recorded for each surface. The maximum decrease in laminar theory friction factors, as aspect ratio increased for any given surface, was 6%, which is less than the experimental error. Theoretical turbulent friction factor lines were calculated using the Swamee-Jain equation, defined previously.

Following this section is a comparison between the experimental data and the wall function method’s prediction for performance, based on the measured channel size and roughness geometries. For the wall function method prediction, the measured geometries and constant fluid properties were input in MATLAB. Flow rate was set to vary by ranging the Reynolds numbers from 5 to 3400, as detailed in the Preliminary Results section. There is also a brief section on the application of the constricted flow model.

The lowest roughness tested had a measured height of 35.6 µm and pitch of 250.6 µm, $\lambda/h = 7$. The relative roughness for this surface ranged from 2% to 4% using the constricted parameter. According to the Moody diagram, which is limited to a relative roughness of 5%, laminar flow is unaffected by surface roughness. Figure 33 below shows the experimental friction factors obtained for this surface at three different channel separations. The effect of this roughness is clear, showing an increase of about 9% from conventional laminar theory for the 572 µm channel separation, and about 17% for the 439 µm channel separation. These two larger channel results are nearly within experimental error of each other, and for this reason, no larger channel separations were tested, as they would certainly converge to conventional laminar theory. The smallest channel separation resulted in friction factors that are 26% greater than laminar theory. All three test cases showed consistently later transitions to turbulence than predicted by conventional theory, although the transition Reynolds numbers were comparable to the results of the smooth channel tests.

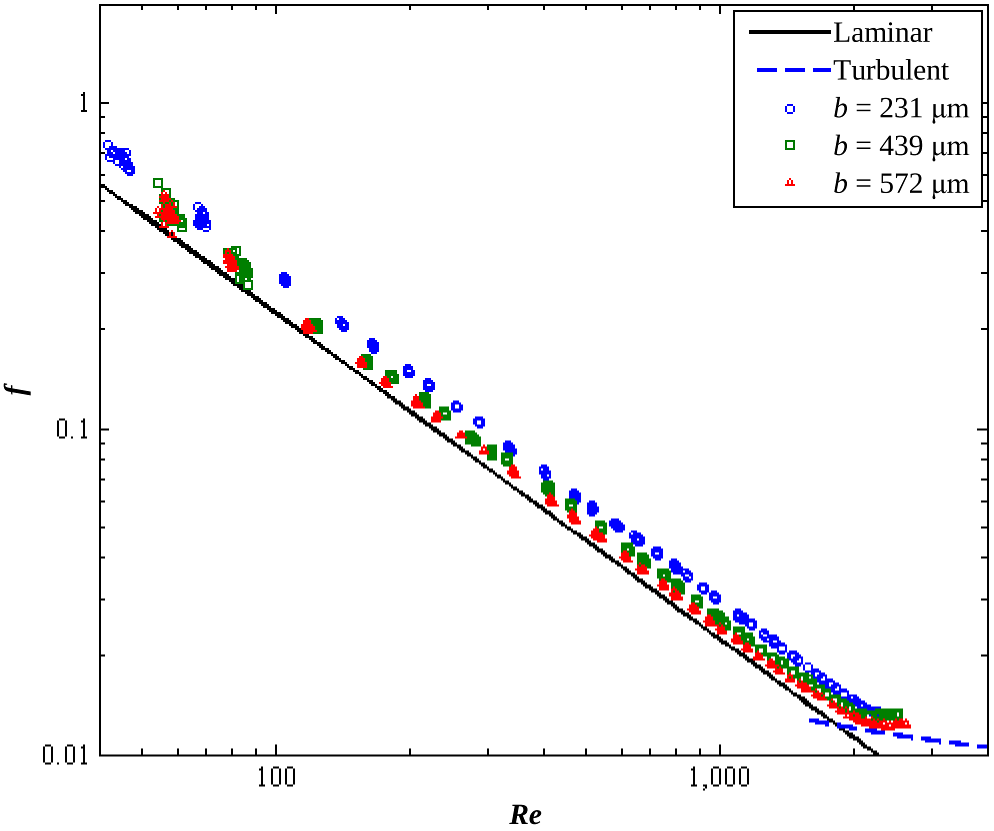

**Figure 33. Experimental Friction Factor vs. Reynolds Number, $\lambda/h = 7$**
**$b$ = 231, 439, and 572 µm**

The $\lambda/h$ = 8 surface is shown in Figure 34 below. Because of the increased distance between roughness elements, and the resulting larger pitch-to-height ratio, i.e. $\lambda/h$ = 8, it was expected that this surface would have a less pronounced effect on the friction factor than did the previous, $\lambda/h$ = 7 surface. However, the friction factors for the smallest channel separation were found to be 55% greater than conventional laminar theory predicted, as opposed to the mere 26% increase for the $\lambda/h$ = 7 and $b$ = 231 μm case. The data for the intermediate channel separations, 444 and 593 μm, are nearly indistinguishable from one another graphically, but both are significantly greater than conventional laminar theory; 26% and 19% greater, respectively. Data obtained from the 751 μm separation case is within error of laminar theory; about 5% greater.

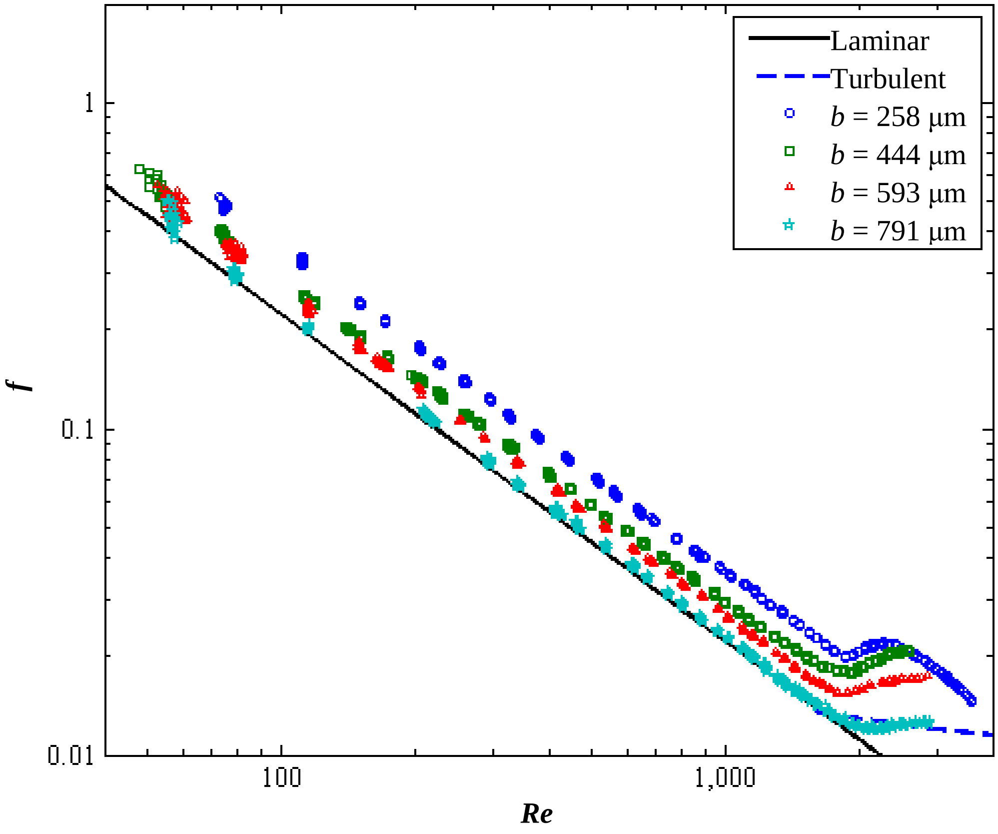

**Figure 34. Experimental Friction Factor vs. Reynolds Number, $\lambda/h$ = 8**
**$b$ = 258, 444, 593, and 791μm**

Transition Reynolds number for the $\lambda/h$ = 8 surface did not vary significantly with channel separation, but transition occurred later than predicted by conventional theory. Transition appeared to be more sudden or sharp for the smaller channel separations, as opposed to the slow or gradual increase seen for the 751 μm separation case. The 258 μm case consistently transitioned sharply then gradually decreased in all trials. Similar behavior of decreasing experimental friction factors was observed for the smooth channel when the 150 μm gauge block was used, and leakage ensued. This may indicate that for this test case, had flow rate been increased further, the test section may have proceeded to exhibit a slow leak at the inlet or outlet headers, as these were the areas prone to leak in high pressure flows.

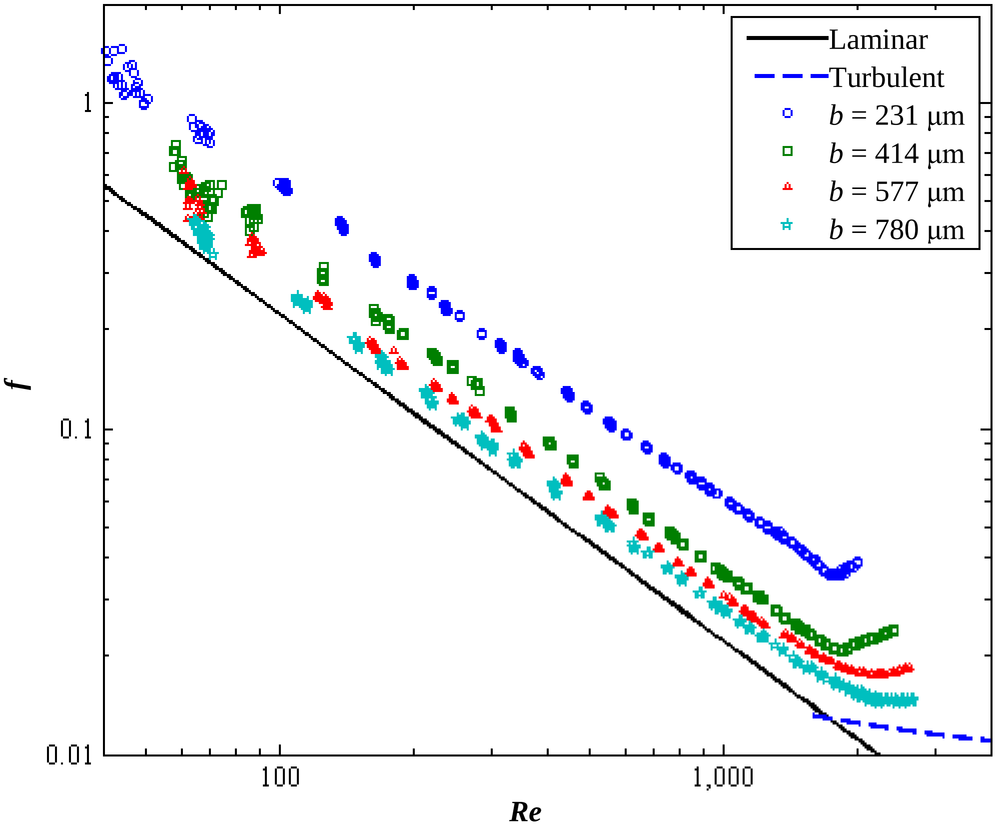

**Figure 35. Experimental Friction Factor vs. Reynolds Number, $\lambda/h = 5$**
**$b$ = 231, 414, 577, and 780 μm**

A pitch-to-height ratio of 5, as is the case in Figure 35 above, is indicative of transitional roughness (between *k*- and *d*-types). This roughness height is the same as in the $\lambda/h = 8$ plot (Figure 34), but the pitch is significantly smaller; 250.2 μm. For this surface, the largest channel separation tested, 780 μm, resulted in friction factors that were 23% greater than the laminar theory predicted. The next smaller channel separations, 577 and 414 μm, resulted in laminar friction factors 36% and 59% greater than conventional theory, respectively. The smallest channel separation, 231 μm, resulted in laminar friction factors that were 142% above conventional laminar theory. The transition

Reynolds number remained about the same for each channel separation, but as channel separation decreased, the transition became more abrupt, similar to the behavior of the $\lambda/h$ = 8 surface.

Figure 36, below, shows the results for the $\lambda/h$ = 3 surface, where the height remained the same as with the previous two plots, approximately 50 µm, but the pitch was the smallest attainable by wire EDM, about 150 µm. Similar to every set of experiments shown thus far, as the channel separation decreased, the friction factor increased. The interesting thing to note with this surface is that there is little difference between this and the previous $\lambda/h$ = 5 case, where the pitch was 250.2 µm. The largest channel separation for these surfaces, 751 µm, resulted in lower friction factors than the previous case, at 16% greater than laminar theory. The 552 and 414 µm channel separations saw a negligible increase compared to the $\lambda/h$ = 5 surfaces, whereas the 230 µm separation yielded slightly lower friction factors, at 125% above laminar theory. For this roughness pitch, transition occurred later for every channel separation than in the previous $\lambda/h$ = 5 case, but the same pattern of increasingly abrupt transition for decreasing channel size is still shown.

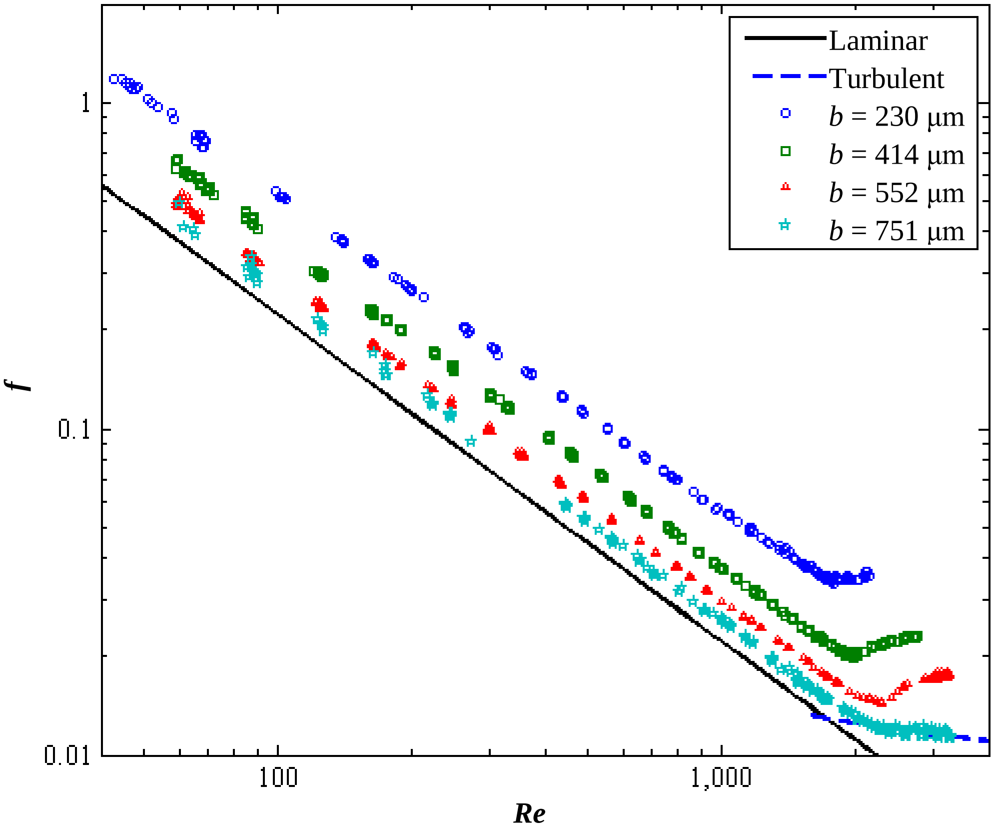

**Figure 36. Experimental Friction Factor vs. Reynolds Number, $\lambda/h$ = 3**
**$b$ = 230, 414, 552, and 751 µm**

The first thing to note for Figure 37 below is that, due to the increased roughness height of 131 µm, the 250 µm gauge blocks used for each previous surface could not be used. Thus the smallest channel separation is 377 µm. Also, because the 800 µm gauge blocks (resultant separation of 755 µm) had not resulted in friction factors comparable to smooth channel theory, the largest gauge block (1000 µm, resultant separation of 937 µm) was used. As channel size decreased, friction factor increased, and so the trend is consistent across all data sets. However, this roughness profile, and not the $\lambda/h$ = 8 profile, as noted by Coleman *et al*. [37] shows the most pronounced effect on friction factor, well into the minichannel range. Experimental friction factors for the largest channel separation were 71% greater than predicted by laminar theory, and for the smallest channel separation were 266% greater. Transition to turbulence for this surface occurred at increasingly lower Reynolds numbers as channel separation decreased, as can be seen in Figure 37. This differs from every previous test case, which saw greater transitional Reynolds numbers.

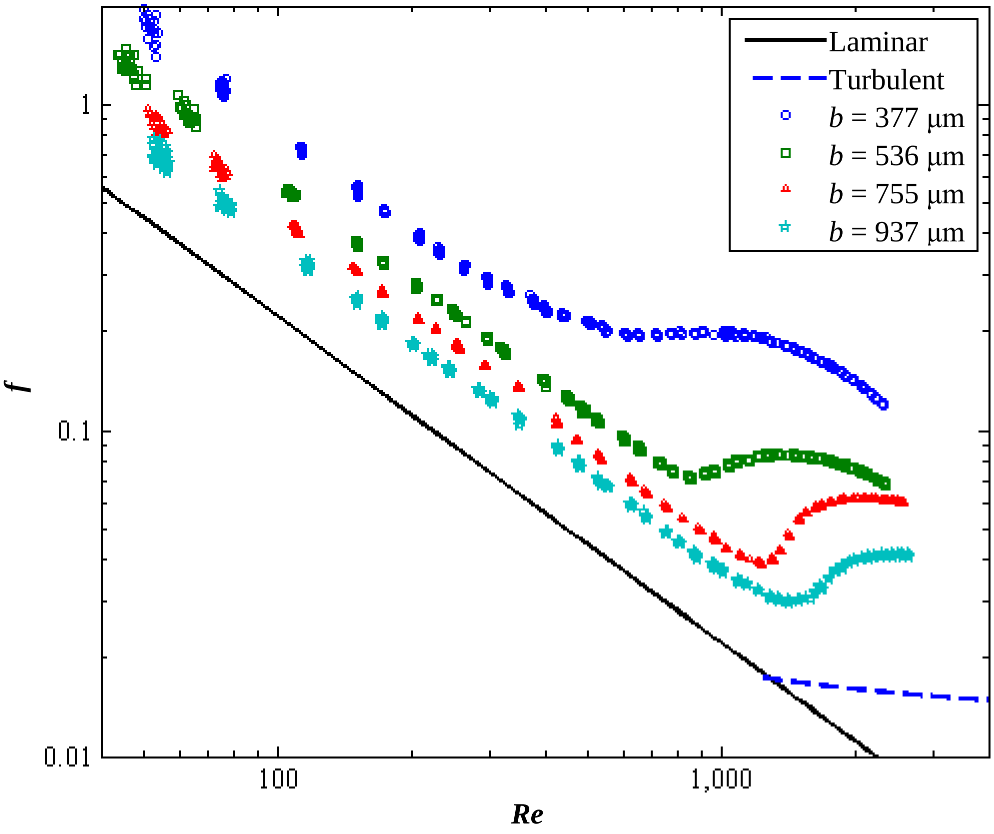

**Figure 37. Experimental Friction Factor vs. Reynolds Number, $\lambda/h$ = 2**
***b* = 377, 536, 755, and 937 µm**

Although turbulent flow was not one of the objectives of this work, all experiments were run at least up to the transition Reynolds number, which allowed for some observations to be made regarding the effect of roughness on transition. Transitional behavior has been discussed for each test case thus far, in terms of the shape or suddenness of the departure from laminar flow, as well as the relative critical Reynolds numbers. In general, transition occurred around *Re* = 1800, though some test cases saw an earlier transition as channel size decreased, particularly for the taller roughness cases, or the lower $\lambda/h$ surfaces. The $\lambda/h$ = 2 surface, for example, began to transition as early as *Re* = 370 for the smallest channel separation *b* = 377 μm, and *Re* = 780 for *b* = 536 μm.

As channel measurements were recorded throughout the course of testing, theoretical friction factors were calculated using the wall function method and the constricted flow method. These theoretical values were kept separate initially so as to let the data speak for itself. In the following sections, the experimental data is compared with the friction factors predicted by the wall function method and the constricted flow model. In addition, the data is compared more thoroughly and discussed more in-depth, in an attempt to ascertain the effects of changing pitch, height, and channel separation on flow.

## 6.3 Comparison with Wall Function Method

The next five figures show the previous experimental data plotted with the results of the wall function method. The theoretical friction factors were calculated using the MATLAB code shown in Appendix A. Measured channel geometry and roughness geometry were the only parameters input into the code. Fluid properties were assumed constant, and a range of flow rates were chosen such that the Reynolds numbers ranged from 5 to 3400. The same laminar and turbulent theory lines shown in previous plots (in black and blue, respectively) were maintained in these for comparison purposes. In the plot legends, the experimental data is referred to by the channel separation followed by “exp” and wall function method results are the channel separation followed by “theory.”

The wall function method does not attempt to predict a critical Reynolds number, and so no discussion of transition will be found in this section. Extension of the current theory to turbulent flow is an item for future work.

It was shown previously that the surface with the lowest roughness height *h* = 35.6 μm, resulting in a pitch-to-height ratio $\lambda/h$ = 7, had the least effect on friction factors for laminar flow as compared with the rest of the test pieces. The preliminary study of friction factors indicated that the wall function method would likely not provide an accurate prediction of pressure drop in a channel where the pitch-to-height ratio is large, due to the instability in the model for the combination of high roughness ratios and low channel aspect ratios. In contradiction with this assessment of the model, the wall function method was able to predict friction factors for this surface and all three channel separations exceptionally well, under-predicting by less than 4% for each channel separation. Figure 38 shows a plot of the experimental data and the corresponding theory lines obtained from the wall function method for the $\lambda/h$ = 7 surface.

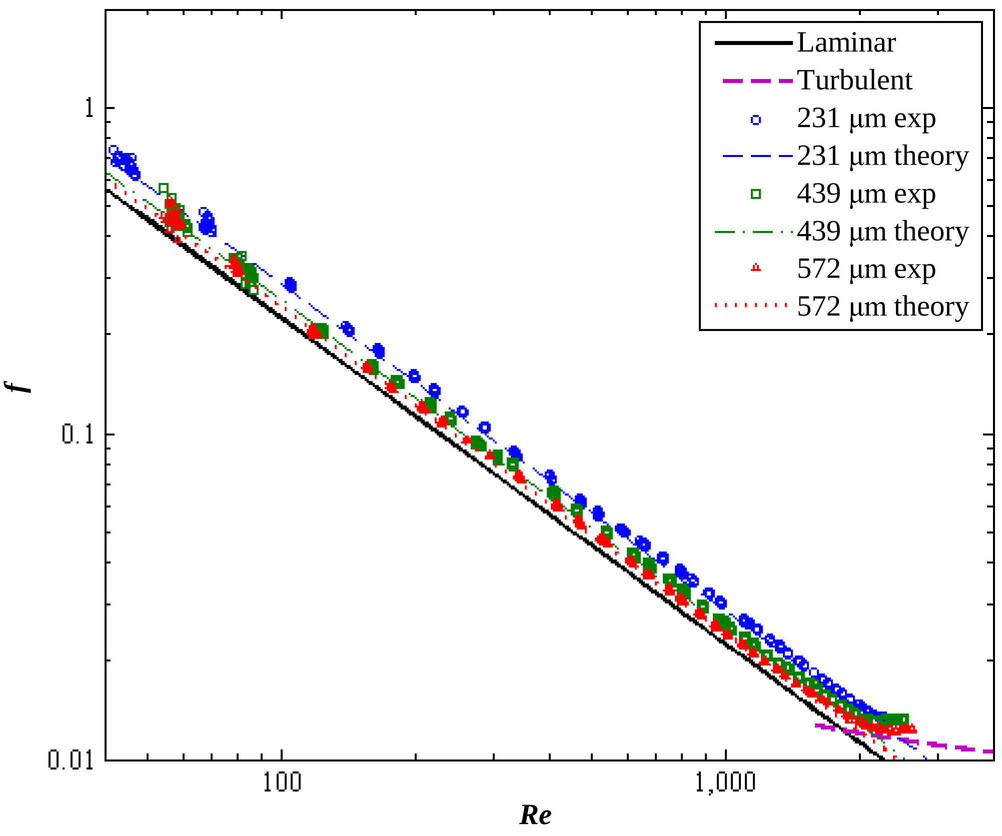

**Figure 38. Experimental and Theoretical Friction Factor vs. Reynolds Number, $\lambda/h$ = 7 $b$ = 231, 439, and 572 μm**

Figure 39 shows the wall function method predictions for friction factors for the $\lambda/h$ = 8 surface. Though a pitch-to-height ratio of 8 has been referred to as “transitional” roughness and may be expected to have the greatest effect on fluid flow, according to literature, it has been shown that this is not the case for the current sinusoidal surfaces (the $\lambda/h$ = 2 surface saw the greatest pressure loss). The $\lambda/h$ = 8 surface had the highest pitch, λ = 400.4 μm, and consequently had the highest cosine power; the variable which was indicated in the friction factor study as a potential source of instability. This power combined with the relatively high pitch-to-height ratio would indicate that the wall function method may fail to accurately predict the experimental data. The wall function method over-predicted the experimental data for the largest channel separation by about 4%, which was one of two cases in the entire data set where it over-predicted. The model under-predicted the smallest channel separation by 17%. The two intermediate channel separations, *b* = 444 and 593 μm, were found to be 26% and 55% greater than conventional laminar theory, respectively. But, the predictions from the wall function method were indistinguishable, at 16.5% and 16.9% above conventional laminar theory, respectively. Although the wall function method was able to correlate with the experimental data for the *b* = 593 μm case to within 2%, this surface resulted in the most irregular or inconsistent predictions.

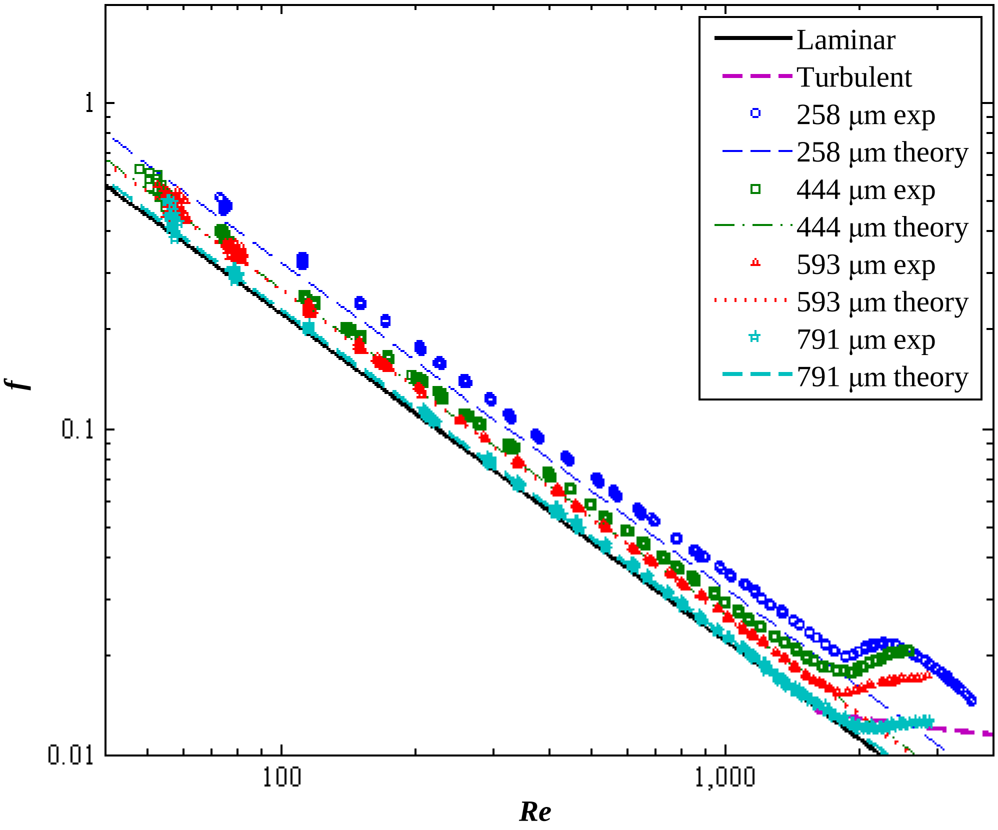

**Figure 39. Experimental and Theoretical Friction Factor vs. Reynolds Number, $\lambda/h$ = 8 *b* = 258, 444, 593, and 791μm**

The following figure shows the experimental data and wall function predictions for the $\lambda/h$ = 5 surface. The wall function method significantly under-predicted friction factors for all channel separations for this surface (see Figure 40). The data for the two largest channel separations, $b$ = 577 and 780 μm, fall 13% and 18% above predictions from the wall function method, respectively. Data for $b$ = 414 μm exceeded the constricted flow method's prediction by 29%, and the $b$ = 231 μm exceeded it by 88%. It is an interesting observation that the wall function method for $b$ = 231 μm correlates exceptionally well (to within 4%) with the experimental data for $b$ = 414 μm, and the same is true for the next two larger channel separations. Though the wall function method was thought to be capable of predicting friction factors for higher values of $\lambda/h$, this roughness profile does not adhere to the wall function method's predictions any more than the previous roughness profile.

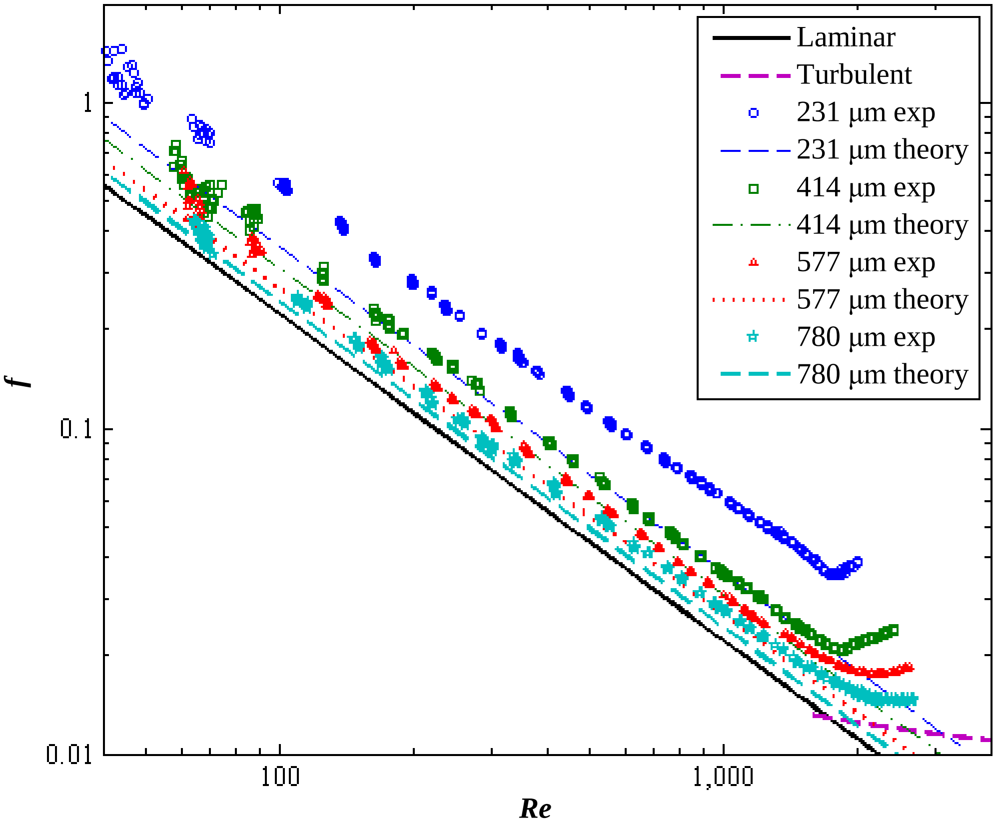

**Figure 40. Experimental and Theoretical Friction Factor vs. Reynolds Number, $\lambda/h$ = 5 $b$ = 231, 414, 577, and 780 μm**

The $\lambda/h$ = 3 surface has same roughness height and slope as the $\lambda/h$ = 5 surface, but the roughness elements are more closely spaced. The similarities in experimental data for these two surfaces were discussed in the previous section. Figure 41 below shows the wall function method's predictions for the $\lambda/h$ = 3 surface below. For the largest channel separation, the wall function predicted experimental friction factors exactly, with 0% error. The next channel separation's data fell within 3% of the wall function method's prediction. For $b$ = 414 and 230 µm, however, the data fell 27% and 23% above the wall function method's prediction, respectively.

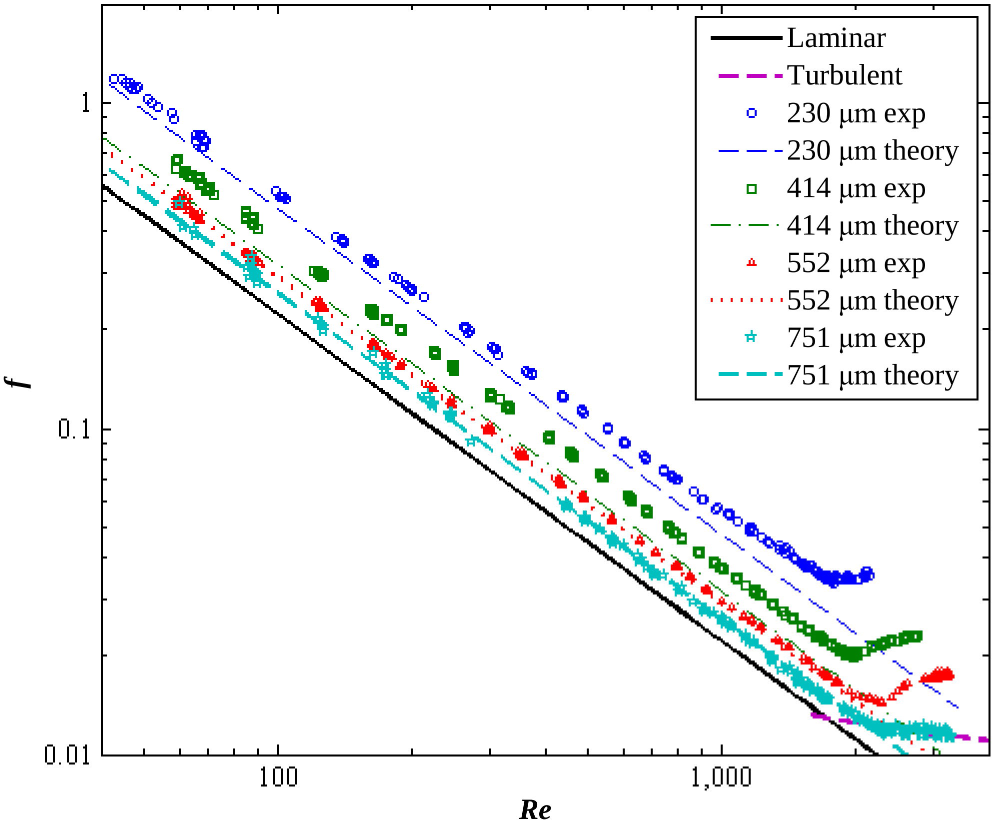

**Figure 41. Experimental and Theoretical Friction Factor vs. Reynolds Number, $\lambda/h$ = 3 $b$ = 230, 414, 552, and 751 µm**

Figure 42 shows the wall function method's predictions for the highest roughness tested; the $\lambda/h$ = 2 surface. Excellent agreement was found for the smallest channel separations, with experimental data falling within 2% of the wall function method friction factors for both $b$= 536 and 377 µm. This agreement was foreshadowed in the preliminary results section, where the range of low pitch-to-height ratios and small channel aspect ratios were expected to result in the greatest friction factors with the least instability. Percent error was somewhat different for the two larger channel separations; friction factors for $b$ = 755 µm were 25% greater than the wall function method, whereas for $b$ = 937 µm they were 8% lower. This is the second test case where the wall function method over-predicted frictional losses.

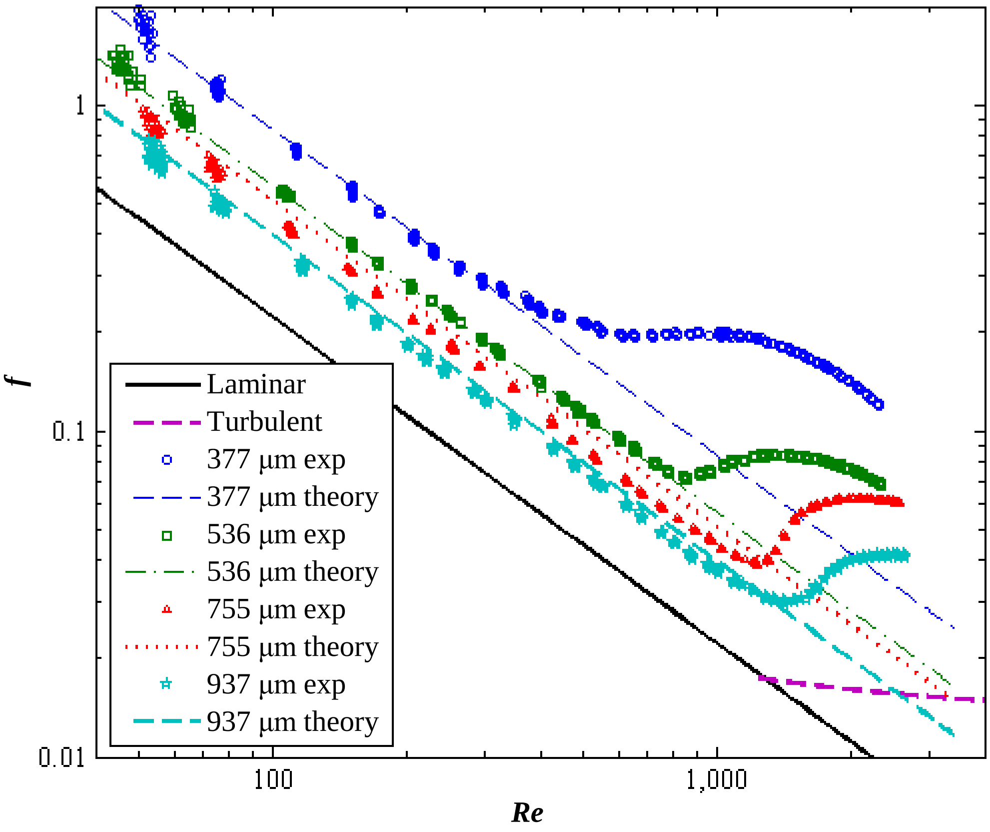

**Figure 42. Experimental and Theoretical Friction Factor vs. Reynolds Number, $\lambda/h$ = 2**
**$b$ = 377, 536, 755, and 937 µm**

Of the nineteen test cases presented here, nine were predicted to within experimental error by the wall function method. Those cases include the two largest $\lambda/h$ surfaces, with better agreement seen for the larger channel separations, and the two smallest $\lambda/h$ surfaces, with better agreement for the larger separations and the $\lambda/h$ = 3 surface, and better agreement for the smaller separations and the $\lambda/h$ = 2 surface. The $\lambda/h$ = 5 surface exhibited the poorest agreement with the wall function method's predictions for all channel separations tested.

A summary of percent error between the experimental data and both the smooth channel correlation and the wall function method for each test case is provided in Table 10 below. All experimental friction factors were found to be greater than conventional theory and percent difference increased as channel separation decreased, with the difference becoming more pronounced as $\lambda/h$ decreased. Similarly, experimental friction factors were found to be greater than the wall function method's predictions in all cases but for the largest channel separations for $\lambda/h$ = 8 and 2. The cases for which percent error is less than experimental error are highlighted in grey in Table 10.

**Table 10. Experimental Error**

| Pitch-to-Height Ratio | Separation | Aspect Ratio | Hydraulic Diameter | Relative Roughness | Height-to-Separation Ratio | % Error from Laminar Theory | % Error from Wall Function Method |
|---|---|---|---|---|---|---|---|
| *λ/h* | *b* | *α* | *Dh* | *h/Dh* | *h/b* | | |
| | µm | | µm | | | % | % |
| 7 | 231 | 0.02 | 455 | 8% | 0.15 | 26% | 4% |
| | 439 | 0.03 | 849 | 4% | 0.08 | 17% | 5% |
| | 572 | 0.05 | 1094 | 3% | 0.06 | 9% | 2% |
| 8 | 258 | 0.02 | 505 | 10% | 0.19 | 55% | 17% |
| | 444 | 0.03 | 858 | 6% | 0.11 | 26% | 8% |
| | 593 | 0.05 | 1134 | 4% | 0.08 | 19% | 2% |
| | 791 | 0.06 | 1489 | 3% | 0.06 | 5% | -4% |
| 5 | 231 | 0.02 | 453 | 11% | 0.21 | 142% | 88% |
| | 414 | 0.03 | 802 | 6% | 0.12 | 59% | 29% |
| | 577 | 0.05 | 1104 | 4% | 0.09 | 36% | 18% |
| | 780 | 0.06 | 1470 | 3% | 0.06 | 23% | 13% |
| 3 | 230 | 0.02 | 452 | 11% | 0.22 | 125% | 23% |
| | 414 | 0.03 | 801 | 6% | 0.12 | 65% | 27% |
| | 552 | 0.04 | 1058 | 5% | 0.09 | 31% | 3% |
| | 751 | 0.06 | 1419 | 3% | 0.07 | 16% | 0% |
| 2 | 377 | 0.03 | 732 | 18% | 0.35 | 266% | 1% |
| | 536 | 0.04 | 1029 | 13% | 0.24 | 150% | 2% |
| | 755 | 0.06 | 1425 | 9% | 0.17 | 103% | 25% |
| | 937 | 0.07 | 1745 | 8% | 0.14 | 71% | -8% |

Examining first the constant roughness pitch cases, where $\lambda/h$ = 7, 5, and 2, the roughness height effect on flow is evident, as the percent difference from smooth correlation increases significantly as roughness height increases for each channel separation. Even in the event that the relative roughness is the same for two surfaces, the friction factors are greater when roughness height is greater. For example, comparing percent errors for $h/D_h$ = 4%; the friction factors for the $\lambda/h$ = 7 surface are 17% greater than laminar theory, $\lambda/h$ = 5 are 36% greater. This behavior was expected, but the wall function method's predictive capability was surprising. For the constant pitch cases, the wall function method predicted the lowest $\lambda/h$ surface well for all separations, but for the next tallest roughness was unable to correlate with any of the data. This would not be surprising if the trend had continued and the wall function method continued to under-predict friction factors for the $\lambda/h$ = 2 surface. However, excellent agreement was found for the smaller channel separations, or lowest aspect ratios, while error increased for the larger channel separations.

The three cases for constant roughness height, $\lambda/h$ = 8, 5, and 3, all resulted in comparable relative roughness values for the channel separations tested, reinforcing the statement that the concept of relative roughness is not applicable for structured roughness elements. It was the $\lambda/h$ = 5 surface that exhibited the greatest effect on fluid flow, however, and not the $\lambda/h$ = 8 surface that was noted in the literature. On either side of the surface, for the lower and higher roughness pitches, percent error between the experimental data and laminar theory decreased, with the exception of the $\lambda/h$ = 3 surface and 414 µm channel separation. The same trend can be seen in the percent errors between experimental friction factors and those predicted by the wall function method.

Another method for comparison of experimental data is through the use of the Poiseuille number, $Po = f \cdot Re$, which is a constant in the laminar flow regime. This parameter varies with channel geometry, but was also found to increase with increasing roughness height, as the roughness caused laminar friction factors to increase, but had minimal effect on the Reynolds number. The variation in experimental Poiseuille number with roughness type and channel aspect ratio is shown in Figure 43 below. For the smooth channel case, the Poiseuille number was constant, $Po$ = 23, for all channel separations.

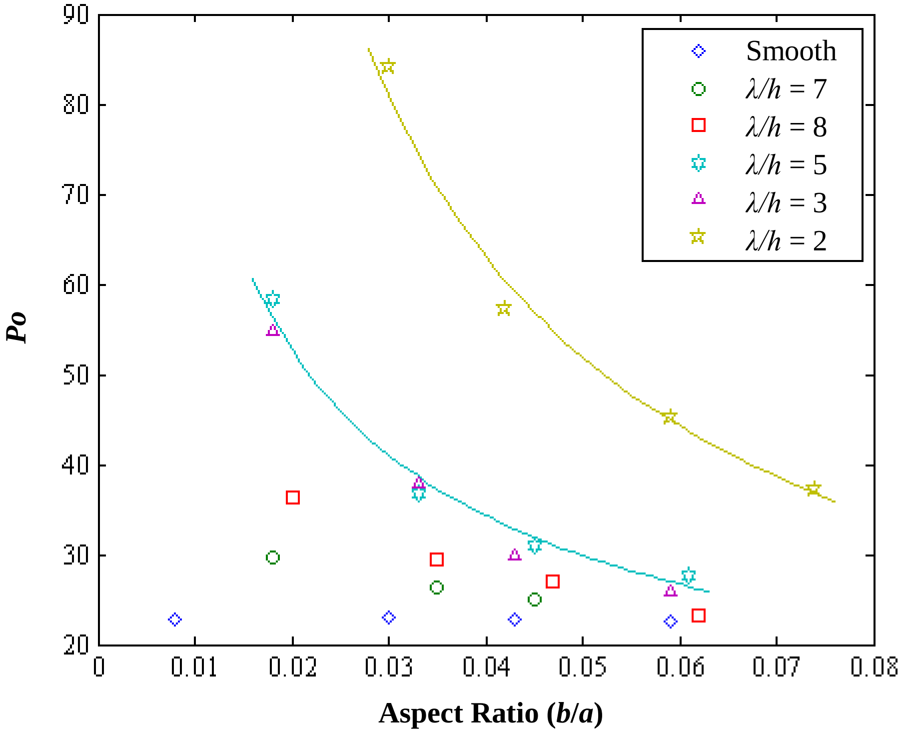

**Figure 43. Experimental Poiseuille Number vs. Channel Aspect Ratio**

The Poiseuille number is useful for comparison across an array of data sets where the Reynolds numbers are not consistent throughout. That is, plotting $f$ vs. $\alpha$, as was done in the Preliminary Results section, is nearly impossible for this section because not every test case was run for the same Reynolds numbers. Plotting the Poiseuille number versus aspect ratio, however, shows that the same asymptotic behavior seen in the Preliminary Results section was exhibited by the experimental data. As the roughness pitch-to-height ratios and the channel aspect ratios decreased, the Poiseuille numbers increased. The two curves shown in Figure 43 are intended to highlight the behavior of $Po$ as $\alpha$ varies, and do not represent a relevant function. Table 11 provides the Poiseuille numbers and normalized Poiseuille numbers for each test case. As channel aspect ratios increased, $Po$ for each rough case converged to $Po_{smooth}$, seen in the decrease of the normalized Poiseuille numbers. Neither friction factors nor Poiseuille numbers were correlated with the roughness pitch-to-height ratio, as too few channel separations or aspect ratios were tested to obtain a reasonable correlation.

**Table 11. Experimental Poiseuille Numbers**

| **Surface** | **Aspect Ratio** | **Poiseuille Number** | $Po/Po_{smooth}$ |
|---|---|---|---|
| | $\alpha$ | $Po$ | |
| **Smooth** | 0.01 | 23 | 1 |
| | 0.03 | 23 | 1 |
| | 0.04 | 23 | 1 |
| | 0.06 | 23 | 1 |
| $\lambda/h = 7$ | 0.02 | 30 | 1.31 |
| | 0.03 | 26 | 1.14 |
| | 0.05 | 25 | 1.09 |
| $\lambda/h = 8$ | 0.02 | 36 | 1.60 |
| | 0.03 | 29 | 1.28 |
| | 0.05 | 27 | 1.18 |
| | 0.06 | 23 | 1.03 |
| $\lambda/h = 5$ | 0.02 | 58 | 2.57 |
| | 0.03 | 37 | 1.59 |
| | 0.05 | 31 | 1.37 |
| | 0.06 | 28 | 1.22 |
| $\lambda/h = 3$ | 0.02 | 55 | 2.41 |
| | 0.03 | 38 | 1.65 |
| | 0.04 | 30 | 1.31 |
| | 0.06 | 26 | 1.15 |
| $\lambda/h = 2$ | 0.03 | 84 | 3.71 |
| | 0.04 | 57 | 2.49 |
| | 0.06 | 45 | 1.99 |
| | 0.07 | 37 | 1.65 |

## 6.4 Comparison with Constricted Flow Model

To review, the constricted flow model makes use of the amplitude parameter $\varepsilon_{Fp}$ in order to "constrict" the flow. In essence, it serves to account for the boundary layer in rough channel flows, and has been applied to experimental data in literature in order to force experimental data to adhere to conventional laminar theory for smooth channels.

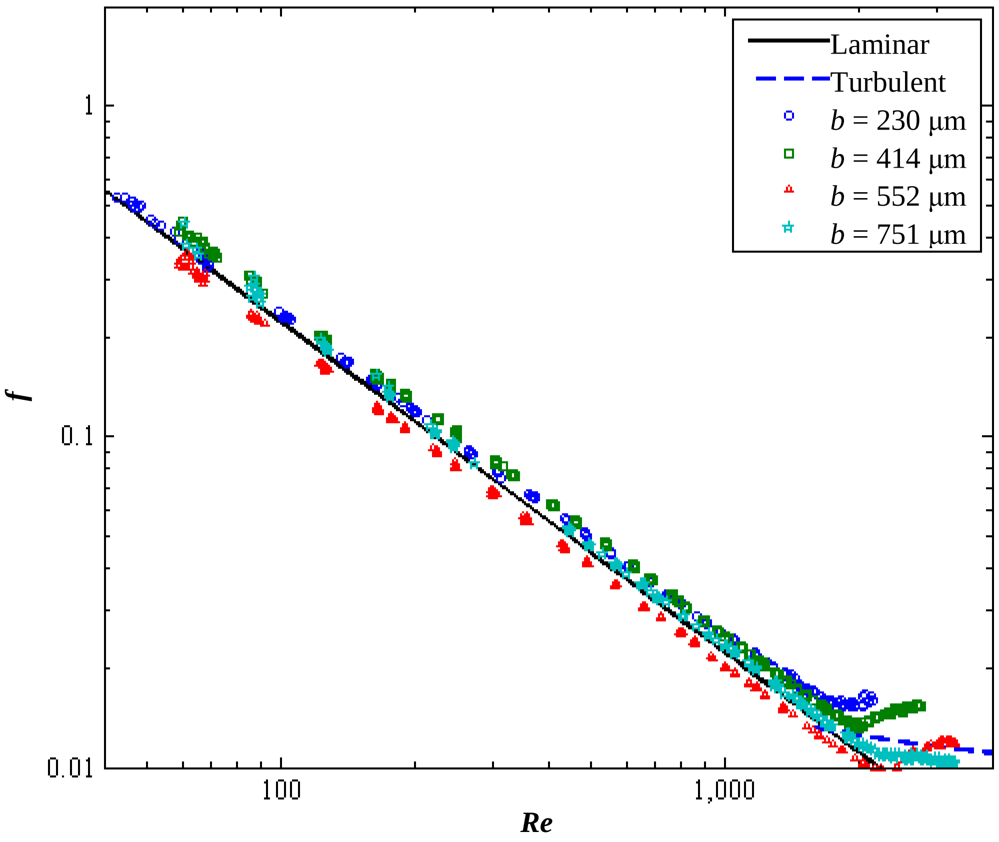

**Figure 44. Constricted Experimental Friction Factor vs. Reynolds Number, $\lambda/h = 3$**
**$b$ = 230, 414, 552, and 751 µm**

In applying the constricted flow model to the data at hand, the friction factors and Reynolds numbers, equations 17 and 21, respectively, were recalculated using the constricted geometry. Figure 44 provides an example of the outcome for the $\lambda/h = 3$ surface. The data shown were within 10% of laminar theory, the closest fit of all surfaces tested. The remaining test cases resulted in friction factors consistently lower than laminar theory when the constricted flow model was applied.

# 7 Conclusions

Laminar flow of an incompressible fluid in rectangular channels, possessing two-dimensional roughness, was investigated from a theoretical standpoint resulting in a model for pressure versus flow that allowed for the direct input of surface roughness geometry. This model is referred to as the wall function method. The primary focus was on long, small aspect ratio, rectangular channels in the mini- or microscale range. Structured roughness of a sinusoidal type was evaluated in order to control and vary the pitch and height. These surfaces were described by their roughness pitch-to-height ratios, $\lambda/h$. A test set and a series of roughness test pieces were fabricated for experimental assessment of the applicability of the wall function method.

Standard amplitude, spatial, and shape parameters were evaluated for the rough surfaces generated in order to determine a combination of parameters relevant to the sinusoidal-type roughness. The spatial parameter $R_{SM}$ was found to be in exact agreement with the designed roughness pitch, while the average step height, a non-standard parameter, was found to be in good agreement with the designed peak height. A more universal parameter is required for measurement of the peak height, and a method for designing and predicting the cosine power, which controls the peak slope, is also needed. Relative roughness, $\varepsilon_{Fp}/D_h$, was found to be an inconsistent means of representing structured roughness, as it does not vary sufficiently with roughness pitch or shape.

A series of experiments were run with degassed water flowing through channels possessing a range of roughness types, summarized in Table 13 in Appendix B. In every test case, friction factors were found to be greater than conventional laminar theory for smooth rectangular ducts. As channel aspect ratio decreased, or as the hydraulic diameter decreased, the experimental friction factors increased, with the increase becoming more pronounced for taller and more closely spaced roughness. No pattern was observed for the cases of constant roughness height and varying pitch, aside from the intermediate surface, $\lambda/h = 5$, exhibiting the largest friction factors of the three. It was noted in the literature that there is an intermediate pitch-to-height ratio that would yield the greatest effect on fluid flow. However, in these experiments, it was the smallest pitch-to-height ratio, $\lambda/h = 2$, that exhibited the largest friction factors.

Comparing experimental data with the friction factors obtained from the wall function method uncovered some unexpected results. First, the surface for which $\lambda/h$ was greatest ($\lambda/h = 8$) was expected to show more instability than the rest in the wall function method, but data for this surface was within experimental error of the wall function method for the two larger channel cases. The next largest pitch-to-height ratio was the short profile, $\lambda/h = 7$, which was expected to have the least effect on fluid flow, and was predicted best by the wall function method out of all the sinusoidal surfaces. The intermediate surface, for which $\lambda/h = 5$, was the most unpredictable of the surfaces tested, and resulted in the poorest comparison with the wall function method. This pitch-to-height ratio is considered the transition between *d*-type and *k*-type roughness. The surface of $\lambda/h = 3$ saw friction factors comparable to those of the $\lambda/h = 5$ surface, though were consistently lower. The wall function method predicted the largest two channel separations for this surface to well within experimental uncertainty. The final and tallest surface roughness, $\lambda/h = 2$, had the most pronounced effect on fluid flow, with percent errors in excess of 100% compared with smooth channel theory. The wall function method predicted the two smallest channel separations for this surface exceptionally well, which is contrary to the previous cases where larger channel separations were predicted successfully.

Though the wall function method had some success, and is consistent with the smooth channel correlation, only nine of the nineteen rough cases were able to be predicted with the wall function method. The limits of the lubrication approximation were tested by increasing the Reynolds number and the surface roughness, and in spite of exceeding those limits, the analysis still saw some success. A potential reason for the poor predictive capability may be due to the range of Reynolds numbers tested. The analysis was made for laminar flow, true, but the experimental flows may not have been laminar enough. In terms of scale analysis, the Reynolds number multiplied by the aspect ratio, $Re \cdot \alpha$, should be approximately 1. Though the aspect ratios were sufficiently small, the lowest flow rates obtained with the experimental test setup were limited to $Re \geq 40$. The analysis should be more successful for Stokes flow.

Other potential sources of error may be alleviated through improvements to the experimental test setup. Entrance and exit effects that were neglected in the theoretical analysis may not have been entirely negligible for smaller channel separations. The non-uniformity of the channel cross-section, although minimized during testing, might imply that the channel could have deflected for higher flow rates. Alignment of roughness elements may have contributed to uncertainty in the hydraulic performance of the various surfaces. Uncertainties and errors in instrumentation, measurement, and measurement locations in general could also be improved.

Overall, the limits of the wall function method were tested and it was shown that it is possible to predict frictional losses in a significantly rough microchannel without the complex computations of the fluid in the near wall region.

# 8 Recommendations

As with all experimental reports, more data is required in order to make a definite conclusion. A greater range of $\lambda$, $h$, and $p$ combinations, with more precise geometric similitude across all cases, together with the ability to vary channel height, would shed some light on the grey areas of this work. In addition, a more extensive sensitivity study on these roughness parameters would complete the information put forth in the Preliminary Results section; more specifically, the effect of varying roughness height on wall function friction factors should be expanded. A shape parameter must also be identified to estimate sinusoid power for the roughness studied in this work.

Roughness shape has been noted in the literature as playing a role in fluid flow, and for this reason different roughness geometries should be tested for comparison with the wall function method. A series of roughness test pieces with square geometry have been generated to fit in the existing test set. Smooth continuous functions need to be developed for the new geometries. Alternatively, the code presented in the Appendix could be modified to allow the user to input profile data for analysis. This approach would be ineffective for complex geometries, however, as well as for the extended analysis where the roughness slope is required. The direction of roughness elements may also play a role, particularly for thermal applications where longitudinal roughness may enhance heat transfer. Thus another extension of the current work would be to investigate the same roughness profiles rotated at 90 degrees, such that the peaks and grooves are parallel to the flow, and at other oblique angles.

A few simple improvements to the experimental apparatus could extend its capabilities into the turbulent regime. Also, a smaller pump (perhaps a syringe pump) and a lower range flowmeter would allow for lower Reynolds number data, which is essential for the theoretical analysis presented herein. Ideally, a single flowmeter that works well over all ranges of flow rate, from Stokes flow to the fully turbulent regime, would reduce error in switching between flowmeters, reduce the number of calibrations to be performed, and reduce the amount of data processing.

The test set as-is could easily be enhanced for use with micro-PIV (particle imaging velocimetry). The aluminum lid may be replaced by a transparent structural plastic, though sealing would need to be readdressed. This was kept in mind during the design stages, as it would be of great interest to understand the growth of vortices between the roughness elements studied here. Micro-PIV would also allow for visual verification of the flow profile development.

From the theoretical standpoint, it is imperative that the further analysis based on the augmented lubrication approximation be carried out. A method for evaluating the inertial integral must be established, but an approximation may be sufficient. The inertial integral from equation 16 is:

$$\frac{6\rho Q^2}{5a^2}\int_0^L \left( \frac{\frac{\partial g(x)}{\partial x} - \frac{\partial f(x)}{\partial x}}{\left(g(x) - f(x)\right)^3} \right) \partial x$$

To simplify this integral, the wall function slopes $\frac{\partial g(x)}{\partial x}$ and $\frac{\partial f(x)}{\partial x}$ may be taken to be the maximum slope of an individual asperity on the periodic surface. In the case of the $\lambda/h = 5$ surface, for example, the maximum slope is 1.35, resulting in a maximum slope difference of 2.70. Taking another simplification, after the constricted flow method, the integral reduces to

$$\frac{6\rho Q^2}{5a^2}\frac{L}{b_{cf}^3}\cdot 2.70$$

Comparing this integral with the viscous portion gives an indication of the range of applicability of this augmented lubrication approximation:

$$0.27\frac{\rho Q}{a\mu} << 1$$

Within this criterion, the inertial term is negligible, and the wall function method is sufficient. If, for example, the flow rate exceeds this limit for the geometry herein, then the augmented lubrication approximation may provide some improvement.

# 9 References

[1] Moody, L.F., 1944, “Friction factors for pipe flow,” Transactions of ASME, 66, pp. 671-684.

[2] Von Mises, R., 1914, “Elemente der Technischen Hydromechanik,” Leipzig, B.G. Teubner.

[3] Kandlikar, S. G., Schmidt, D., Carrano, A. L., and Taylor, J. B., 2005, “Characterization of Surface Roughness Effects on Pressure Drop in Single-Phase Flow in Minichannels and Microchannels,” Physics of Fluids, **17** (10), pp. 962–968.

[4] Brophy, J., 2005, “The Microchannel Revolution,” Focus on Catalysts, **2005** (2), pp. 1-2.

[5] Schlichting, H., 1949, “Vortragsreihe,” (“Lecture Series ‘Boundary Layer Theory’ - Part I: Laminar Flows”) NACA TM No. 1217.

[6] Darcy, H., 1857, “Recherches Experimentales Relatives au Mouvement de L'Eau dans les Tuyaux,” (“Experimental Research Relating to the Movement of Water in Pipes”), Mallet-Bachelier, Paris.

[7] Hopf, L., 1923, “Die Messung der Hydraulischen Rauhigkeit,” (“The measurement of hydraulic roughness”), Zeitschrift für Angewandte Mathematik und Mechanik, **3**, pp. 329-339.

[8] Fromm, K., 1923, “Strömungswiderstand in Rauhen Rohren,” (“Flow resistance in rough pipes”), Zeitschrift für Angewandte Mathematik und Mechanik, **3**, pp. 339-358.

[9] Nikuradse, J., 1933, “Strömungsgesetze in Rauhen Rohren,” (“Laws of Flow in Rough Pipes”) NACA TM No. 1292.

[10] Colebrook, C.F., 1939, “Turbulent flow in pipes with particular reference to the transition region between the smooth and rough pipe laws,” Journal of the Institute of Civil Engineers, **4**, pp. 133–156.

[11] Kandlikar, S.G., Garimella, S., Li, D., Colin, S., King, M.R., 2006, Heat Transfer and Fluid Flow in Minichannels and Microchannels, Elsevier, Oxford.

[12] Shah, R.K., 1972, “Laminar Flow Forced Convection Heat Transfer and Friction in Straight and Curved Ducts – A Summary of Analytical Solutions,” Stanford University, Palo Alto, CA.

[13] Shah, R. K., 1975, “Laminar Flow Friction and Forced Convection Heat Transfer in Ducts of Arbitrary Geometry,” International Journal of Heat and Mass Transfer, **18**, pp. 849-862.

[14] Mala G.M., Dongqing L.1, Dale J.D., 1997, “Heat Transfer and Fluid Flow in Microchannels,” International Journal of Heat and Mass Transfer, **40** (13), pp. 3079-3088.

[15] Papautsky, I., Gale, B.K., Mohanty, S., Ameel, T.A., Frazier, A.B., 1999, "Effects of Rectangular Microchannel Aspect Ratio on Laminar Friction Constant," *Proceedings of SPIE – The International Society for Optical Engineering, Proceedings of the 1999 Microfluidic Devices and Systems II*, Santa Clara.

[16] Wu, H.Y. and Cheng, P., 2003, "Friction Factors in Smooth Trapezoidal Silicon Microchannels with Different Aspect Ratios," International Journal of Heat and Mass Transfer, **46**, pp. 2519–2525

[17] Li, Z.X., Du, D.X., Guo, Z.Y., 2003, "Experimental Study on Flow Characteristics of Liquid in Circular Microtubes," Microscale Thermophysical Engineering, **7** (3), pp. 253-265.

[18] Pfahler, J., Harley, J., Bau, H., and Zemel, J.N., 1991, "Gas and Liquid Flow in Small Channels," *Micromechanical Sensors, Actuators, and Systems*, ASME, **32**, pp. 49-61.

[19] Yu, D., Warrington, R., Barron, R., Ameel, T., 1995, "Experimental and Theoretical Investigation of Fluid Flow and Heat Transfer in Microtubes," *Proceedings of the 1995 ASME/JSME Thermal Engineering Joint Conference*, Maui, Hawaii.

[20] Judy, J., Maynes, Webb, D.B. W., 2002, "Characterization of Frictional Pressure Drop for Liquid Flows through Microchannels," International Journal of Heat and Mass Transfer, **45** (17), pp. 3477-3489.

[21] Tu, X. and Hrnjak, P., 2003, "Experimental Investigation of Single-Phase Flow Pressure Drop Through Rectangular Microchannels," *Proceedings of the 1st International Conference on Microchannels and Minichannels*. Rochester, NY.

[22] A. Bucci, G.P. Celata, M. Cumo, E. Serra, and G. Zummo, 2003, "Water Single-Phase Fluid Flow and Heat Transfer in Capillary Tubes," *Proceedings of the 1st International Conference on Microchannels and Minichannels*. Rochester, NY.

[23] Bavière, R., Ayela, F., Le Person, S. and Favre-Marinet, M., 2005, "Experimental Characterization of Water Flow through Smooth Rectangular Microchannels," Physics of Fluids, **17**, 1–4.

[24] Akbari, M., Bahrami, M., and Sinton, D., 2009, "Flow in Rectangular Microchannels: an Experimental Investigation," ASME Journal Fluid Engineering, Vol. 131, pp. 041203-1-10.

[25] Peng, X.F., and Peterson, G.P., 1995, "Convective Heat Transfer and Flow Friction for Water Flow in Microchannel Structures," International Journal of Heat and Mass Transfer, **39** (12), pp. 2599-2608.

[26] Peng, X.F., Peterson, G.P., and Wang, B.X., 1994, "Frictional Flow Characteristics of Water Flowing Through Rectangular Microchannels," Experimental Heat Transfer, **7**, pp. 249-264.

[27] Kandlikar, S.G. and Grande, W.J., 2003, "Evolution of Microchannel Flow Passages--Thermohydraulic Performance and Fabrication Technology," Heat Transfer Engineering, **24** (1), pp. 3-17.

[28] Mehendale, S.S., Jacobi, A.M., Shah, R.K., 1999, Heat exchangers at micro- and meso-scales, in: R.K. Shah (Ed.), Compact Heat Exchangers and Enhancement Technology for the Process Industries, Begell House, New York, pp. 55–74.

[29] Bahrami, M., Yovanovich, M.M., Culham, J.R., 2007, "A Novel Solution for Pressure Drop in Singly Connected Microchannels," International Journal of Heat and Mass Transfer, **50**, pp. 2492-2502.

[30] Menezes, P.L., Kishore, and Kailas, S.V., 2008, "Influence of Roughness Parameters on Coefficient of Friction Under Lubricated Conditions," Sādhanā, Academy Proceedings in Engineering Sciences, **33** (3), pp. 181-190.

[31] Schlichting, H., 1936, "Experimentelle Untersuchungen zum Rauhigkeitsproblem," ("Experimental Investigation of the Problem of Surface Roughness") NACA TM No. 823.

[32] Sams, E. W., 1952, "Experimental Investigation of Average Heat Transfer and Friction Coefficients for Air Flowing in Circular Tubes Having Square-Thread-Type Roughness," NACA RM E52D17.

[33] Rawool, A.S., Mitra, S.K., Kandlikar, S.G., 2006, "Numerical Simulation of Flow Through Microchannels with Designed Roughness," Microfluidics and Nanofluidics, **2** (3), pp.215-221.

[34] Wang, X.Q., Yap, C., and Mujumdar, A.S., 2005, "Effects of Two-dimensional Roughness in Flow in Microchannels," Journal of Electronic Packaging, **127** (3), pp. 357–361.

[35] Sun, H. and Faghri, M., 2003, "Effect of Surface Roughness on Nitrogen Flow in a Microchannel Using the Direct Simulation Monte Carlo method," Numerical Heat Transfer, Part A: Applications: An International Journal of Computation and Methodology, **43** (1), pp. 1-8.

[36] Jiménez, J., 2004, "Turbulent Flows Over Rough Walls," Annual Review of Fluid Mechanics, **36**, pp. 173-196.

[37] Coleman, S.E., Nikora, V.I., McLean, S.R., and Schlicke, E., 2007, "Spatially Averaged Turbulent Flow Over Square Ribs," Journal of Engineering Mechanics, **133** (2), pp. 194-204.

[38] Mala, G.M. and Li, D., 1999, “Flow Characteristics of Water in Microtubes,” International Journal of Heat and Fluid Flow, **20**, pp. 142-148.

[39] Sabry, M.N., 2000, “Scale Effects on Fluid Flow and Heat Transfer in Microchannels,” IEEE Transactions on Components and Packaging Technologies, **23** (3), pp. 562-567.

[40] Koo, J. and Kleinstreuer, C., 2003 “Liquid Flow in Microchannels: Experimental Observations and Computational Analyses of Microfluidics Effects,” Journal of Micromechanics and Microengineering, **13**, pp. 568–579.

[41] Kleinstreuer, C. and Koo, J., 2004, “Computational Analysis of Wall Roughness Effects for Liquid Flow in Micro-conduits,” Journal of Fluids Engineering, **126** (1), pp. 1–9.

[42] Gamrat, G., Favre-Marinet, M., Le Person, S., Bavière, R., and Ayela, F., 2008, “An Experimental Study and Modelling of Roughness Effects on Laminar Flow in Microchannels,” Journal of Fluids Mechanics, **594**, pp. 399–423.

[43] Gamrat, G., Favre-Marinet, M., and Le Person, S., 2009, Modelling of Roughness Effects on Heat Transfer in Thermally Fully-developed Laminar Flows through Microchannels,” International Journal of Thermal Sciences, **48** (12), pp.2203-2214 .

[44] Brackbill, T. P., 2008, “Experimental Investigation on The Effects of Surface Roughness on Microscale Liquid Flow,” Rochester Institute of Technology, Rochester, NY.

[45] Weinstein, S., 2009, Personal Communication.

[46] Brackbill, T. P. and Kandlikar, S. G., 2006, “Effect of Triangular Roughness Elements on Pressure Drop and Laminar-Turbulent Transition in Microchannels and Minichannels,” *Proceedings of the 4th International Conference on Nanochannels, Microchannels, and Minichannels*, Limerick, Ireland.

[47] Brackbill, T. P., and Kandlikar, S. G., 2008, “Effects of Roughness on Turbulent Flow in Microchannels and Minichannels,” *Proceedings of the Sixth International ASME Conference on Nanochannels, Microchannels and Minichannels*, Darmstadt, Germany.

[48] Young, P. L., Brackbill, T.P. and Kandlikar, S.G., 2009, “Comparison of Roughness Parameters for Various Microchannel Surfaces in Single-Phase Flow Applications,” Heat Transfer Engineering, **30** (1), pp. 78 - 90.

[49] Fox, R.W., McDonald, A.T., and Pritchard, P.J., 2004, <u>Introduction to Fluid Mechanics</u>, John Wiley & Sons, New York.

[50] Viswanath, D.S., Ghosh, T.K, Prasad, D.H.L., and Rani, K.Y., 2006, <u>Viscosity of Liquids: Theory, Estimation, Experiment, and Data</u>, Springer, Dordrecht, Netherlands.

[51] Kakaç, S, Shah, R. K., Aung, W., 1987, Handbook of Single-Phase Convective Heat Transfer, John Wiley & Sons, New York.

[52] Brown, G. O., 1994, "The History of the Darcy–Weisbach Equation for Pipe Flow Resistance," Proceedings of the Environmental and Water Resources History, Reston, VA.

[53] Stanton, T. E. and Pannell, J. R., 1914, "Similarity of Motion in Relation to the Surface Friction of Fluids," Philosophical Transactions of the Royal Society of London, Series A, **214**, pp. 199-224.

[54] Taylor, J.B., Carrano, A.L., Kandlikar, S.G., "Characterization of the Effect of Surface Roughness and Texture on Fluid Flow – Past, Present, and Future," International Journal of Thermal Sciences, **45** (10), pp. 962-968.

[55] Doering, C. R., 2009, "The 3D Navier-Stokes Problem," Annual Review of Fluid Mechanics, **41**, pp. 109-128.

# Appendix A – MATLAB Code

The following code was used to calculate theoretical friction factors for the two-dimensionally rough surfaces using the wall function method and constricted flow method. Fluid properties were relatively constant across all test cases, and were updated as needed. The wall function variables, roughness parameters, and channel separation were updated according to each test case.

```
%%% Calculation of friction factors based on wall functions
%%% Wall function format: A*cos(B*x + C)^D + E

clear all
clc
format long
tic

%%% Fluid Properties
mu = 0.000893; % N.s/m^2               % viscosity
rho = 997.1; % kg/m^3                  % density

%%% Surface Geometry
l = 149.8; % um                        % pitch
h = 49.6; % um                         % height
p = 4;                                 % power

%%% Surface Parameters (in microns)
ep = 27.7;                             % constricted parameter
Rq = 9.9;                              % RMS roughness
Ra = 8.6;                              % average roughness

% Channel Geometry (in microns)
a = 12700;                             % channel height
b = 250;                               % root separation
bcf = b - 2*ep;                        % constricted separation
bRa = b - 2*Ra;
A = a*b;                               % cross-sectional area
Acf = a*bcf;                           % constricted area
ARa = a*bRa;
P = 2*a + 2*b;                         % perimeter
Pcf = 2*a + 2*bcf;                     % constricted perimeter
PRa = 2*a + 2*bRa;
Dh = 4*A/P;                            % hydraulic diameter
Dhcf = 4*Acf/Pcf;                      % constricted diameter
DhRa = 4*ARa/PRa;
L = 25400;                             % distance (1.0 in)
x = 0:L;

%%% Flow Rates and Velocity
Re = [5:5:45, 50:50:3400];             % Reynolds Number
Q = mu*A.*Re.*10^-6./(rho*Dh);         % Flow rate in m3/s
```

```
G = Q/0.000000017;
v = Q./(A*(10^-6)^2); % m/s          % velocity
vcf = Q./(Acf*(10^-6)^2);            % constricted velocity
vRa = Q./(ARa*(10^-6)^2);

%%% Constricted Reynolds Numbers
Recf = rho*Q*Dhcf/(mu*Acf)*10^6;
ReRa = rho*Q*DhRa/(mu*ARa)*10^6;

%%% Channel setup
% lower wall
f = h.*cos(x.*pi./l).^p - b/2;
df = -(pi*h*p.*(cos(x.*(pi/l)).^(p - 1)).*sin(x.*(pi/l)))/l;

% upper wall
g = -h.*cos(x.*pi/l).^p + b/2;
dg = (pi*h*p.*(cos(x.*(pi/l)).^(p - 1)).*sin(x.*(pi/l)))/l;

%%% Plot Channel & Roughness
figure(1)
plot(x, f, x, g)
axis([0 b+100 -b/2-50 b/2+50])

%%% Define Integrand
% y = 1/(g - f)^3
y = @(z) 1./(b - 2*h.*cos(z.*(pi/l)).^p).^3; % 1/um^3

figure(2)
ezplot(y)

%%% Approximate Int(1/(g - f)^3)
q1 = quad(y,0,L,1.0e-6);  % 1/um^2

%%% Calculate Theoretical Pressure-drop
% dP = (12*mu*Q/a)*q1
dP = (12*mu.*Q./(a*10^-6))*q1*(10^6)^2;

%%% Calculate Friction Factor
f = Dh.*dP./(2*L*rho*v.^2);

%%% Output
disp('~~Wall Function Analysis~~')
disp(['Pitch = ', num2str(l), ' um'])
disp(['Height = ', num2str(h), ' um'])
disp(['Pitch-Height Ratio = ', num2str(l/h)])
disp(['Separation = ', num2str(b), ' um'])
disp(' ')
disp('           Re                dP                  f')
disp('                            kPa')
Wall = [Re', dP'*10^-3, f'];
disp(Wall)
disp(' ')
```

```
%%% Constricted Flow Method
% dPcf = (12*mu*Q/a)*(L/beff^3);
% beff = bcf or bRa
beff = bcf;
dPcf = (12*mu.*Q/a)*(L/beff^3)*(10^6)^3;
% Dheff = Dhcf or DhRa, and veff = vcf or vRa
Dheff = Dhcf;
veff = vcf;
fcf = Dheff.*dPcf./(2*L*rho*veff.^2);

disp('~~Constricted Flow Analysis~~')
disp(['Constricted Parameter, ep = ', num2str(ep)])
%disp(['Average Roughness, Ra = ', num2str(Ra)])
disp(' ')
disp('           Re,cf             dP,cf              f,cf')
disp('                             kPa')
Constr = [Recf', dPcf'*10^-3, fcf'];
disp(Constr)
disp(' ')

%%% Correlation for Smooth Channels
alpha = b/a;
flam = 24*(1-1.3553*alpha+1.9467*alpha^2-1.7012*alpha^3+0.9564*alpha^4-
0.2537*alpha^5)./Re;

%%% Plot f vs. Re
figure(3)
loglog(Re, flam,'k', Re, f,'b', Recf, fcf,':g','LineWidth',2)


toc
```

# Appendix B – Test Matrices

**Table 12. Designed Test Matrix**

| **Asperity Dimensions** | | | **Channel Dimensions** | | | | |
|---|---|---|---|---|---|---|---|
| **Pitch** | **Height** | **Aspect Ratio** | **Separation** | **Aspect Ratio** | **Hydraulic Diameter** | **Relative Roughness** | **Height-Separation Ratio** |
| $\lambda$ | $h$ | $\lambda/h$ | $b$ | $\alpha$ | $D_h$ | $h/D_h$ | $h/b$ |
| **µm** | **µm** | **---** | **µm** | **---** | **µm** | **---** | **---** |
| 250 | 125 | 2 | 400 | 0.03 | 776 | 16% | 0.35 |
| | | | 600 | 0.05 | 1146 | 11% | 0.24 |
| | | | 800 | 0.06 | 1505 | 8% | 0.17 |
| | | | 1000 | 0.08 | 1854 | 7% | 0.14 |
| 150 | 50 | 3 | 250 | 0.02 | 490 | 10% | 0.22 |
| | | | 450 | 0.04 | 869 | 6% | 0.12 |
| | | | 600 | 0.05 | 1146 | 4% | 0.09 |
| | | | 800 | 0.06 | 1505 | 3% | 0.07 |
| 250 | 50 | 5 | 250 | 0.02 | 490 | 10% | 0.21 |
| | | | 450 | 0.04 | 869 | 6% | 0.12 |
| | | | 600 | 0.05 | 1146 | 4% | 0.09 |
| | | | 800 | 0.06 | 1505 | 3% | 0.06 |
| 400 | 50 | 8 | 250 | 0.02 | 490 | 10% | 0.19 |
| | | | 450 | 0.04 | 869 | 6% | 0.11 |
| | | | 600 | 0.05 | 1146 | 4% | 0.08 |
| | | | 800 | 0.06 | 1505 | 3% | 0.06 |
| 250 | 31.25 | 8 | 250 | 0.02 | 490 | 6% | 0.15 |
| | | | 450 | 0.04 | 869 | 4% | 0.08 |
| | | | 600 | 0.05 | 1146 | 3% | 0.06 |
| Smooth | | | 150 | 0.01 | 296 | 0% | 0.00 |
| | | | 400 | 0.03 | 776 | 0% | 0.00 |
| | | | 600 | 0.05 | 1146 | 0% | 0.00 |
| | | | 800 | 0.06 | 1505 | 0% | 0.00 |

## Table 13. Measured Test Matrix

| **Asperity Dimensions** | | | **Channel Dimensions** | | | | | |
|---|---|---|---|---|---|---|---|---|
| **Pitch** | **Height** | **Aspect Ratio** | **Separation** | **Aspect Ratio** | **Hydraulic Diameter** | **Relative Roughness** | **Relative Roughness** | **Height-Separation Ratio** |
| $\lambda$ | $h$ | $\lambda/h$ | $b$ | $\alpha$ | $D_h$ | $h/Dh$ | $\varepsilon_{Fp}/D_h$ | $h/b$ |
| **µm** | **µm** | **---** | **µm** | **---** | **µm** | **---** | **---** | **---** |
| 249.5 | 131.0 | 2 | 377.0 | 0.03 | 732 | 18% | 12% | 0.35 |
| | | | 536.2 | 0.04 | 1029 | 13% | 8% | 0.24 |
| | | | 754.6 | 0.06 | 1425 | 9% | 6% | 0.17 |
| | | | 936.9 | 0.07 | 1745 | 8% | 5% | 0.14 |
| 149.8 | 49.6 | 3 | 230.3 | 0.02 | 452 | 11% | 6% | 0.22 |
| | | | 413.7 | 0.03 | 801 | 6% | 3% | 0.12 |
| | | | 551.8 | 0.04 | 1058 | 5% | 3% | 0.09 |
| | | | 751.3 | 0.06 | 1419 | 3% | 2% | 0.07 |
| 250.2 | 49.4 | 5 | 230.5 | 0.02 | 453 | 11% | 6% | 0.21 |
| | | | 414.1 | 0.03 | 802 | 6% | 4% | 0.12 |
| | | | 577.2 | 0.05 | 1104 | 4% | 3% | 0.09 |
| | | | 780.3 | 0.06 | 1470 | 3% | 2% | 0.06 |
| 400.4 | 49.6 | 8 | 257.7 | 0.02 | 505 | 10% | 7% | 0.19 |
| | | | 444.0 | 0.03 | 858 | 6% | 4% | 0.11 |
| | | | 593.4 | 0.05 | 1134 | 4% | 3% | 0.08 |
| | | | 791.0 | 0.06 | 1489 | 3% | 2% | 0.06 |
| 250.6 | 35.6 | 7 | 231.4 | 0.02 | 455 | 8% | 4% | 0.15 |
| | | | 439.0 | 0.03 | 849 | 4% | 2% | 0.08 |
| | | | 571.8 | 0.05 | 1094 | 3% | 2% | 0.06 |
| Smooth | | | 101.8 | 0.01 | 202 | N/A | 0.6% | 0.012 |
| | | | 377.5 | 0.03 | 733 | | 0.2% | 0.003 |
| | | | 548.4 | 0.04 | 1051 | | 0.1% | 0.002 |
| | | | 751.0 | 0.06 | 1418 | | 0.1% | 0.002 |

# Appendix C – Part Drawings

The following drawings were generated in SolidWorks by Brian LaPolt for off-site manufacture via wire EDM. A set of 6 pairs of gauge blocks in total were manufactured; those listed on the part drawing as well as a 9 mm wide gauge block (for setting a 1000 μm channel separation). Roughness samples were made in pairs; three samples of constant roughness height $h$ = 50 μm and varying roughness pitch, and two additional surfaces of shorter and taller roughness heights, $h$ = 31.25 and 125 μm.

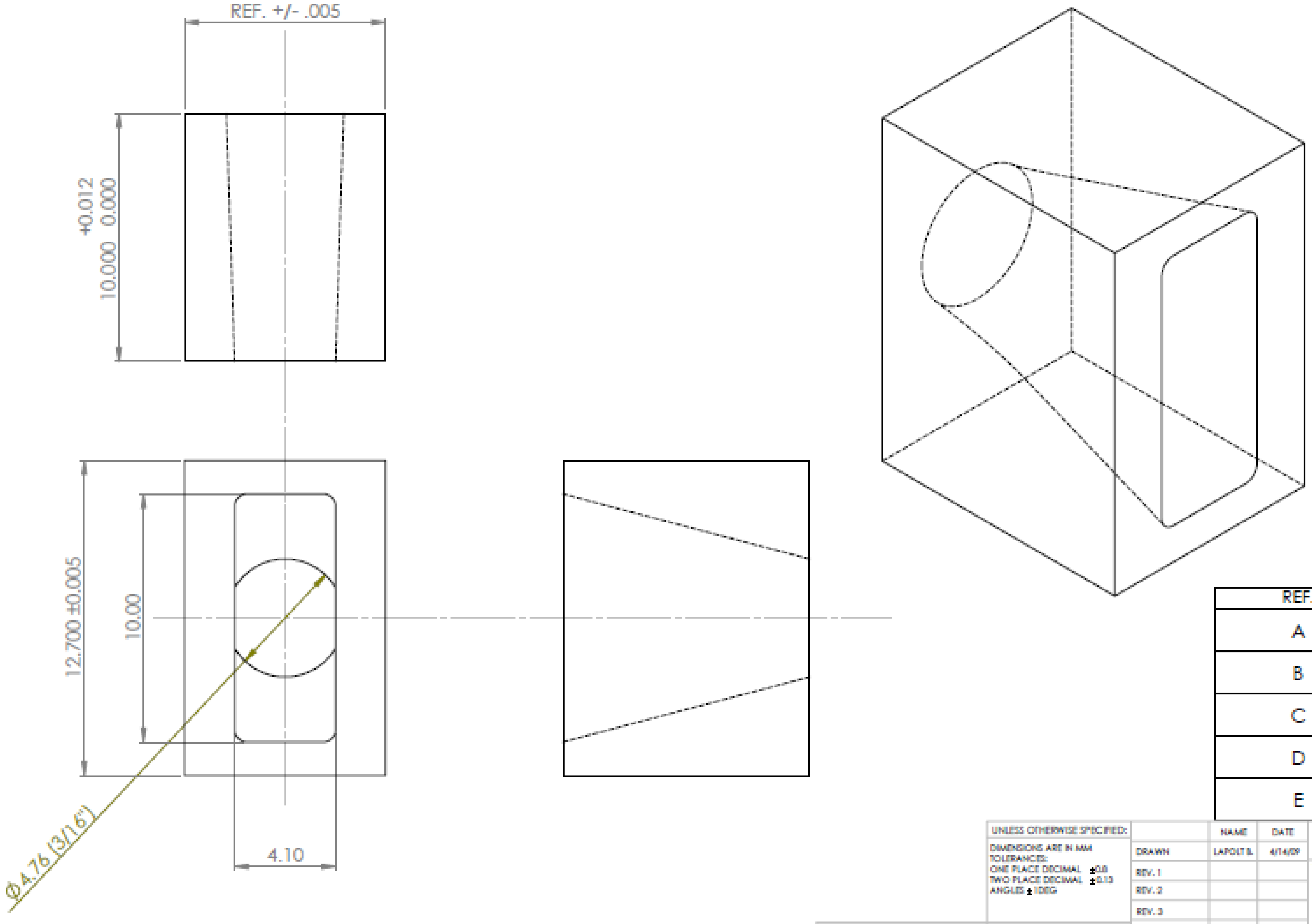

| REF. | Qty. | Dimension |
|---|---|---|
| A | 2 | 8.150 |
| B | 2 | 8.250 |
| C | 2 | 8.450 |
| D | 2 | 8.600 |
| E | 2 | 8.800 |

**PROPRIETARY AND CONFIDENTIAL**

THE INFORMATION CONTAINED IN THIS DRAWING IS THE SOLE PROPERTY OF <INSERT COMPANY NAME HERE>. ANY REPRODUCTION IN PART OR AS A WHOLE WITHOUT THE WRITTEN PERMISSION OF <INSERT COMPANY NAME HERE> IS PROHIBITED.

UNLESS OTHERWISE SPECIFIED:
DIMENSIONS ARE IN MM
TOLERANCES:
ONE PLACE DECIMAL ±0.8
TWO PLACE DECIMAL ±0.13
ANGLES ±1DEG

MATERIAL
17-4 PH

FINISH
8 OR BETTER UNLESS NOTED

DO NOT SCALE DRAWING

| | NAME | DATE |
|---|---|---|
| DRAWN | LAPOLT B. | 4/14/09 |
| REV. 1 | | |
| REV. 2 | | |
| REV. 3 | | |
| REV. 4 | | |

COMMENTS:

Qty. 2 of each Ref. Dimension required. Note the circular and rectangular features are centered in the block.

DO NOT DEBURR KEEP ALL EDGES SHARP.

NSF TEST FIXTURE

TITLE:

Gauge Block

SIZE B
DWG. NO. TestSet-M
REV 1.0
SCALE: 1:2
SHEET 3 OF 10

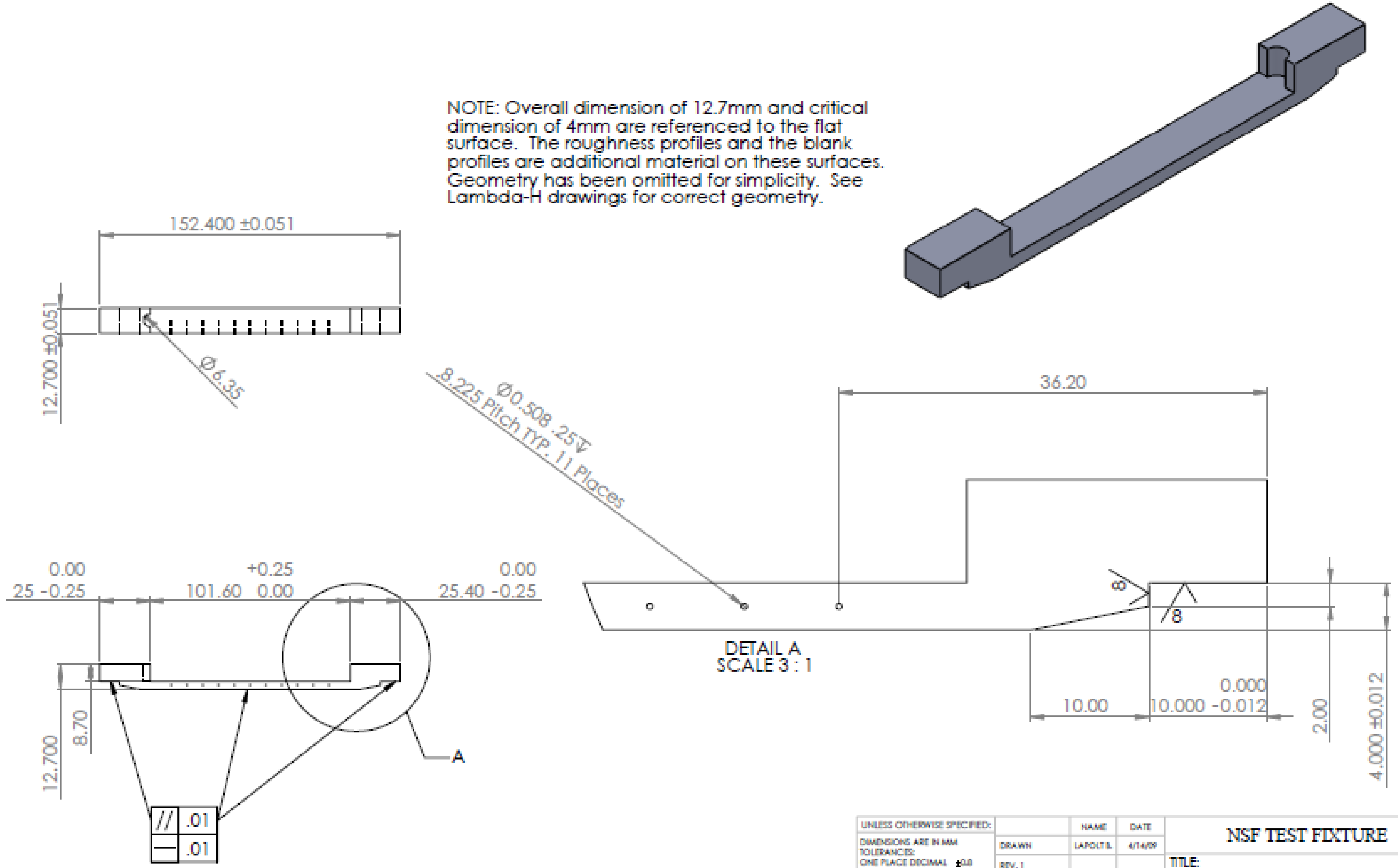

NOTE: Overall dimension of 12.7mm and critical dimension of 4mm are referenced to the flat surface. The roughness profiles and the blank profiles are additional material on these surfaces. Geometry has been omitted for simplicity. See Lambda-H drawings for correct geometry.

DETAIL A
SCALE 3 : 1

**PROPRIETARY AND CONFIDENTIAL**

THE INFORMATION CONTAINED IN THIS DRAWING IS THE SOLE PROPERTY OF <INSERT COMPANY NAME HERE>. ANY REPRODUCTION IN PART OR AS A WHOLE WITHOUT THE WRITTEN PERMISSION OF <INSERT COMPANY NAME HERE> IS PROHIBITED.

UNLESS OTHERWISE SPECIFIED:
DIMENSIONS ARE IN MM
TOLERANCES:
ONE PLACE DECIMAL ±0.0
TWO PLACE DECIMAL ±0.13
ANGLES ±1DEG

MATERIAL
303 Stainless

FINISH
8 OR BETTER UNLESS NOTED

DO NOT SCALE DRAWING

| | NAME | DATE |
|---|---|---|
| DRAWN | LAPOLT B. | 4/14/09 |
| REV. 1 | | |
| REV. 2 | | |
| REV. 3 | | |
| REV. 4 | | |

COMMENTS:
DO NOT DEBURR KEEP ALL EDGES SHARP.

Max permissible radius for inside corners is .13mm

Not required:
- .636mm relief on backside
- .508mm holes x11

NSF TEST FIXTURE

TITLE:
Roughness Sample

SIZE B
DWG. NO. TestSet-M
REV 1.0
SCALE: 1:2
SHEET 4 OF 10